Proceedings of the Special Session on

Structural and Solid Mechanics and

Fatigue Damage of Materials

6th International Conference on

Structural Engineering and Construction Management 2015

Kandy, Sri Lanka

11th to 13th December 2015

Abstracts of 6th International Conference on Structural Engineering and Construction Management 2015

Vision

Promoting innovative research for tomorrow's development

Mission

To meet experts, colleagues and friends in the field and to exchange findings, concepts and ideas on research for the development of a sustainable world

ISBN: 978–955–589–210-0

Printed at: Nethwin Printers (Pvt) Ltd.,
Gampola Road, Peradeniya, Sri Lanka
E-mail: nethwin@yahoo.com

Preface

It is with great pleasure that we present the Proceedings of the 6th International Conference on Structural Engineering and Construction Management (ICSECM 2015). This is the sixth conference consecutively organized following the 1st International Conference on Sustainable Built Environment in 2010, 2nd International Conference on Structural Engineering and Construction Management in 2011, 3rd International Conference on Sustainable Built Environment in 2012, 4th International Conference on Structural Engineering and Construction Management in 2013 and the 5th International Conference on Sustainable Built Environment in 2014, keeping its tradition of adhering to engineering excellence.

Taking a step forward from the last four events, the coverage of specialty areas of this conference has been diversified. This book contains the abstracts of research papers from ten different sub specialties in Construction Management, Construction Materials and Systems, Structural Health Monitoring, Structural and Solid Mechanics, Earthquake Engineering, Fatigue Damage of Materials, Water Safety, Hydraulic Structures, Tall Building and Urban Habitat and MSW and Landfill Management. We expect that all these abstracts will be presented in parallel sessions from 11th to 13th December 2015.

We would like to express our appreciation to all keynote lecturers for their invaluable contribution. We are very much grateful to the authors for contributing research papers of high quality. The research papers of these abstracts in the publication have been peer-reviewed. The enormous work carried out by the reviewers is gratefully appreciated. We are also pleased to acknowledge the advice and assistance provided by the members of the international advisory committee, members of the editorial committee along with many others who volunteered to assist to make this very significant event a success. Finally, we acknowledge the financial sponsorship provided by many organizations that has been extremely helpful in successfully organizing this international conference.

It is the earnest wish of the editors that this book of abstracts and volumes of proceedings would be used by the research community and practicing engineers who are directly or indirectly involved in studies related to Construction Management.

Editorial Committee

6th International Conference on Structural Engineering and Construction Management 2015

11th December 2015.

**Message from
Conference Chairmen**

It is a pleasure for us to welcome all the participants to the 6th International Conference on Structural Engineering and Construction Management 2015 in Kandy, Sri Lanka. We, the co-chairs would gratefully like to mention the previous successful conferences, the 1st International Conference on Sustainable Built Environment 2010, 2nd International Conference on Structural Engineering and Construction Management 2011, 3rd International Conference on Sustainable Built Environment 2012, 4th International Conference on Structural Engineering and Construction Management 2013 and the 5th International Conference on Sustainable Built Environment in 2014, all held in Kandy, Sri Lanka.

The theme selected for the conference - Structural Engineering and Construction Management- is extremely relevant for today's world. With the vision of promoting innovative research for tomorrow's development, we organize this conference as a meeting place of talents, knowledge and dedication. Therefore, we trust that the conference will produce great ideas from a variety of Research and exchange the knowledge of experts, colleagues and friends who are working for the world's sustainable development.

The conference focuses on different sub topics in Structural Engineering and Construction Management, Construction Materials and Systems, Structural Health Monitoring, Structural and Solid Mechanics, Earthquake Engineering, Fatigue Damage of Materials, Water Safety, Hydraulic Structures, Construction Management, Tall Buildings and Urban Habitat and MSW and Landfill Management. The proceedings of the conference are peer reviewed. The full papers are published in volumes in paper format with a book of abstracts.

The host city of the conference, Kandy, is a world heritage city famous for its unique architecture, culture, natural beauty and climate. We hope that you will enjoy your time in Kandy during the conference.

We, the conference co-chairs express our sincere thanks to our guests, keynote speakers, authors, members of the international advisory committee, members of the editorial committee financial sponsors and many others who volunteered to assist to make this very significant event a success.

Prof. Ranjith Dissanayake
Prof. S.M.A. Nanayakkara
Prof. Priyan Mendis
Prof. Janaka Ruwanpura
Dr. G.S.Y De Silva
Eng. Shiromal Fernando

Co-chairs

6th International Conference on Structural Engineering and Construction Management 2015
11th December 2015.

Message from
Dean, Faculty of Engineering, University of Peradeniya.

I am glad to submit this message for the Sixth International Conference on Structural Engineering and Construction Management (ICSECM-2015), which is a continuation of the efforts of the organizers to share knowledge and research in the sectors. This time too, the conference is held in historic city of Kandy, in Sri Lanka.

The ICSECM - 2015 is organized as a joint effort of a number of professionals, and a number of institutions; including Engineering Faculties of Peradeniya, Moratuwa and Ruhuna Universities in Sri Lanka. The topic covered and the keynotes delivered by professionals in the field add more depth to the objectives and outcomes of the conference.

I take this opportunity to thank the organizers for their commitment and persistent effort to make the conference a success. These events facilitate a forum for many young undergraduate and postgraduate students to receive a good initial exposure to present their work, and for some few, to get a flavor of organizing events of global importance.

I believe that the organizers of ICSECM-2015 will continue their dialog of bringing concerned professionals from diverse fields, from different parts of the worlds, into the discussion forum of ICSECM.

I wish the conference a great success.

Prof. Leelananda Rajapaksha

Dean,
Faculty of Engineering,
University of Peradeniya,
Peradeniya,
Sri Lanka.

Table of Contents

SECM/15/014

Design of the new extra-dosed bridge over the Kelani River

Y.K.R. Gunawardena[1*], H. Ohashi[2], Y. Yamahana[3] and T. Nohmi[2]

[1]Consulting Engineers and Architects Associated (Pvt) Ltd, Kotte, Sri Lanka
[2]Oriental Consultants Company Limited, Tokyo, Japan
[3]Katahira and Engineers International, Tokyo, Japan
*E-Mail: yasojag@ gmail.com, TP: +949719724241

Abstract: An extra-dosed post-tensioned pre-stressed concrete box girder bridge over the Kelani River is scheduled to be built as part of an elevated roadway project in Colombo, Sri Lanka. This three-span structure will be 380m long, with a 180m main span. The box-girder will be 5.6m high at the pylon locations and 3.3m at mid-span and the ends. The two U-shaped pylon structures with a twin tower configuration will support a fan-type stay-cable arrangement with 24 stay-cables emanating from each tower. The towers which are 29m high, rise from the piers starting at the level of the under-side of the pot-bearings supporting the box girder. The stay-cables are attached to the 30.4m wide bridge deck at the sides and are proposed to be ECF cables. The detailed design of the bridge was carried out taking into consideration the in-situ balanced cantilever method of construction, which will be used for this bridge, through a staged analysis. The design was carried out in conformance with BS5400. Structural modelling and analysis was carried out using the CSiBridge2015 software. This paper presents and discusses the detailed design procedure of the main bridge elements, the load-cases considered, key results and the planned construction procedure of the proposed bridge

Keywords: balanced-cantilever, extra-dosed, Staged construction analysis

1. Introduction

A new bridge over the Kelani river is scheduled to be built as part of the New Kelani Bridge Construction Project (NKBCP) which is a proposed roadway project which will connect the Colombo Katunayaka Expressway (CKE), which is the expressway connecting the international airport to the city, to one of the main arteries in Colombo, the Baseline road, and to the main access road to the Colombo port through an elevated roadway [1]. This bridge, which will be an Extra-dosed pre-stressed-concrete (PC) box girder bridge and is the centrepiece of the proposed development, will also be a landmark structure for Colombo and the first of its type in Sri Lanka.

2. 'Extra-dosed' Structural concept

In 1988, a French Engineer Jacques Mathivat, proposed a new form of pre-stressed post-tensioned concrete bridge [2] in which he proposed a system of external pre-stressing with the pre-stressing component located outside of the main girder boundaries. The internal pre-stressing of the upper section of the beam was replaced by external cables arranged over a small-sized mast located atop of the pier of the bridge he proposed (Figure 1).

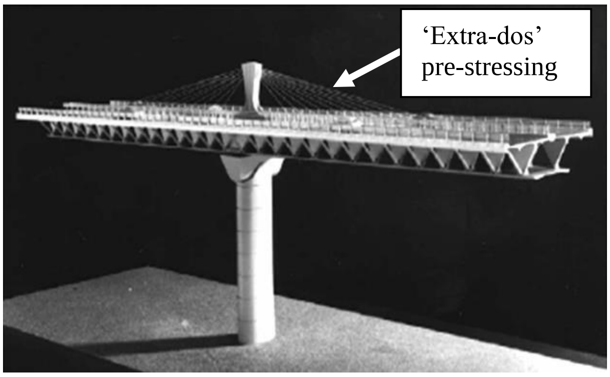

Figure 1: Proposed Viaduct for Arrêt Darré [2]

Since the external pre-stressing arranged by Mathivat was akin to the 'extra-dos', which is the upper curve of an arch, this new form of PC bridge was referred to as the 'Extra-dosed' type. Extra-dosed PC bridges are a hybrid form of bridge incorporating the structural features of PC girder bridges and those of cable-stayed bridges. While in a cable stayed bridge the vertical load is taken exclusively by the stay cables, in an extra-dosed bridge only a proportion of the vertical load is taken by the external cables (cable stays), while the girder itself takes a significant proportion of the vertical load resulting in larger girder depths than for cable stayed bridges of the same span.

The cable stays of an extra-dosed bridge essentially act as external pre-stressing but with a higher effective eccentricity than for conventional external pre-stressing which lie within the confines of the girder structure, resulting in a reduction of girder size compared to girder bridges of the same span. Due to the cable stays acting as external pre-stressing supporting only a proportion of the live load, the cable stays (external pre-stressing) can be stressed to higher stresses than those allowed in cable-stayed bridges [3] as the cables will be less severely loaded for fatigue considerations. In summary, the structural concept of extra-dosed bridges can be described as a PC box girder bridge with external pre-stressing through stay cables which also carry a portion of the vertical load.

3. General design outline

The proposed extra-dosed bridge is a 3-span structure with a 180m main span and two 100m long side spans. The main span length was determined by the design constraint of the need to avoid locating piers within the river limits. The side span lengths were constrained by the need to avoid locating piers on existing roads and the need to keep sufficient head-room over the said roads. An acceptable ratio of main span to side span length was also required in order to minimise out-of-plane forces on the pylon structure. Hence a main span to side span ratio of 1.8 was chosen. The bridge spans from P19 at station 800m to P22 at station 1180m, with pylons P20 and P21 located at stations 900m and 1080m respectively. This notation will be used throughout this paper. The layout of the proposed bridge with respect to the existing roads and bridge is shown in Figure 2.

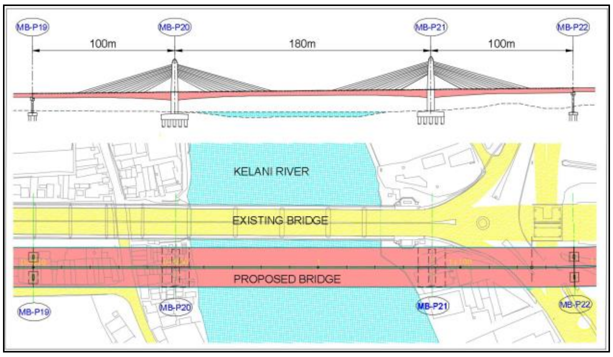

Figure 2: Layout of bridge – plan and elevation

A three cell box girder was chosen as the cross section for the main girder of the bridge. This cross section was chosen based on its high torsional rigidity as well as due to the wide nature of the deck which was designed to support 6 lanes of traffic. The cross sections of the girder at the pylon locations and at mid-span are given in Figure 3.

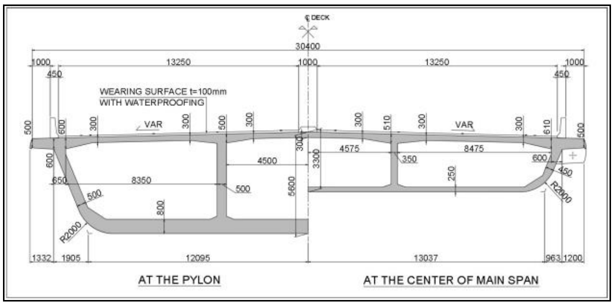

Figure 3: Cross section of main girder

The cross section heights are 5.6m at the pylon locations and 3.3m at mid span and side span ends. As per published literature [3] for extra-dosed bridges, the girder height is usually in the order of L/35~L/45 at the pylon and L/50~L/60 at mid-span, where L is the main span length. For a 180m span this translates into a height of 4~5.1m at the pylon and 3~3.6m at mid-span. A slightly larger value of girder height was chosen for the proposed bridge in order to minimise the size of the stay cables that would be required. In Table 1 typical extra-dosed bridge girder heights are compared to typical values of cable-stayed bridges and PC box girder bridges for the same span.

Table 1: Girder heights for three bridge types

Type of bridge	At pylon	At mid-span
Extra-dosed bridge	L/35 ~ L/45	L/50~L/60
Cable stayed bridge	L/80 ~ L/100 (constant)	
Box girder bridge	L/8 ~ L/16	L/35 ~ L/40

The girder height varies parabolically from 5.6m at the pylon location to 3.3m, 61m either side of the pylon centreline. The girder height is constant from Station 800-839m, for the middle 58m of the main span and also from station 1141-1180m. The top slab is 300mm thick throughout the length of the bridge while the bottom slab thickness and web thickness varies along the length of the bridge as shown in Figure 4.

The girder is supported at the pylon locations and at the end piers on 4 pot bearings each which are located near or directly beneath the web walls. The bearings, which provide no rotational restraint, are fixed in translation in the direction transverse to the bridge axis at all piers, and are free in the longitudinal direction at all piers except at P21.

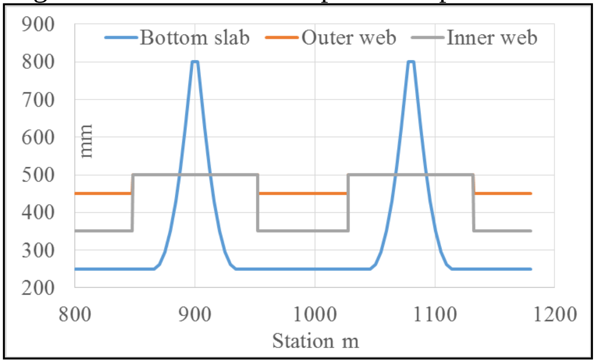

Figure 4: Thickness variation of slabs and webs

Providing longitudinal fixity only at a single pier is not usual in long-span bridge design. This layout was adopted since the design longitudinal load-effects due to wind, temperature and seismic loading in Sri Lanka were relatively minor. The girder is also supported by a system of stay cables emanating from two U-shaped pylons with a twin tower configuration. The twin towers are approximately 20m high above the top surface of the box girder and are inclined 5^0 to the vertical for aesthetic reasons. Each tower supports two planes of stay cables composed of 12 stay cables each. Hence 24 stays emanate out from each pylon. The design resulted in the shortest six cables in each plane being 27 tendon cables while the longest six were 37 tendon cables. The layout of the pylons and stay cables are shown in Figures 5 and 6. The twin towers are rigidly connected to the pylon pier while the connection between the girder and pylon pier is through pot bearings as described.

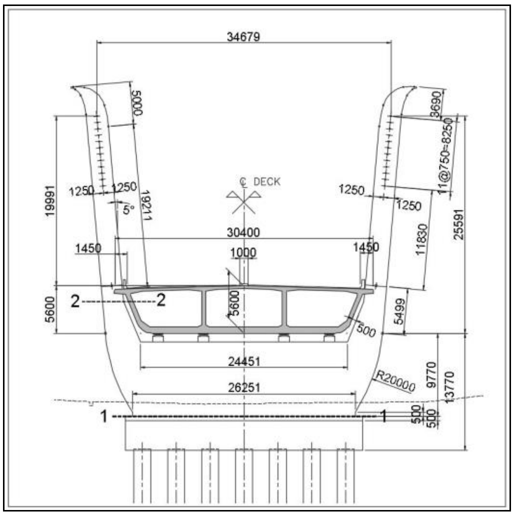

Figure 5: Pylon layout

General design guidance [3] states that for an extra-dosed bridge the tower height above the girder level is of the order of L/8~L/15 which for a 180m span gives a tower height of 12~22.5m. . Hence the tower height of 20m that was chosen falls within the general design guidance. For comparison, a cable–stayed bridge tower would be approximately 36~60m high for the same span. A double plane stay cable arrangement as described was chosen given the need to incorporate a 30.4m wide deck and due to the increase in torsional stiffness a double plane stay arrangement offers. A fan-type arrangement of stay cables was chosen out of the types commonly used (Figure 7).

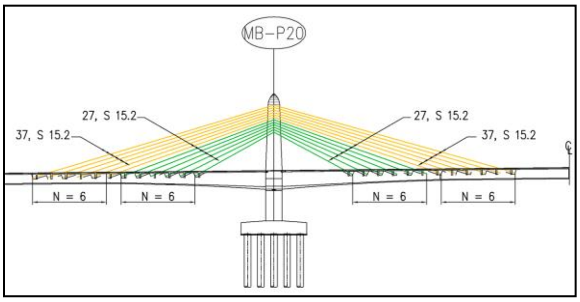

Figure 6: Stay cable layout (P20/P21)

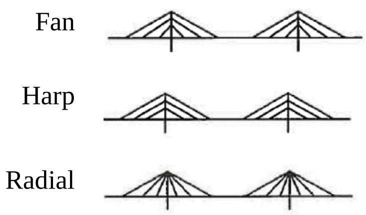

Figure 7: Types of stay cable arrangement

The fan type, which is a hybrid arrangement in between the radial and harp types, utilises cable stays more efficiently than the other types while keeping the sectional forces in the pylon at an acceptable level especially compared to those resulting from the radial type arrangement. The stay cables are located at 4.5m intervals along the suspended length of the girder and spaced at 0.75m intervals at the towers. At the tower a saddle type anchoring system (Figure 8) was chosen since it results in a smaller tower width and smaller spacing of stay cables at the towers than alternative anchorage systems. The 4.5m interval along the girder corresponds to the segment length considered for the girder construction.

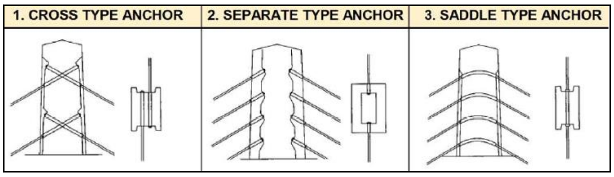

Figure 8: Anchorage systems at pylons

A double tube saddle type tower anchorage system (Figure 9) which allows for the replacement of stay cables was chosen.

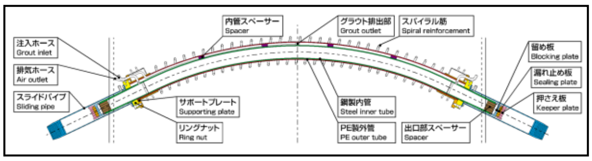

Figure 9: Double-tube saddle anchorage (typical) [4]

Usually, the suspended length of the girder, which is the length supported by stay cables, is of the order of 0.2L. However for this bridge the suspended length was increased to 0.28L, taking into account the deck size as well as to keep the stay cable size to a minimum (Figure 10)

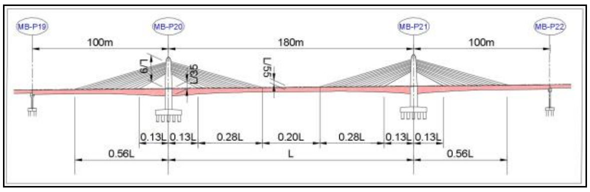

Figure 10: Stay cable layout along the bridge

At the girder level each stay cable is anchored to the girder through anchorages (Figure 11) located on the sides of the bridge deck.

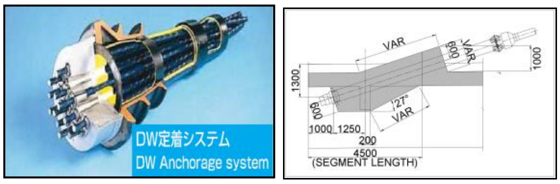

Figure 11: Stay cable anchorage (typical) [4]

The segments of the bridge which contain stay cable anchorages also consist of 400mm thick full width cross beams which are 1750mm high as seen in Figure 12. The structural effect of the cross beams is to improve the load-distribution within the girder cross section of the stay cable forces and to improve the transverse resistance of the girder.

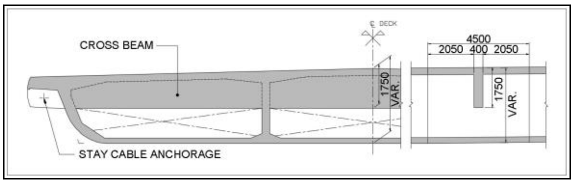

Figure 12: Cross beam layout

Taking into account its excellent corrosion resistance as well as relative ease of construction, epoxy coated and filled (ECF) tendons (Figure 13) will be used for the stay cables of the proposed bridge. In addition to the epoxy coating, the tendon also has a polyethylene (PE) covering and the stay cable itself has a protective PE pipe in which all the tendons are enclosed. ECF tendons also offer superior fretting fatigue resistance compared to other alternatives which is advantageous since the tendons will be susceptible to fretting fatigue due to the saddle type anchorage used at the towers.

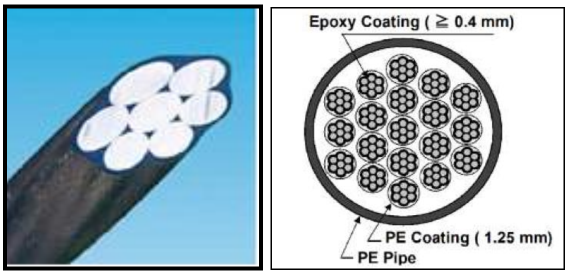

Figure 13: Typical ECF tendon [4] and Stay cable

The sub-surface soil profile at the locations of the proposed piers consist of a thick alluvium layer composed of layers of peat, clay and sand overlaying the bedrock layer. The rock layer consisted of highly to moderately weathered gneiss and was located approximately 25~30m below mean sea level. The allowable bearing capacity for the design of piles socketed in rock was recommended to be 3000kPa together with an ultimate socket friction of ~200kPa. The decision to locate the fixed bearing condition in P20 was made since fixing the girder at P20 resulted in larger lateral forces at P21 (governed by creep and shrinkage effects) and since the ground conditions at P21 were more favourable than at P20.

Table 2: Construction sequence (time in months)

Construction activity	Time
Pile cap, pylon pier and pier head	13
Girder segments without stay cables and part construction of towers	+3.5
Girder segments with stay cables and completion of tower construction	+7.5
Completion of cantilevers	+ 1

Construction of side spans	+ 3
Construction of closure segment at mid span	+1.5
Parapet construction and surfacing	+2

The construction of the proposed extra-dosed bridge will be carried out using the balanced cantilever method with two cantilevers on either side being constructed from each pylon. Table 2 outlines the general planned sequence of construction and approximate timelines. An assumed construction schedule was considered for the structural analysis which is described in the next section.

4. Structural modelling and analysis

The structural modelling for the design of the extra-dosed bridge was done using the CsiBridge2015 analysis software. For the consideration of global effects, a three-dimensional finite element (FE) model consisting of 1-D elements was used. The box girder, pylons, piers and cables were modelled using 1-D frame elements with equivalent stiffness properties. A screen-shot of the finite element model is given in Figure 14.

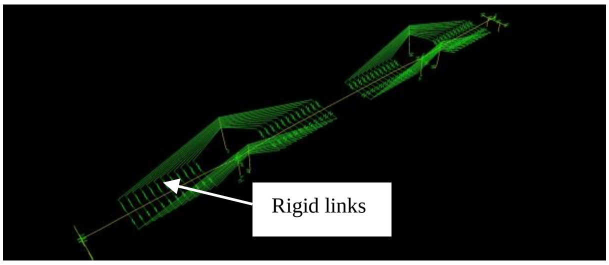

Figure 14: FE analysis model (tendons not shown)

The elements were modelled along the locations of their centroids and the connections between the stay cables and girder were made through rigid links as shown. Since the girder was modelled using frame elements the cross beams were not explicitly modelled. The effects of the cross beams were considered by the use of rigid links as described above. The stay cable anchorage points considered in the model corresponded to their locations in the actual structure. The pylon support foundations were modelled using coupled translational and rotational springs and was updated throughout the analysis to reflect the actual foundation configuration designed. The pot bearings supporting the main girder were modelled using springs with very high translational stiffness with releases specified as appropriate. Hence the connection between the girder elements and the pylon elements in the model was through these spring elements. The 'pier table' of the pylon was modelled by constraining the joints corresponding to the bottom of the pot bearings and the bottom of the towers to act as a rigid body. The stay cables were rigidly connected to the towers at the pylons.

Initially the analysis was done without including the internal pre-stressing tendons within the model. This was done in order to obtain the load-effects of the girder to estimate the required number of internal pre-stressing tendons. The number of internal tendons were then estimated, with an allowance of approximately 2MPa for secondary effects of pre-stressing for the girder. The pre-stressing tendon layout thus designed was then explicitly modelled as elements in the FE model (Figure 15).

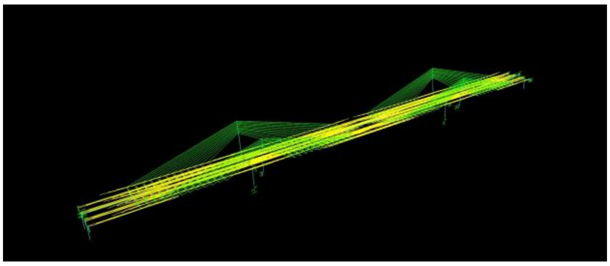

Figure 15: FE model with tendons (in yellow)

The jacking stress for the tendons was specified to be $0.72f_{pu}$. All pre-stress losses were calculated through the software using the following loss parameters. Jacking from both ends was assumed for all internal tendons.

- Friction coefficient 0.3 /rad
- Wobble coefficient 0.004 rad/m
- Wedge draw in 5 mm

The following main loads were considered in the analysis;

1. Dead load and super-dead loads
2. Live loading due to HA and HB loads
3. Wind loading
4. Temperature loading
5. Creep and shrinkage
6. Differential settlement of piers (10mm)
7. Cable and tendon pre-stressing effects
8. Secondary live loading
9. Frictional restraint effects

All loads were considered in accordance with BS5400:2 [5] with traffic loading being taken from BS5400:2(1978). 45 units of HB loading were considered for the analysis. In addition to the aforementioned loads the following special loading conditions were also considered.

1. Sudden loss / replacement of any one stay
2. Replacement of any one bearing

The sudden loss of any one stay was modelled by removing the cable element from the model and re-running the analysis, with equal and opposite forces applied to the girder and tower locations to which the cable was connected to, equal in value to the force in the particular cable at the ULS obtained from the original model (with all load factors set to 1.0). A 1.8 impact factor was applied to take into account dynamic effects. A similar approach was used for the stay and bearing replacement conditions (without the impact factor).

As the bridge will be constructed using the balanced cantilever method a staged analysis was done in order to realistically model dead load effects and effects due to creep and shrinkage. An assumed construction schedule was used for the staged analysis. A 15 day cycle was considered for the construction of girder segments without stay cable anchorages and an 18 day cycle was considered for segments with stay cable anchorages. For each stage, the respective girder segments were added after which the dead load and internal pre-stressing were applied and stay cable pre-stressing applied thereafter where appropriate. During construction of the cantilevers the springs modelling the pot-bearings at the pylons were temporarily assigned to provide full restraint. In reality too, a temporary fixing arrangement will be constructed at the pylon locations to facilitate balanced cantilever construction. When adding the respective segments in the analysis model, segments on either side of the pylon were added at the same time, mimicking the proposed actual construction sequence. Once the cantilever construction was completed, the side-spans were added to the model after which the rotational restraints temporarily assigned to the pylon bearing springs were released. The closure segment at mid-span was then added and the final translational releases were assigned to the bearing-springs, prior to stressing the bottom tendons of the closure segment. The super-dead loads were then added and the effects of long term creep and shrinkage were assessed through time-lapse load-stages which calculated effects up-to 30 years (T=∞) after completion of the bridge (T=0). The creep and shrinkage calculation was done through the software which followed the procedure specified in the CEB-FIP 1990 model code [6]. The creep and shrinkage effects were considered not only for the long term but throughout the construction period. Figure 16 shows a screen-shot of the stage at which the cantilevers emanating out of P20 have been completed.

The effects of all other loads were calculated using the staged analysis model (and associated stiffness) at T=0. The HA and HB live load effects were calculated through influence line analysis using the in-built function of the analysis software. For the wind loading a basic wind speed of 33.5 ms^{-1} was considered [7] while for temperature loading effects, a uniform temperature difference of +/- 7^0C was considered with an installation temperature of 32^0C [8]. A temperature difference +/- 8^0C was considered between steel and concrete elements of the bridge. The re-distribution of load effects due to the change of support fixities was calculated through the software itself. During the staged analysis, the loading from the form traveller was considered as a point load of 160T while a construction live load of 14.6 kN/m on one cantilever and half the load on the other was also considered. The main material parameters considered in the analysis are tabulated in Table 3.

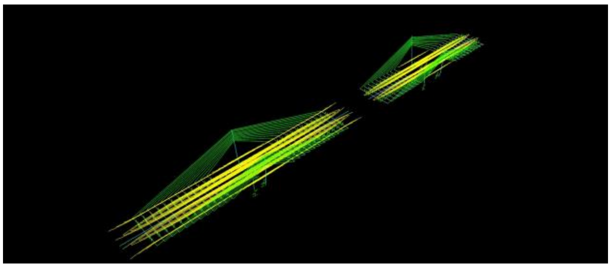

Figure 16: Model at completion of P20 cantilevers

Table 3: Main material parameters considered

Parameter	Value
E (Young's Modulus) of girder (1.15 x 34 – taking into account effect of rebar and tendons) - G50 concrete	39.1 GPa
E of tower - G50 concrete	34 GPa
E of pier (pylon piers included) – G40	31 GPa
E of pre-stressing tendons/cable stays	200 GPa
Shrinkage start date as per [6]	3 days
UTS of tendons f_{pu}	1850 MPa
Relative humidity	70%
Shrinkage coefficient as per [6] β_{sc}	5
Relaxation class as per [6]	2

The full sectional stiffness was considered for the girder elements in the analysis while the sectional stiffness of the pylons and piers were reduced by 50% to account for the fact that these will be cracked at SLS. The same analysis model was used for SLS and ULS, in line with limit state theory. For the stay cables no 'apparent modulus' effects

[9] were considered, since even for the longest cable, the change in modulus was negligible.

Initially the analysis was run with all stay cables considered as 27 tendon cables. However it was ascertained that the cable capacity was not sufficient to meet the design criteria upon which the longest six stay cables emanating from each tower was changed to 37 tendon cables. The stay cable pre-stress was applied through the software at each relevant analysis stage as a 'target-force' load-case in which the software increased the strain of the cable until it achieved the specified force. The amount of stay cable pre-stress was initially determined considering the remaining allowable force increase in the cables after the resulting SLS loads in the cables without pre-stress were deducted. Since staged analysis is a type of non-linear analysis, the maximum amount of pre-stress was finalised through iteration.

Creep and shrinkage loss of internal pre-stress was accounted for in the analysis itself as the tendons were modelled explicitly and deformed compatibly with the elements they were embedded to.

5. Detailed design of box girder

Using the load-effects from the global analysis, the SLS and ULS design of the main box girder for longitudinal effects was carried out. The steps described in sections 5.1 to 5.3 were followed in the design. In the longitudinal direction, the main box girder was designed as a Class 2 pre-stressed concrete member as per BS5400-4 [5]. The internal pre-stressing layouts that were designed for the top and bottom slabs of the main box girder are shown in Figures 17a-c. The arrangement is symmetric about the centreline of the girder cross section.

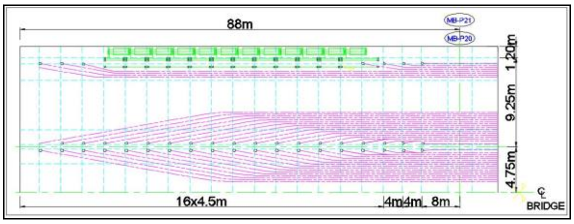

Figure 17a: Top slab pre-stressing (for P20/P21 cantilever spans) – 88 x 15ø15.2mm tendons

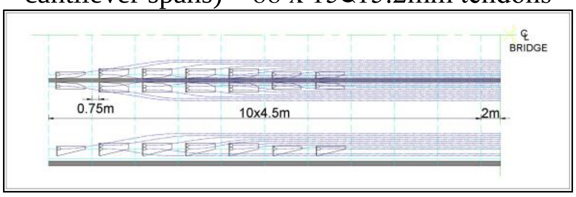

Figure 17b: Bottom slab pre-stressing (mid-span) 66 x 15ø15.2mm tendons

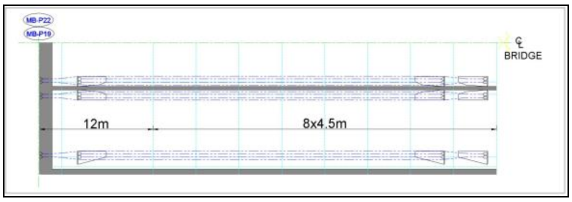

Figure 17c: Bottom slab pre-stressing (side-spans) – 24 x 15ø15.2mm tendons

5.1 Stress check for completed bridge

The extreme fibre stresses of the main girder cross section due to the critical load combinations were calculated for the bridge at and after completion. The resulting stresses were then checked with the relevant stress limitations, which as per BS5400-4 Section 6.3.2 [5] were 2.55 MPa in tension and 20 MPa in compression for grade 50 concrete. The calculated extreme fibre stresses along the bridge are shown in Figure 18. When calculating the stresses, for contributions from the axial forces applied on the girder by the stay cables and internal tendons, a distribution angle of 33^0 was considered [10], since the axial forces are not immediately effective across the whole cross section (Figure 19). This resulted in an effective distribution length behind the anchorage of approximately 7.5m. In the calculation of stresses the contribution from the aforesaid axial forces was only considered effective after this length.

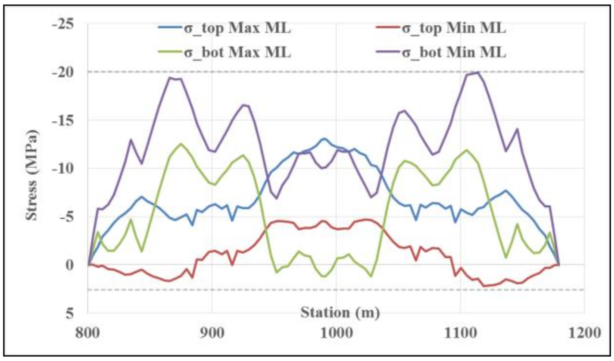

Figure 18: Extreme SLS fibre stresses (T = 0 to ∞) (Tension positive, sagging moment positive)

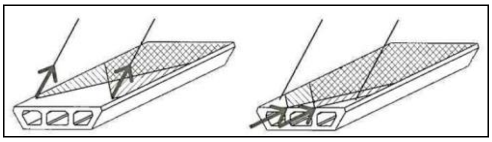

Figure 19: Distribution of applied axial forces

5.2 Stress check during construction

Similar to 5.1, stresses were also calculated for load-effects during construction. It was confirmed that the maximum and minimum stresses during construction were also within the required limits.

5.3 Ultimate capacity checks

In addition to the SLS design, the ULS moment, shear and torsion capacities were also checked. For the longitudinal moment capacity in order to obtain the required capacity above the applied ULS moment it was necessary to design and consider the capacity contributions from the reinforcement of the top and bottom slabs. The longitudinal reinforcement thus designed is tabulated in Table 4. The moment capacity was calculated taking into account the co-existing axial force in the section. Figure 20 shows the variation of maximum and minimum ULS longitudinal moments and the calculated ULS capacities.

Table 4: Slab rebar (top and bottom surfaces)

Slab	Rebar (c/c in mm)	Length along bridge
Top slab	H12@150 c/c	Full length
Bottom slab	H12@150 c/c	P20/21 to P20/21 +/- 12m, P20/21 +/- 54m to +/-90m and side span ends
	H25@150 c/c	P20/21 +/- 12m to +/- 36m
	H20@150 c/c	P20/21 +/- 36m to +/- 54m

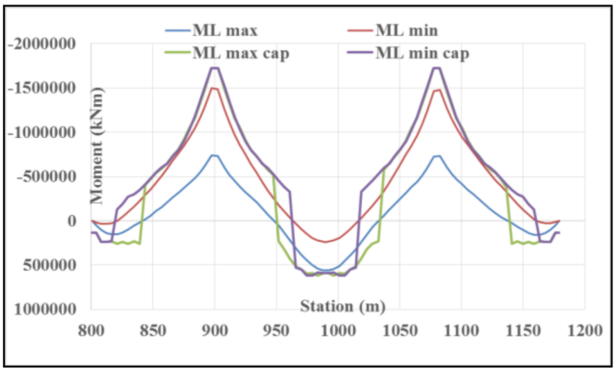

Figure 20: ULS moments and capacities (Sagging moments positive)

The ULS shear and torsion effects were also assessed. The distribution of shear between the outer and inner webs was obtained through an additional finite element model which modelled each web and associated top and bottom slabs as separate elements along with the cross beams. For the outer and inner webs maximum distribution ratios of 0.37 and 0.20 were obtained. These ratios together with the obtained load-effects from the main analysis model was used for ULS shear design of the girder.

5.4 Displacement of girder

The displaced shape of the bridge due to dead and super dead loads (including pre-stress) at the end of creep and shrinkage is shown in Figure 21. A maximum displacement of 423mm (~ L/425) was calculated from the analysis at mid-span. During construction this long term deflection needs to be taken into account in order to ensure that the road alignment of the structure achieves the design requirement in the long term.

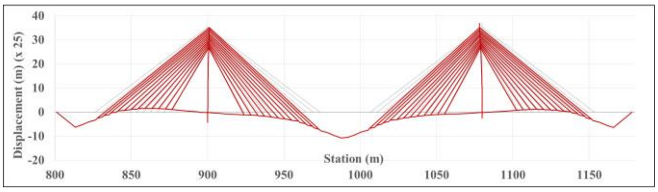

Figure 21: Long term bridge displacement

6. Detailed design of stay cables

The stay cables were designed ensuring that SLS loads in the cables did not exceed $0.6f_{pu}$. For the load-cases of sudden loss of one stay and stay replacement, a stress of $0.65f_{pu}$ was permitted while during construction a maximum stress of $0.7f_{pu}$ was considered permissible. The resulting maximum SLS cable loads for cables emanating from P20 and P21 are shown in Figure 22. Results are presented for cables of one tower of each pylon (as effects are nearly symmetric). As can be seen the maximum cable loads are less than the allowable for all cables. Since the loads in the cables vary due to the live load, fatigue of the cables was also considered. The allowable stress for fatigue is a function of the maximum allowable SLS stress [3] as shown in Figure 23.

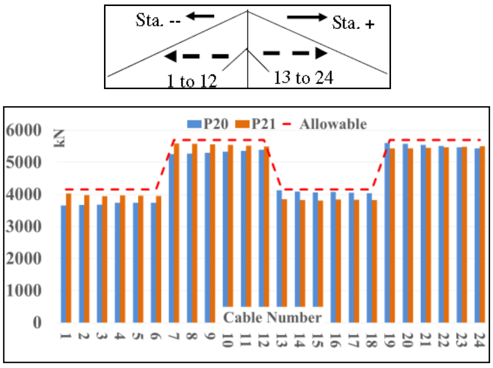

Figure 22: Maximum SLS cable loads (P20/P21)

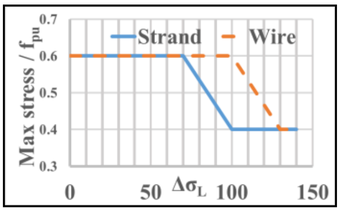

Figure 23: Allowable fatigue stress range ($\Delta\sigma_L$) [3]

For an allowable stress of $0.6f_{pu}$, the allowable stress range is 70 MPa. The calculated cable stress ranges due to live load (HA loading only) are shown in Figure 24. Using HA loading to assess fatigue stress ranges may seem overly conservative. However this method is acceptable since additional bending stresses induced in the cables near anchorages [11] are not explicitly taken into account in the analysis.

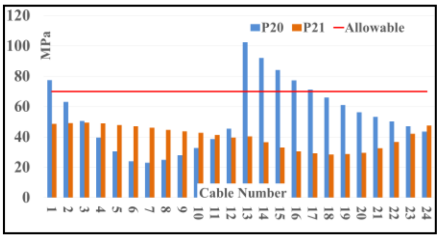

Figure 24: Stay Cable stresses due to HA loading

The shortest five cables of P20 were observed to have stress ranges above the limiting value. This was mitigated by increasing the number of tendons used for these stays. Cable vibrations due to wind/rain will be monitored during construction and damping devices will be designed and installed as required.

7. Detailed design of pylons

The towers of the pylon vary from a 2.5m x 3.5m section at the top to a 2.5m x 5m section at the level of the top of the girder, after which the section increases in width until the level of the 'pier-table', as shown in Figure 25. Below the level of the pier table the pylon 'pier' is a cellular box structure with the typical section as shown in Figure 26. The overall width of the pier varies from 32.71m at level of the bearings to 26.25m at level of the top of the pile cap.

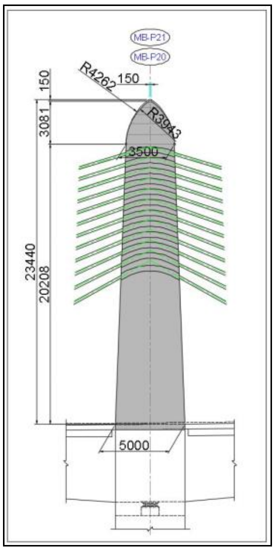

Figure 25: Pylon tower section variation

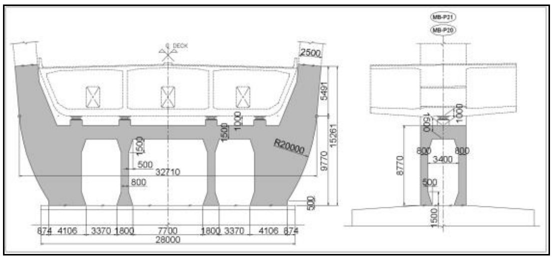

Figure 26: Pylon pier typical cross sections

The tower and pier sections were designed as bi-axially loaded reinforced concrete columns at the ULS and the crack widths were checked at the SLS. The ULS maximum axial force and sectional moments for Sections 1-1 and 2-2 as defined in Figure 5, are given in Table 5 for pylon P20, along with the designed perimeter axial reinforcement. The design of the end piers is not explicitly described in this paper as its design depends on the loadings from the approach bridge as well. However the design philosophy of the piers is the same as that of the pylons.

Table 5: ULS load-effects for pylon P20

Load-effect	Sect 1-1	Sect 2-2
Max compression kN	257606	34818
Min compression kN	185037	53357
Max moment about longitudinal axis	106814	37936
Max moment about transverse axis	501642	120504
Max shear in longitudinal dir.	14955	7365
Max shear in transverse dir.	2944	1998
Max torsion	39439	4
Designed axial rebar	H32@150 mm c/c	H32+H40 @150mm

8. Detailed design of foundations

The designed pile layout for pylons P20 and P21 is shown in Figure 27 while the corresponding pile cap section is shown in Figure 28. 2m diameter piles were considered in the design.

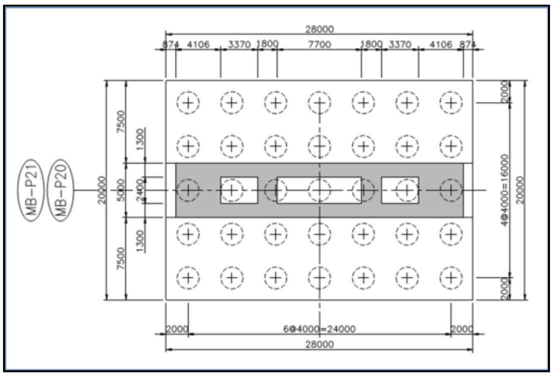

Figure 27: Pile layout of P20/P21 foundations

The design of piles was carried out by using the reactions of the pylon support springs which modelled the effect of the pile foundations in the global analysis model, and applying the said reactions as input loads to a separate finite element model of the pile system. This finite element model is shown in Figure 29.

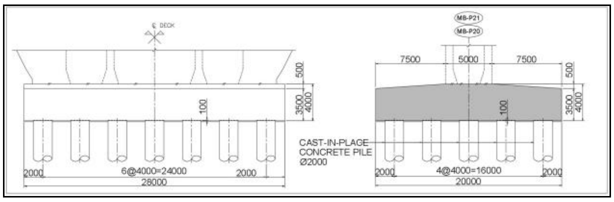

Figure 28: Pile cap dimensions P20/P21

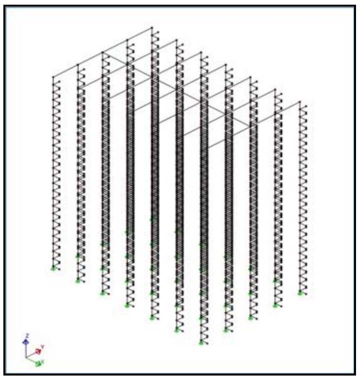

Figure 29 – FE model used for pile design

The top of the piles in the above model was joined together by rigid elements as the 4m high pile cap was considered to be rigid. The piles were supported by springs spaced at 1m intervals which modelled the varying stiffness of the soil layers. The bearing stress from the pile acting on the bearing layer was calculated using the SLS axial force at the bottom of the pile. The pile reinforcement was designed for the ULS condition by considered the pile as a bi-axially loaded reinforced concrete column. The maximum load-effects used for the design of piles in P20 and P21 are tabulated in Table 6. The pile caps of both P20 and P21 pylons are 28m long, 20m wide and 4m high. The pile cap reinforcement was designed based on the moments in the 28m x 4m sections at the face of the pylon pier. This resulted in bottom main reinforcement of 2 x 2H32@150mm c/c. Due to the arrangement of the pylons, the 20m x 4m sections were not critical for the pile cap design.

9. Conclusion and further work

This paper has presented and discussed the detailed design of the main structural elements of the proposed new extra-dosed bridge over the Kelani River, which will be the first of its kind in the country. At the time of writing this paper the detailed design work is ongoing, especially with regard to bearing design, anchorage design and transverse design of the box girder and cross-beams. It is hoped that more details of the design will be the subject of a separate paper in the future.

Table 6: Pile load-effects (kN/kNm)

Load effect	P20	P21
Max SLS axial compression	11618	12122
Max ULS axial compression	15040	15604
Min ULS axial compression	4740	3978
Max ULS moment (moment	1357 (43)	1266 (20)
about ppclr. dir in brackets)	1027 (541)	1122 (603)
Axial rebar	40H25 @ upper part	
	40H20 @ lower part	

Acknowledgement

The assistance provided by Suneth Priyankara in the preparation of figures and the overall support and encouragement given to the authors by the Project Director and other officials of the Road Development Authority in charge of the NKBCP for the writing of this paper is acknowledged.

References

[1]. Ohashi H. et al., "Outline of the new bridge construction project over the Kelani river", ICSECM, Kandy, 2015. (not yet published)

[2]. Benjumea J. et al., "Structural behaviour and design criteria of extradosed bridges", J. of Construction Engineering, Vol. 25, No. 03,

pp. 383-398, Pontifical Catholic University of Chile, 2010.
[3]. Specifications for Design and Construction of Cable-Stayed Bridge and Extradosed Bridge, Japan Prestressed Concrete Institute, 2012.
[4]. Company product brochures, Sumitomo Electric Industries Ltd., Japan.
[5]. BS5400, Steel, concrete and composite bridges Parts 1 to 10, BSI, London, 1978 & 2006.
[6]. CEB-FIP model code 1990, Euro International Committee for Concrete, Thomas Telford, 1993.
[7]. Design of buildings for high winds, Ministry of Housing and Construction, Sri Lanka, 1980.
[8]. Bridge Design Manual, Road Development Authority, Sri Lanka, 1997.
[9]. Mathivat J, The cantilever construction of prestressed concrete bridges, Wiley, 1983.
[10]. Specification for highway bridges Part 1-Common, Japan Road Association, 2002.
[11]. Gimsing N.J., Cable supported bridges, Wiley, 1983.

SECM/15/015

Outline of the New Construction Project over the Kelani River

H. Ohashi[1*], D. Jayasekare[2] and T. Oguni[3]

[1] Team Leader, Oriental Consultant and Katahira Engineering International JV Project Director,
[2] Road Development Authority, Ministry of University Education & Highways
[3]Oriental Consultant and Katahira Engineering International JV
*E-Mail: ohashi-hr@oriconsul.com

Abstract: This project is to construct part of urban expressway in the most congested area in Colombo, Sri Lanka. It is featured by a long-span prestressed concrete extradosed bridge and elevated steel box girders supported by steel portal frame piers. This paper presents outline of the project by focusing on the advancement of technologies employed in this design, construction method and long-term durability.

Keywords: High performance steel, epoxy coated and filled strand, extradosed bridge, accelerated construction, gravel compaction, urban elevated steel bridge

.

1. Introduction

With the opening of Colombo-Katunayake Expressway (CKE) connecting the Sri Lankan capital to Bandaranaike International Airport in October 2013, there is a considerable increase in the traffic entering the Colombo city and the capacity of existing New Kelani Bridge will not be sufficient to cater to such heavy traffic volume. The daily traffic volume of both roads is 86,000 vehicles on Baseline Road and 27,000 vehicles on Port Access Road.

Major developments in Colombo city and Colombo Port will further increase the traffic in this area. Therefore, Road Development Authority has decided to implement a project to construct a new bridge adjoining the existing bridge with six lanes together with related elevated approach bridges and interchanges.

This Project is the largest bridge construction project in Sri Lanka. As a symbol of Greater Colombo region, it has a long-span extradosed bridge and advanced technical features. The construction will commence in early 2017 and is scheduled to complete by end of 2019. This paper describes the outline of the detailed design and involved technical features.

2. Scope of the Project

The Project is located about 5km north of Colombo Center (Figure 1). The route starting at CKE end point, diverges from the CKE and runs parallel to the existing road, then at the Kelanitissa Junction, 4-lane elevated bridge runs south over Baseline Road 4-lane diverge to west on Port Access Road through the Junction. Those elevated steel box girder bridges will be built over the existing roads supported by steel portal frame piers.

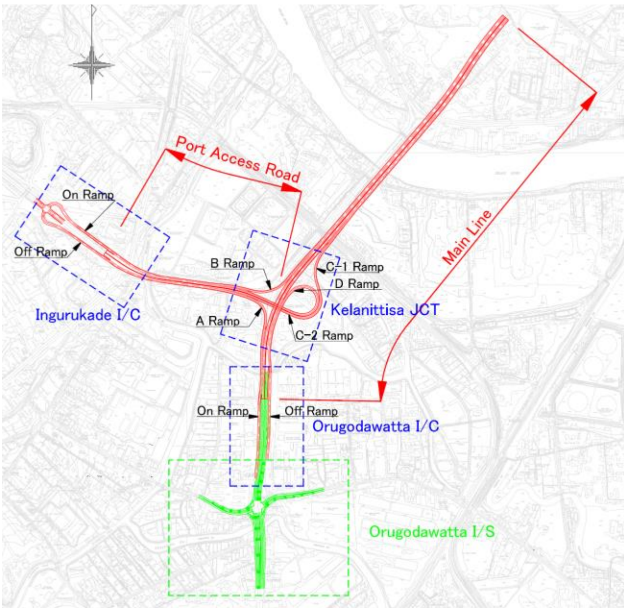

Figure 1: Project Outline

The design life is 120 years. The applied bridge design codes are Bridge Design Manual, Road Development Authority, Sri Lanka, and BS5400, and Bridge Design Standard for Highway Bridges in Japan.

Live load is in accordance with BS5400-2 (1978), including HA loading and 45 units of HB loading. Basic wind speed is 33.5m/sec.

3. Extradosed and PC Box Girder Bridge

3.1 Extradosed Bridge

The extradosed bridge crossing the Kelani River accommodates 6-lane traffic with 380m length having 180-m main span and two 100m side spans. The pylons are reinforced concrete and main girders are three cell prestressed concrete box girder. The girders are supported by pod bearings, longitudinally fixed at one pylon and the others free. The pylon foundations are with 2 m diameter bored piles. The piles are basically end bearing type and the ends socketed into rock.

The stay cables, 12 stays per plane with 37 strands maximum are continuous at pylon and supported by saddles embedded into pylon and the stay cable sockets are fixed to the main girder. The stay cables are composed of epoxy coated and filled 7-wire strands which exterior is coated with polyethylene, and then entire strands are covered by polyethylene pipe, thus giving three layers of corrosion protection system.

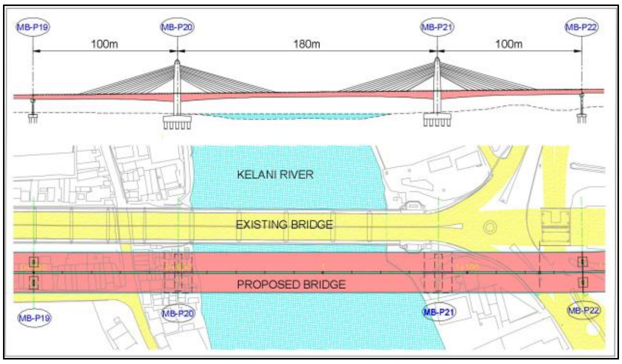

Figure 2: Extradosed Bridge

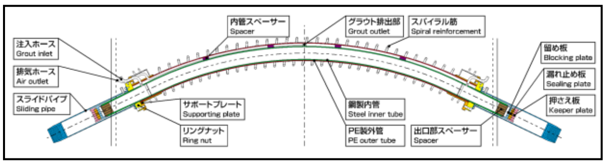

Figure 3: Stay Cable and Saddle

The main girders' three cells have a depth of 5.6m at the pylon and 3.3m at the mid span. The girders are supported by stay cables at 4.5m spacing, considering the construction duration. The girders are longitudinally prestressed and the deck has transverse prestressing for durability.

The pylon extends 23.4m above the deck level, which is L/9 where L is main span length. The pylon is slanted outward and the tip is curved for aesthetical consideration.

The cube strength of concrete for pylons and main girders is 50MPa.

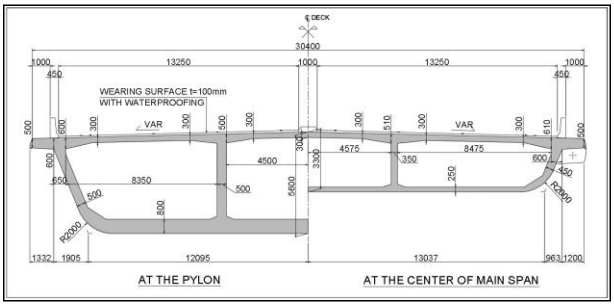

Figure 4: Cross Section at Pylon

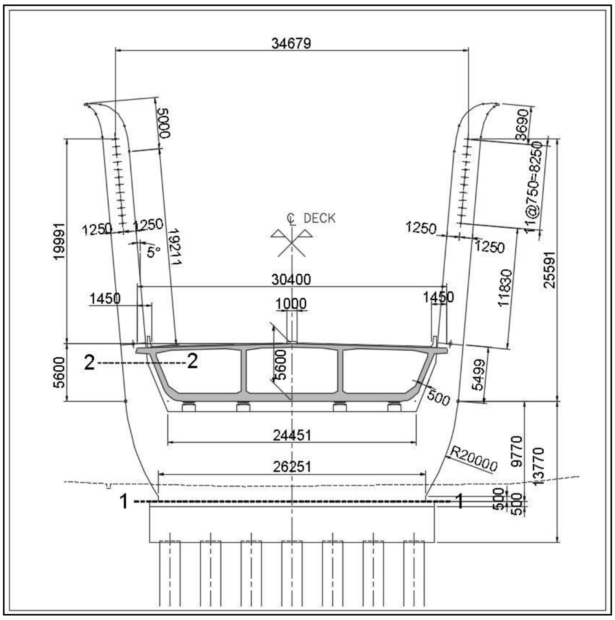

Figure 5: Cross Section at Pylon

3.2 PC Box Girder Bridge

Two PC box girder bridges are located in the northern end in this project. The one connecting with CKE is a 6-span continuous bridge with 40m to 45m spans. It has a double cell girder of 20.5m width. The other end which connects with the extradosed bridge and steel girder and ramp is a 4 and 5-span continuous box girders having variable width with spans varying from 40m to 45m. Those bridge girders are monolithic with the piers. The section is single section for narrow box and double cell section for wide section.

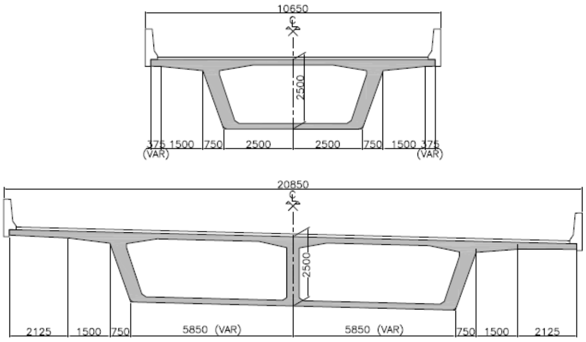

Figure 6: PC Box Girder Sections
(Double-cell section)

4. Steel Bridges

The application of steel box girders and steel piers is to facilitate accelerated construction over the most congested roads in Colombo. Also the junction and interchange bridges are made of steel box girders. Merging and diverging ramps to the main line makes the overall widths of the girders varying.

Although the expansion and contraction due to temperature changes (24 to 40 deg C.) and live loads is small, steel finger-type expansion joints are adopted for long-term durability.

4.1 Steel Box Girders

The span lengths are varying from 42.5m to 78m maximum. This variance is due to the designing of the structure to avoid interference with underground utilities and surrounding important buildings and structures. Those long-spans are not usual for elevated bridges built on land which require 3m deep box girders.

The mainline bridges are consisted of 4 to 5 number of 2m wide box girders. Each box girder is supported by one set of pot bearing at each pier location. However, for ramp bridges, curved with maximum of 50m radius, two bearings support the girder at each pier. The girder for ramp is a single trapezoidal box girder with 6m wide top flange.

The box girder depth is 2m for the main line but the long spans including ramp has 3m depth. The steel grade for the long spans is Bridge High Performance Steel, SHBS500 which has yield strength of 500MPa. This TMCP (Thermo-Mechanically Control Process) steel has been developed as 15% higher than ordinary high strength steel of this grade and has higher ductility and low pre-heat requirements, thus ease of fabrication.

For corrosion protection, the exterior surface of steel will be coated with fluorescent resin paint, with a total film thickness of 250 micro meters, which has said to be 40-60 years effective life.

The deck is a steel-concrete composite deck, which is made of prefabricated steel panels which serves as a form for casting concrete as shown in Figure 9 for example. The bottom plate is 8mm thick and concrete slab is composite with this bottom steel. The deck depth varies 260mm to 300mm.

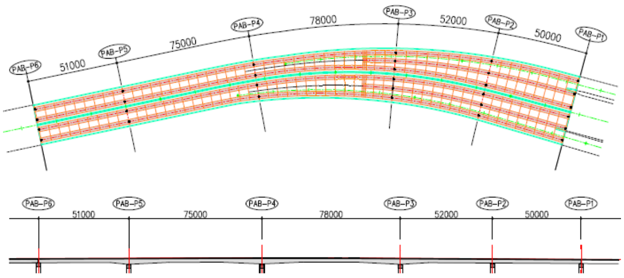

Figure 7: Port Access Bridge

Figure 8: Junction Bridge

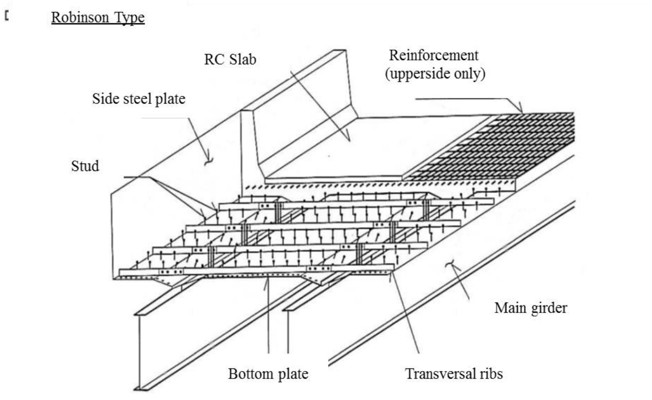

Figure 9: Steel-concrete Composite Deck (typical)

4.2 Steel Portal Frame Piers

The location of pier footing was determined to avoid interference with underground utilities.

Therefore, their portal frame transverse beam had to be widened up to 47m maximum at some locations. The depth of the beam is 2m and 2.5m.

The corner plate thickness of the rigid frame is thickened up to 60mm due to shear lag effect. This also necessitated the use of high strength steel, 500MPa Bridge High Performance Steel, same as for the long-span girders. This high performance steel reduces steel weight at the rigid frame corners.

The column ends connected by 100mm to 140mm diameter anchor bolts which are embedded into footing. Inside of column bottom is filled with concrete.

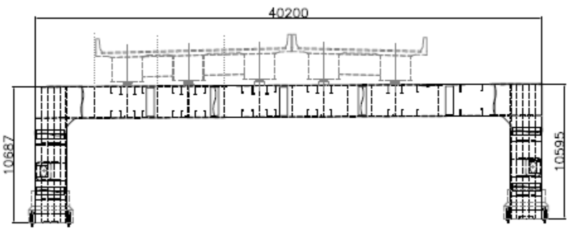

Figure 10: Portal Frame Pier

4.3 Foundations

Bored piles are adopted for the foundation for piers and abutments. Those along the Port Access Road are single laid piles by which the transverse width was reduced because of underground high voltage power cables. Also some foundations needed to adopt eccentric foundations to reduce the transverse dimension of the footing. The diameters of piles are 2.0m, 1.5m and 1.2m.

Pile tip is penetrated into rock designated as Grades IV and III, highly to moderately weathered gneisses rock. Figure 11 shows boring logs for extradosed bridge piers. Allowable end bearing pressure is 3000 to 5000 kPa. Also skin friction is considered for medium to dense soil layers.

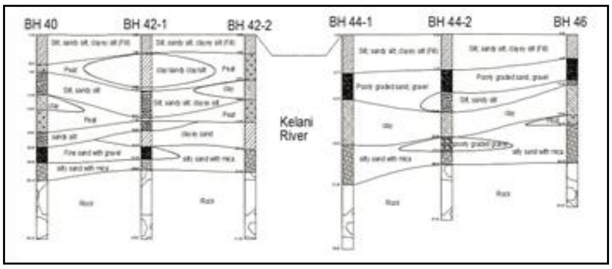

Figure 11: Soil Profile

The abutment located at the CKE end lies in soft soil treated area, and it is considered in design that soft ground is treated before the construction of abutment.

4.4 Transportation and Erection

It is a challenge to build such huge steel structure over the heavy traffic roads. Steel segments transported offshore will be landed at the Colombo Port and transported by low-bed trailers to the site.

The 11m-long box girder segments will be pre-assembled for a span or two on temporary bents, and then transversely moves on rollers on the transfer beams on the portal frame beams. The first box girder span is moved laterally for 3m. Then the second box girder span is assembled and connected with the first one by lateral beams. Then those two box girders are moved laterally, and this operation continues until the fourth box girder spans. For the curved sections, the lateral transfer will have to be done several times, and set on the next transfer beam, when the spanning piers are not parallel. Joining is made by 22mm diameter high-tension bolts (S10T).

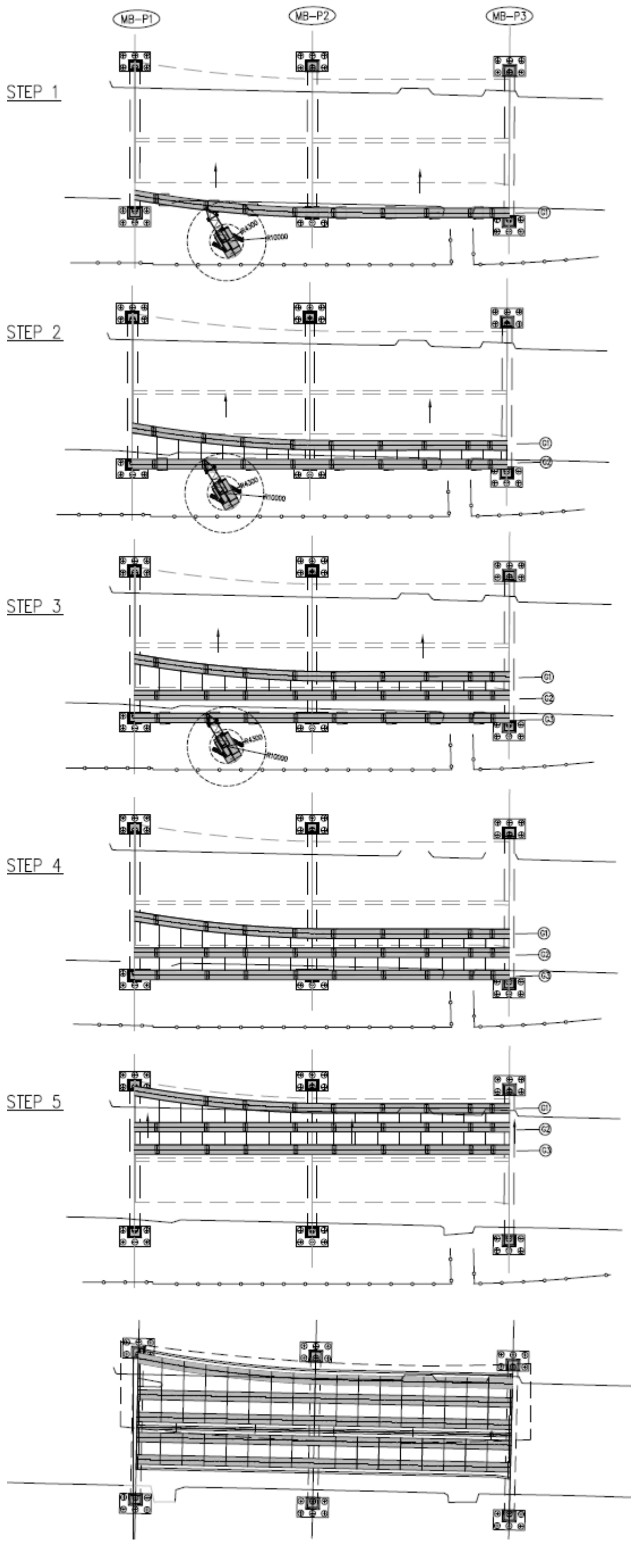

Figure 12: Lateral Transfer of Box Girders

A large lifting crane with a capacity of 160 ton-m will be used to lift up the large segments for assemblage. For the erection of transverse beams of portal frame piers and lateral transfer of box girders, it is necessary to use night time when the traffic is reduced.

Pier columns will be erected by crane installed inside the Right of Way, however, approximately half length of the transverse beam (pre-assembled) will be erected on the temporary bent on the median from the carriageway.

Figure 12 shows construction sequences of box girder erection using lateral transfer.

After erection of girders, panels of steel-concrete composite deck is laid out between the box girders, and connection with main girders is made, followed by casting expansive concrete to complete the deck. Then asphalt pavement with a total thickness of 100mm is laid.

The construction period is scheduled as 3 years, in which approximately 1 year for foundation and 2 years for piers and superstructure.

5. Soft Soil Treatment

The new road merges and connects with CKE end point with an embankment. About 100m section in this region is with around 7.5m deep organic clay underlying requiring soft soil treatment. The new road merges to the existing CKE with embankment with the maximum of 4.5m depth. The CKE embankment was previously improved by use of 0.5m diameter sand compaction pile on 1.5m triangular grid. General plan and subsurface condition is shown in Figure 13.

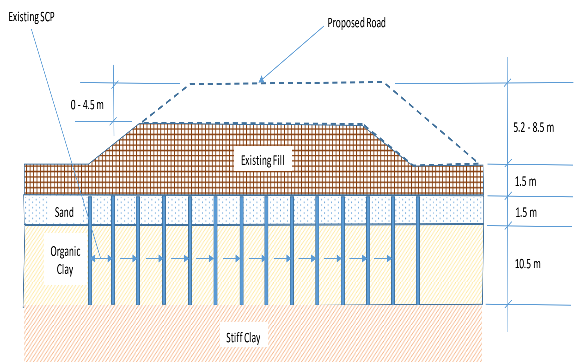

Figure 13: Soft Soil Treatment

The design criteria used for the soft soil improvement is such that the duration for preloading is not more than 18 months, safety factor for short and long term stability is 1.2 and 1.25 respectively, safety factor for bearing is 2.0, residual settlement is less than 150mm after 3 years in service.

The analysis consists of slope stability of embankment, strength evaluation of existing sand piles, and long-term settlement. For settlement analysis, 2D Plaxis software was used. The soil data used for the analysis are tabulated in Table 1.

Table 1: Soil Parameters

Depth (m)	7.5
Soil Layer	clay
Unit Weight (kN/m^3)	14.0
Compression Index, C_c	0.729
Recompression Index, C_r	0.073
Secondary Compression, C_a	0.044
Void Ration, e_0	3.772
Coeff. of Vertical Consolidation, C_v (m^2/yr)	1
Coeff. of Horizontal Consolidation, C_h (m^2/yr)	2

Due to the soft nature of existing soil, ground improvement is necessary to reduce post construction settlement and to improve ground stability. The ground improvement work will consist of embankment preloading and installation of granular compaction piles (GCP). GCP are constructed by compacted sand or gravel, which is inserted into the soft clay by displacement method and thus create a composite ground (Figure 14).

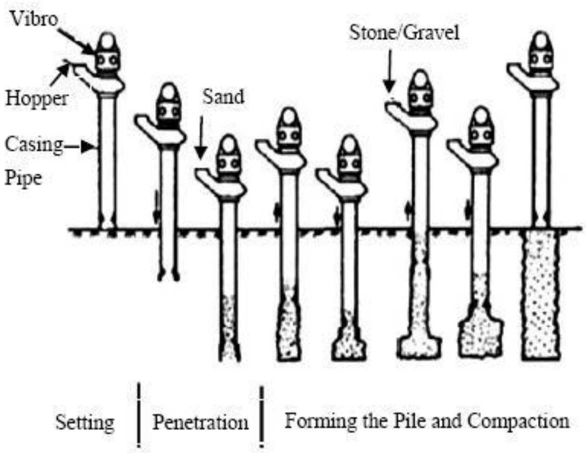

Figure 14: Installation of GCP

Using preloading with GCP, the following are achievable:

- Improved stiffness of the subsoil to decrease settlement.
- Improved shear strength for better stability and increased bearing capacity.
- Rapid consolidation of the subsoil.

Estimated settlements are shown in the Table 2. During the construction, embankment settlement, displacement and pore water pressure will be monitored and checked with the design.

Table 2: Soft Soil Analysis Results

Fill Height (m)	Consolidation Settlement (m)		Residual Settlement after Preloading (m)
	Untreated	With GCP	
8.5	1.295	0.906	0.010
7.6	1.228	0.845	0.007
6.5	1.135	0.761	0.061
5.8	1.068	0.702	0.059

6. Conclusions

The summary of outstanding features of this project is summarized as below:

(1) The first long-span wide deck PC extradosed bridge to be built in Sri Lanka
(2) The first urban elevated long-span steel box girder bridges to be built on wide span steel portal frame piers
(3) Accelerated erection of elevated bridges over heavy traffic roads
(4) Use of bridge high performance steel (500MPa yield stress) for long-span box girders and wide portal frame piers
(5) Soft soil treatment for organic clay with 0.7m diameter gravel compaction piles with consideration of differential settlement between the existing overlay embankment and new embankment
(6) Consideration of long-term durability for stay cables, steel coating specifications and concrete deck

Acknowledgement

Authors wish to express their thanks to Professor J.M.S.J. Bandara, Chairman of RDA and Dr. Asiri Karunawardena, Director General of National Building Research Organization, for their guidance and valuable advice.

References

[1]. Research Group of Steel Products for Bridges, High Performance Steels (For Bridge Construction), Japan Iron and Steel Federation

[2]. Design and Construction for PC Extradosed Bridge Extra-dosed Bridge, Gihodo

[3]. Design of the new extra-dosed bridge over the Kelani River, ICSECM, Kandy, 2015

SECM/15/038

An Experimental Investigation on Thermal Properties of immature Concrete

A.I.G.K. Mataraarachchi[1*], R. Sayanthan[1] and S.M.A. Nanayakkara[1]

[1]University of Moratuwa, Katubedda, Sri Lanka
*E-Mail: geethkumara@gmail.com, TP: +94714396036

Abstract: Since the heat of hydration of cement is highly temperature dependent, variation of thermal properties of concrete at early ages is essential to predict the temperature rise and distribution due to heat of hydration of cement in concrete. Experimental investigation was carried out to obtain the temperature response of fresh concrete sample of 150mm cube with time under known thermal boundary condition. The specific heat capacity of fresh concrete was estimated based on the specific heat capacities of cement and products of cement hydration using Dulong – Petit Rule (DPR) and Neumann– Kopp Rule (NKR). The thermal conductivity (λ) was determined by fitting the temperature response curve of the cube with the temperature history predicted by transient heat conduction analysis based on the estimated specific heat capacity of concrete using ANSYS software. Tests were conducted for concrete at early age, i.e. from one hour to 1 day, for several mix proportions. It was found that thermal conductivity increases rapidly within the first 5 to 12 hours and reached a constant value which depends on the mix proportion.

Keywords: thermal conductivity, specific heat capacity, early age concrete, transient heat conduction analysis

1. Introduction

Thermal properties of concrete is required to obtain temperature rise and distribution in early age concrete which depends on the exothermic hydration process, chemical and physical properties of concrete materials and thermal boundary conditions [1, 2]. Temperature rise and thermal gradient developed at early age can cause cracking in concrete which can affect the long term performance of concrete structures [3, 4].

In cement hydration process, a large quantity, typically 70 ~ 90% of total heat, is released within a day [5] and significantly increase the temperature even above 70 ~ 90 °C depending on the cement type, cement quantity and size of the element[6].

A Multicomponent hydration model has been developed by Maekawa et al. [1, 2] to predict the heat of hydration based on chemical composition and physical properties of cement. This model can be implemented into transient heat conduction analysis program to predict the temperature and temperature gradient for any thermal boundary conditions [6].

Essential thermal and physical input parameters to solve a transient heat conduction analysis are thermal conductivity (λ), specific heat capacity (c), and density (ρ) of concrete.

Results reported in literature on Experimental investigations of thermal conductivity and specific heat capacity of fresh concrete are highly scattered with contradictory results [7, 8, 9, 10, 11, 12]. Thermal conductivity of concrete with limestone aggregates is reported as 3.0 J/s/m/K [9, 10], and concrete with siliceous aggregates such as quartz with higher thermal conductivity is reported in the range of 5.0 ~ 8.0 J/s/m/K [9, 11, 12].

Specific heat capacity of mineral components of cement powder can be estimated based on Dulong-Petit Rule (DPR) and Neumann-Kopp Rule (NKR), and the results are accurate at room temperature [20]. Jindrich et al. [13] reports that many researchers use the estimated specific heat data from DPR & NKR with 3.3% mean deviation to the absolute data. Many authors [14, 15] reported that the specific heat capacity of OPC powder is 0.7 J/g/K which is approximately equal with DPR & NKR estimation. Once the specific heat capacity of components in cement paste is known, the overall specific heat capacity of concrete can be calculated based on mixing theory [24].

Conventional steady state methods to estimate thermal conductivity of fresh concrete, which is a heterogeneous, saturated porous material, produce large errors as the parameters used in estimation are very sensitive [8]. Transient measurement methods reducing moisture movements are desirable to estimate thermal properties of fresh concrete [9].

In this study, with the view of the lack of data on the behaviour of thermal properties of fresh concrete, a specially designed experimental program to determine thermal properties of fresh concrete was conducted.

2. Theoretical Background

2.1 3D Transient Heat Conduction Analysis

The heat diffusion differential equation derived based on Furrier Law and Laplacian with Cartesian coordinate system describing three dimensional heat conduction through homogeneous medium is given by equation 1 [17];

$$\frac{\partial^2 T}{\partial x^2} + \frac{\partial^2 T}{\partial y^2} + \frac{\partial^2 T}{\partial z^2} + \frac{\dot{q}}{\lambda} = \frac{1}{\alpha} \cdot \frac{\partial T}{\partial t} \qquad (1)$$

Where; λ -Thermal conductivity(J/s/m/K), $\alpha = \lambda/\rho c$ thermal diffusivity(m^2/s), c - specific heat capacity(J/kg/K), ρ - density(kg/m^3), and $\dot{q}$ - volumetric heat generation rate (J/s/m^3).

2.2 Dulong – Petit and Neumann– Kopp Rules for Estimation of Specific Heat Capacity of OPC Concrete

Dulong-Petit and Neumann-Kopp rules can be used to estimates the specific heat capacity of concrete mineral components and cement hydrates with the degree of hydration [21, 22]. Dulong-Petit Rule (DPR) states that regardless of the nature of the substance, the specific heat capacity, c_i (J/kg/K) of a solid element is given by equation 2 [21];

$$c_i = \frac{3R}{M} \qquad (2)$$

Where, R is the gas constant equal to 8.3144621 J/mole/K, and M kg/mole is the molar mass of solid substance.

Neumann-Kopp Rule (NKR) states that the specific heat capacity, c per unit mass for alloys can be calculated from the following equation 3 [22];

$$c = \sum_{i=1}^{N} (c_i.f_i) \qquad (3)$$

Where, i is the subsequent number from 1 to N which is the total number of alloy constituents, and f_i is the mass fraction of the i^{th} constituent.

Mixing theory which is similar to NKR states that the specific heat capacity of cement paste and concrete can be given by the equations 4 and 5 [23];

$$c_{paste} = c_{CH}.m_{CH} + c_{UC}.m_{UC} + c_{FW}.m_{FW} \qquad (4)$$

$$c_{conc} = c_{paste}.m_{paste} + c_{sand}.m_{sand} + c_{cagg}.m_{cagg} \qquad (5)$$

Where, c denotes the specific heat capacity of cement paste (CH – cement hydrates, UC – unhydrated cement, and FW – free water), sand and coarse aggregates. Symbol "m" denotes the mass fraction of concrete materials and cement hydrates.

2.3 Sensitivity of Specific Heat Capacity of Concrete to transient heat conduction

A transient heat conduction analysis which is briefed in section 3.3, was carried out using ANSYS software to determine the sensitivity of thermal properties to temperature rise at the centre of a concrete specimen under external heat input. The specimen was modelled as shown in Figure 3.

Initial inside and steady state boundary temperatures were set as $T_{t=0}$ = 30 ºC, and T_o = 40 ºC respectively. Thermal conductivity and specific heat capacity of steel (0.5% Carbon) mould were considered as 54 J/s/m/K, 465 J/kg/K respectively [17].

As many authors reported [9, 10, 11, 12], the thermal conductivity of concrete was selected with an average value of 2.907 J/s/m/K.

Torban C et al. [26] reports that the degree of hydration that can be achieved within a day for OPC is 30%. Bentz [7] reveals that the specific heat capacity of saturated OPC paste with w/c of 0.3 to 0.4, linearly decreases by 14.5%, when the degree of hydration is 30%. Based on this hypothesis, the overall linear reduction in specific heat capacity of concrete including fine and coarse aggregate computed using equation 5, is less than 5.4% from the initial specific heat capacity of OPC concrete. Therefore specific heat capacity of concrete was selected with the maximum value of 1339 J/kg/K adding 5.4% decrease for the sensitivity analysis (see Table 1).

Density of concrete is estimated based on the densities of material in the concrete mix as reported by many authors [7, 8, 14, 15, and 16] and remains unchanged as the total volumetric or mass changes do not occur thorough out the hydration process [26]. Charnockitic gneiss or charnockite, quartzite, marble, dolomite, granulite, migmatite, gneisses and amphibolite are the common Precambrian metamorphic rocks in Sri Lanka [28]. The thermal properties of sand and coarse aggregates are in similar range as sand are naturally created from same rocks origins [29]. The specific heat capacity of gneisses and granulite type rocks are reported in the range of 670 to 1550 J/kg/K [30]. Therefore, the density of concrete was estimated as 2271kg/m^3 to calculate the thermal diffusivity of concrete based on mix M-3.

Table 1: Selected Thermal Properties of Concrete

Thermal Conductivity, λ J/s/m/K	Specific Heat Capacity, c J/kg/K	Thermal Diffusivity, α m^2/s
2.422	1266.69	8.4195E-07
2.422	1339.00	7.9648E-07

Transient heat conduction analysis was performed for a 150 mm concrete cube under external temperature of 40 ºC. It took nearly 1 hour and 40 minutes to reach the centre temperature to external temperature as shown in Figure 1. It can be also seen that change of specific heat from 1339 to 1276 J/kg/K (i.e.5.4% change) has not significantly affected the temperature response curve.

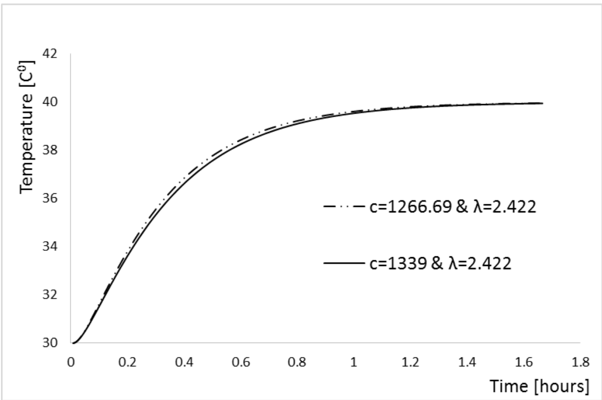

Figure 1: Sensitivity of Temperature Response to Specific Heat Capacity of Concrete

Therefore, thermal conductivity of concrete can be obtained by matching the maximum temperature rise rate of temperature history curves from experiments and transient heat conduction analysis while assuming specific heat capacity being a constant in early age concrete.

3. Experimental Investigation

3.1 Material

In this study the thermal properties of concrete produced with OPC, fine and coarse aggregate available in the local market are considered. The chemical composition, and physical properties of the selected OPC sample are given in Table 2 & Table 3.

Table 2: Percentage of Chemical Composition of OPC

SiO_2	Al_2O_3	Fe_2O_3	CaO	MgO	SO_3	K_2O	Na_2O
20.94	5.31	3.26	63.40	1.22	2.41	0.20	0.00

Table 3: Physical Properties of OPC

Water Demand %	Soundness (mm)	Setting Time		Residu e 45 um	Fineness (cm^2/g)
		Initial (min)	Final (min)		
29.6	1.1	158.0	202.0	9.6	3093

Mineral components in OPC are Alite (C_3S), Belite (C_2S), Aluminate (C_3A), Ferrite (C_4AF), and Gypsum ($(C\dot{S})_3H_2$), where C=CaO, A=Al_2O_3, F=Fe_2O_3, H=H_2O, and $\dot{S}$=SO_3 [6]. Mass proportions of each mineral components were estimated using Bogue method [27] and given in Table 4.

Table 4: Mass Proportions of Mineral Components of OPC

C_3S	C_2S	C_3A	C_4AF	Gypsum
58.59	15.86	8.56	9.92	5.21

3.2 Experimental Setup

The experimental setup shown in Figure 2, consisted of hot water bath connected with thermostat (TST) and thermocouple to maintain constant temperature T_o, Four numbers of standard steel mould were used to cast specimens. Thermocouples were embedded in specimens to measure temperature at the centre of each specimen.

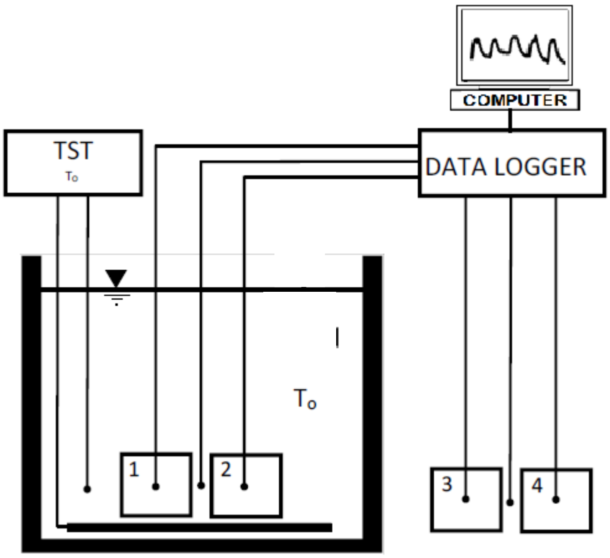

Figure 2: Experimental setup to measure internal temperature rise of specimens using a hot water bath

The steel moulds were carefully filled with the concrete continuously applying vibrations in order to minimize air entrapment. Top surface of the specimens were sealed as shown in Figure 3, to avoid water movement into the specimens.

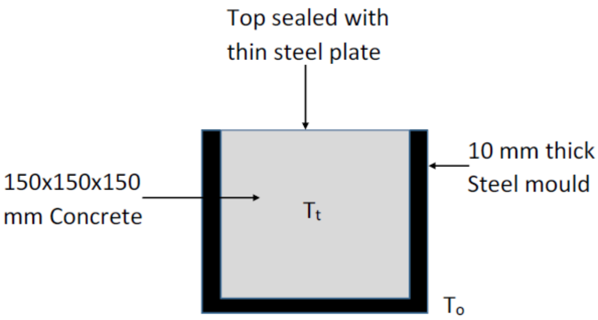

Figure 3: Specimen geometry, dimensions, and boundary conditions

Specimens 1 and 2 were immersed in hot water bath first 2 hours after concrete batching, and the specimens 3 and 4 were placed outside the hot bath exposing to ambient temperature. The temperature at the centre of all specimens were measured at every 30 sec. intervals using a data logger. The specimen 1 & 2 were retained in hot water bath, until the temperature at the centre of specimens were stabilized at the hot bath temperature (T_o). After that, specimens 1 & 2 were removed from the water bath and immersed the specimen 3 & 4 in the hot water bath. Those specimens were kept in the water bath until the temperature at the centre was stabilized. This process was repeated for a duration of 24 hrs. Two specimens were used simultaneously for measuring the temperature response of concrete specimen at a particular age of concrete to minimize the experimental errors. Further these two set of specimens were used to measure temperature response with 10 consecutive time intervals within a day to obtain thermal property variation pattern. Temperature readings were taken at 30 sec. intervals with an accuracy of 0.01 ^oC, and recorded by data logger.

3.3 Finite Element Model to Estimate Thermal Conductivity

A macro program was written to create FEM with APDL (ANSYS Parametric Design Language) to carry out transient heat conduction analysis incorporating initial (T_i) and boundary temperatures (T_0), thermal conductivity, and specific heat capacity of concrete as input parameters to ANSYS software to predict the temperature variation with time at the centre of concrete cube specimen. Time interval was set as 30 seconds as per the experimental conditions.

A three dimensional isoperimetric and eight node solid element was selected for the thermal analysis. In ANSYS, this element type is called SOLID70. The predicted temperature response curves were fitted with temperature response measured from the experiment by adjusting thermal properties of concrete within the relevant time interval.

3.4 Experimental Plan

Initially, same size concrete specimens with similar arrangement were prepared for the selected mix proportions and peak temperature rise due to heat of hydration was monitored. It was found that maximum temperature difference due to hydration was 2.1 ^oC at around 07 hours after batching concrete. Therefore for each time interval (approximately 90 minutes), temperature rise due to heat of hydration is approximately 0.7 ^oC which will not significantly affect the temperature rise due to external heat input from hot water which was kept at 10 ^oC above the ambient temperature.

Furthermore, keeping the temperature difference, T_o–T_i, around 10 ^oC helped to minimize the effect of acceleration of cement hydration process due to heating in the hot water bath [6].

The experimental plan was prepared to investigate thermal properties of fresh concrete with different cement contents, w/c, and aggregate contents as given in Table 5.

Table 4: Mix Proportions considered in the experimental investigation

Mix	Cement (kg/m^3)	Sand (kg/m^3)	Coarse agg. (kg/m^3)	Water (kg/m^3)	w/c Ratio
M-1	395	1032	777	201	0.508
M-2	464	930	758	178	0.384
M-3	482	901	732	156	0.324

Mix proportions were selected by varying the w/c in the range of 0.3 ~ 0.5, and total fine and coarse aggregate content in the range of 1633 ~ 2079 kg/m^3.

Hot water bath temperature for all the specimen was maintained approximately at 40 ^{o}C and the initial temperature for all the specimens was around 30 ^{o}C, which was the mean ambient temperature inside the laboratory. Core temperature of each cube was measured until the inside temperature reached the outside temperature. It took around 01 hour and 40 minutes to achieve this status.

4. Results and Discussion

4.1 Specific Heat Capacity

Specific heat capacities of cement, and concrete were estimated based on equation 2, 3, 4, and 5, and found that the all the measured temperature response curves can be fitted with the specific heat capacity of aggregates at 1150 J/kg/K which is in agreement with the range reported by Julia Chan [30].

Based on DPR, NKR, and mixing theory, the specific heat capacity of cement (OPC) was estimated using the specific heat capacities of C_3S, C_2S, C_3A, C_4AF, and $(C\dot{S})_3H_2$ as 983.3, 1013.7, 1015.5, 923.9, 1347.0 J/kg/K respectively and found as 985.6 J/kg/K. Estimated Specific heat capacities of three mix proportions of concrete considered are given in Table 5.

Table 5: Estimated Specific Heat capacity of Concrete for three Concrete Mixes

Mix	w/c Ratio	Cement Content (kg/m^3)	Water Content (kg/m^3)	Total Aggregate Content (kg)	Specific Heat Capacity, c (J/kg/K)
M-1	0.508	395	201	1809	1377
M-2	0.384	464	178	1688	1348
M-3	0.324	482	156	1633	1323

It can be seen that there is only insignificant variation (4%) in specific heat capacity of concretes with wide variation of w/c (0.508 ~ 0.324) and cement contents (395- 482 kg/m^3).

4.2 Thermal Conductivity

Thermal conductivity of concrete were obtained by fitting with temperature response curve predicted with transient heat conduction analysis using ANSYS, and experimental temperature response data for mixes M-1, M-2, and M-3. Sample analytical fit with measured temperature response data of M-3 specimen 1 & 2 for the time interval between 4 hours 20 minutes ~ 6 hours are given in Figure 4. These curves were fitted with specific heat capacity of 1323 J/kg/K, and thermal conductivity of 2.471 J/s/m/K.

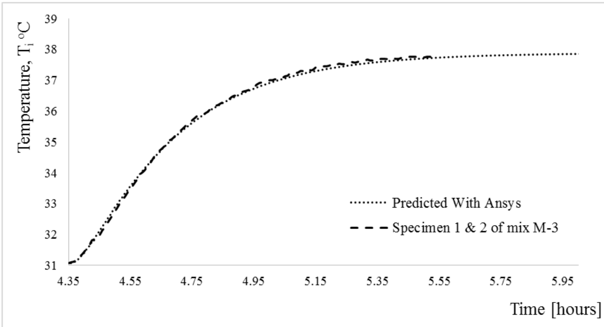

Figure 4: Fitted temperature response curves with relevant experimental data of M-3 specimen 1 & 2

Thermal conductivity obtained based on above described method for three Mixes are shown in Figure 5. The variation of thermal conductivity with time can be expressed as nonlinear curve as shown in Figure 5.

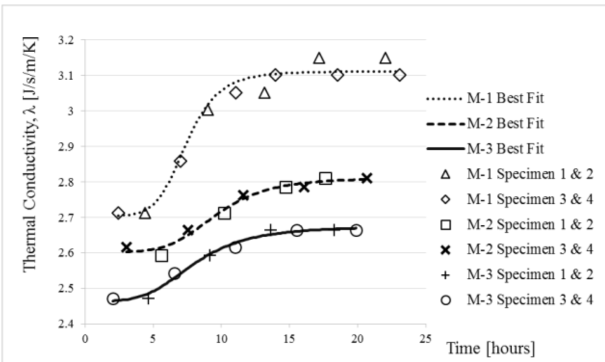

Figure 5: Variation of Thermal Conductivity of Concrete Mixes

It can be seen that the thermal conductivity of OPC concrete follows a unique pattern irrespective of the mix proportions, where it remains constant up to 4 ~ 5 hours and starts to increase up to a maximum value in the range of 2.62 ~ 3.10 J/s/m/K which is fairly in good agreement with values proposed by Kim et al. (2.1 ~ 3.0 J/s/m/K) [9], and Vosteen et al. [10] in previous studies for hardened concrete.

5. Conclusions

Proposed simplified method can be used to investigate thermal properties of fresh and early age concrete.

Specific heat capacities of concrete mixes estimated based on the experimental investigation and rules of Dulong – Petit and Neumann– Kopp are in good agreement with the previous studies.

It was found that the thermal conductivity of concrete increases rapid at early age. The variation of thermal conductivity at fresh state of concrete follows a unique variation irrespective mix proportions, where it remains constant up to 4 ~ 5 hours and starts to increase rapidly and reached a constant value in the range of 2.62 ~ 3.10 J/s/m/K which depends on the mix proportion.

This method can be further developed to study the effect of mix proportion on variation of thermal properties of concrete with hydration and to develop a model to predict the variation of thermal conductivity once the chemical compositions of cement, w/c, and aggregate contents is known.

Acknowledgement

The authors would like to thank the technical staff of the Materials Testing Laboratory in the Department of Civil Engineering at University of Moratuwa for their assistance. Financial assistance from HOLCIM Lanka is gratefully acknowledged.

References

[1]. Y. Suzuki, Y. Tsuji, K. Maekawa, and H. Okumura, Quantification of hydration - heat generation process of cement in concrete, Concrete library JSCE, 1990, No. 16-111-24.

[2]. Koichi Maekawa, Rajesh Chaube, and Toshiharu Kishi, Modelling of concrete performance-Hydration, microstructure formation and mass transport, E&FN Spon, London, 1999.

[3]. Mehta, P.K. and Monteiro, P.J.M., 2006. Concrete, Microstructure, Properties and Materials, McGraw-Hill Companies, Inc., New York, 2006.

[4]. Neville AM. Properties of concrete, 4th edition .Longman, 1995.

[5]. C.M. George, Industrial aluminous cements, P. Barnes (Ed.), Structure and Performance of Cements, Applied Science, London, 1983, pp. 415–470.

[6]. A.I.G.K. Mataraarachchi, S.M.A. Nanayakkara, and Shingo Asamoto, Investigation of temperature rise due to heat of hydration of cement and annual temperature variation related to control of thermal cracking in concrete water retaining structures, SSE, Sri Lanka, 2012.

[7]. D.P. Bentz, Transient plane source measurements of the thermal properties in hydrating cement pastes, Materials and Structures 40 (10) (2007) 1073–1080, 2007.

[8]. Neven Ukrainczyk and Tomislav Matusinović, Thermal properties of hydrating calcium aluminate cement pastes, Cement and Concrete Research 40 128–136, Elsevier Ltd., 2010.

[9]. Kim K.H., Jeon S.E., Kim J.K., and Yang S., An experimental study on thermal conductivity of concrete, Cement Concrete Res 33:363–371, 2003.

[10]. Vosteen HD, Schellschmidt R, Influence of temperature on thermal conductivity, thermal capacity, and thermal diffusivity for different types of rocks, Phys Chem Earth 28:499–509, 2003.

[11]. Bouguerra A., Laurent J.P., Goual M.S., and Queneudec M., The measurement of the thermal conductivity of solid aggregates using the transient plane source technique. J Phys D: Appl Phys 30:2900–2904, 1997.

[12]. Horai K., Thermal conductivity of rock-forming minerals, J Geophys Res 76(5):1278–1308, 1971.

[13]. Jindrich Leitner, Pavel Chuchvalec, David Sedmidubsky, Ales Strejc, and Petr Abrman, Estimation of heat capacities of solid mixed oxides, Thermochimica Acta 395 (2003) 27-46, Elsevier Ltd., 2003.

[14]. Yunsheng Xu, and D.D.L. Chung, Cement of high specific heat and high thermal conductivity, obtained by using silane and silica fume as admixtures, Cement and Concrete Research 30 (2000) 1175-1178, Pergamon, 2000.

[15]. Todd S.S., Low-Temperature heat capacities and entropies at 298.16 K of crystalline calcium orthosilicate, zinc orthosilicate, and tricalcium silicate, J Am Chem Soc 73:3277–3278, 1951.

[16]. Harmathy, T. Z., Thermal Properties of Concrete at Elevated Temperatures, J. of Materials, 5(1), 47-74, 1970.

[17]. John H. Lienhard, Heat Transfer Text Book, Cambridge, Massachusetts, U.S.A., 2000.

[18]. D.A. De Vries, The theory of heat and moisture transfer in porous media revisited, International Journal of Heat and Mass Transfer 30 (7) 1343–1350, 1987.

[19]. P. Mounanga, A. Khelidj, G. Bastian, Experimental study and modelling approaches for the thermal conductivity evolution of hydrating cement paste, Advances in Cement Research 16 (3) 95–103, 2004.

[20]. Andreas Kleiven, and Helge Skarestad, Specific Heat Capacity of Metals, TFY4165 Termisk fysikk, Nttnu, 2014.

[21]. Landau, L.D. Lifshits, E.M., Statistical Physics Pt. 1. Course in Theretical Physics 5 (3rd ed.), Oxford: Pergamon Press. P. 193,196.ISBN 0-7506-3372-7, 1980.

[22]. Frederick Seitz, The Modern Theory of Solids, McGraw-Hill, New York, USA, ASIN: B000OCK08, 1940.

[23]. Waller V., De Larrard F., Roussel P. Modelling the temperature rise in massive HPC Structures. In 4th International Symposium on Utilization of High-Strength/High-Performance Concrete RILEM, Paris, 415–421, 1996.

[24]. Choktaweekarn P., Saengsoy W. and Tangfermsirikul S., A model for predicting the specific heat capacity of fly-ash concrete, Science Asia 35: 178–182, 2009.

[25]. Tuson A., and Charman R., Thermal Material Properties for Modelling of the 2 Metre Box, A report produced for NDA-RWMD, L6677228, Inutec(10)p019 Issue 1, NDA, UK, 2012.

[26]. Torben C. Hansen, Physical structure of hardened cement paste. A classical approach, Material and Structures, 19 6(1986) 423-436, Denmark, 1986.

[27]. Peter C. Hewlett, “Lea’s chemistry of cement and concrete”, Elsevier Science & Technology Books, London, 2004.

[28]. U. de S. Jayawardena, Correlations between Some Strength Properties of Metamorphic Rocks of Sri Lanka, Journal of Geological Society of Sri Lanka, Vol. 14 (2011): 65-69, 2011.

[29]. L.J.D. Fernando, Mineral Resources of Sri Lanka, Natural Resources, Energy and Science Authority, Colombo, Sri Lanka, 1986.

[30]. Julia Chan, Thermal properties of concrete with different Swedish aggregate materials, Lund University, Sweden, 2013.

[31]. E.W. Lemmon, M.O. McLinden, D.G. Friend, Thermo physical properties of fluid systems, P.J. Linstrom,W.G. Mallard (Eds.), NIST Chemistry WebBook, NIST Standard Reference Database Number 69, National Institute of Standards and Technology, Gaithersburg MD, 2005

SECM/15/080

Vertical Uplift Capacity of a Group of Equally Spaced Helical Screw Anchors in Sand

S. Mukherjee [1*] and Dr. S. Mittal [2]

[1]Amity University, Noida, India
[2] Indian Institute of Technology, Roorkee, India
*E-Mail: Corresponding author @ pqr.com, TP: +94975500500

Abstract: This paper presents the experimental investigations on the behaviour of a group of single, double and triple helical screw anchors embedded vertically at the same level in sand. The tests were carried out on one, two, three and four numbers of anchors in sand for different depths of embedment keeping shallow and deep mode of behaviour in mind. The testing program included 48 tests conducted on three model anchors installed in sand whose density kept constant throughout the tests. It was observed that the ultimate pullout load varied significantly with the installation depth of the anchor and the number of anchors. The apparent coefficient of friction (f^*) between anchor and soil was also calculated based on the test results. It was found that the apparent coefficient of friction varies between 1.02 and 4.76 for 1, 2, 3 and 4 numbers of single, double and triple helical screw anchors. Plate load tests conducted on model soil showed that the value of ϕ increases from 35º for virgin soil to 48º for soil with four double screw helical anchors. The graphs of ultimate pullout capacity of a group of two, three and four no. of anchors with respect to one anchor were plotted and design equations have been proposed correlating them. Based on these findings, it has been concluded that the load-displacement relationships for all groups can be reduced to a common curve. A 3-D finite element model, PLAXIS, was used to confirm the results obtained from laboratory tests and the agreement is excellent.

Keywords: Apparent Coefficient of Friction, Helical Screw Anchor, Installation Depth, Plate Load Test.

1. Introduction

Anchors are prefabricated foundations which are used for almost all types of structures e.g. transmission towers, radar towers, tall chimneys, suspension bridges, offshore structures, aircraft moorings, tunnels, buried pipelines under water etc. Anchors are structural elements used in Civil engineering applications to provide resistance against tension, compression and uplift. The past studies on pullout capacity and associated soil deformations of the anchors are very limited. Most of the studies on anchors have been carried out on horizontal anchors and there are much less research work reported on inclined and vertical anchors. Anchors are manufactured in variety of configurations such as plate anchors, pile anchors, grouted anchors, prestressed concrete anchors and single and multiple helical screw anchors. For helical screw anchors, screws are welded at a predetermined suitable spacing along the steel shaft. A screw anchor is installed in the ground by applying torque to the shaft. An axial compression force is applied to the shaft for its advancement into the soil.

The works on single helical screw anchor are many. However, hardly any work is available that examines the interference effect on the pullout capacity of a group of closely spaced anchors. Anchors are seldom used alone. They are always used in groups. Hence, the behaviour of group of anchors is of considerable importance. But very little literature has been published on the topic. In the present study, the influence of a group of 2, 3 and 4 no. of helical screw anchors having equal dimensions and placed vertically in a cohesionless medium, on the magnitude of the vertical uplift resistance has been examined. The test results reported are aimed to suggest empirical approach for design of group of anchors subject to tensile loads.

Meyerhof and Adams (1968) developed an expression to predict the anchor uplift capacity. They had concluded that the geometry of the failure surface is fairly distinct but varies in shape and extent with the H/B ratio and depends on the relative density of the sand. Laboratory vertical pulling tests on groups of circular anchors in sand have been reported by Hanna et al. (1972). The anchors were in groups of up to 25, at various spacing and at depth/diameter ratios of 6 and 12. The ultimate group resistances were compared with the theoretical values of Meyerhof and Adams (1968), and it was concluded that, although the theory predicted behavioral trends, the theoretical failure values were considerably in error. Meyerhof (1973) conducted experiments for identical test conditions and concluded that the pullout capacity of axially loaded inclined plate anchors exceeded that of vertical anchors.

Laboratory tests on steel ball anchors embedded in sand and pulled at angles of inclination up to 55º from the vertical have been reported by Larnach (1972 and 1973) for two anchors and for line groups of three and five anchors. In these tests the depth/diameter ratio was constant at 16, thus ensuring deep anchor behavior. He reported that the initial slope of the load pullout curve for grouped anchor plates is essentially linear and independent of inclination, spacing, and number of anchors in the group.

One thing common in all the above mentioned studies is that they are limited to anchors with a single helix. The proposed semi-empirical theories cannot be easily applied to the problem of multi-helix anchors in which a complication arises owing to the interaction between adjacent helices. This interaction can produce overlapping stress zones that affect the failure mode and ultimate capacity, as highlighted by Merifield and Smith (2010). Mitsch and Clemence (1985) suggested that the ultimate uplift resistance is made of the bearing resistance of the upper helix, frictional cylinder resistance and friction on anchor shaft. Ghaly and Hanna (1991) conducted experimental investigation on single and multiple helical screw anchors installed in dense, medium and loose dry sands. They concluded that the ultimate pullout capacity of screw anchors was a function of sand characteristics, anchor diameter and installation depth of anchor.

In general, anchor capacity is a function of (a) soil type and density; (b) the capacity of each individual bearing element (i.e. plate or helix); (c) the adhesion between the plate/shaft and surrounding soil; (d) the interaction between each bearing element; (e) the orientation of the anchor; and (f) the embedment depth. Any combination of these variables will significantly affect the observed mode of failure and thus the ultimate capacity of a buried anchor in tension.

The objectives of the present study are to develop understanding of multiplate anchor behaviour, their failure mechanism and to develop understanding of the interference effect on the pullout capacity of a group of closely spaced anchors. In the present work the experiments had been conducted to study the behaviour of helical screw anchors under application of axial pullout load by varying the number of anchors, number of screw blades in an anchor and installation depth. The present paper describes the behaviour (in laboratory scale) of group of helical screw anchors pulled vertically upward in medium dense sand. Here in this experimental investigation only one density of sand was used throughout. Also the spacing of the anchors was kept constant equal to 2.5 times the diameter of the screw of the anchor. In the published literature, this spacing was mentioned as one in which no interference happens from the adjacent anchors.

2. Experimental Setup

Laboratory tests were conducted to determine the uplift resistance of helical screw anchors. Although laboratory tests are not substitute of full scale field tests but tests at laboratory have an advantage of allowing a close control on some of the parameters affecting the uplift resistance of helical screw anchors. In this way behaviour of the small size anchor models in the laboratory could be of immense help in asserting the behaviour of full scale anchors in the field in actual condition. The experimental setup used for this work and the procedure adopted for testing of single and multiple helical screw anchors are described elsewhere Mittal & Mukherjee (2013). In this paper, the properties of soil and anchor, the test tank and the loading frame used in the experiments had been described in detail.

3. Test Procedure

Here it was assumed that at any stage, all the anchors,

I. Carry an equal magnitude of load, and,

II. Settle exactly to the same extent.

It was also assumed that during loading no tilting takes place and the anchors are perfectly rigid. Anchors were installed in the ground at a depth of 4, 6, 8 and 10 times the diameter of the screw of the anchor. The three dimensional view of the experimental setup is illustrated in Fig. 1.

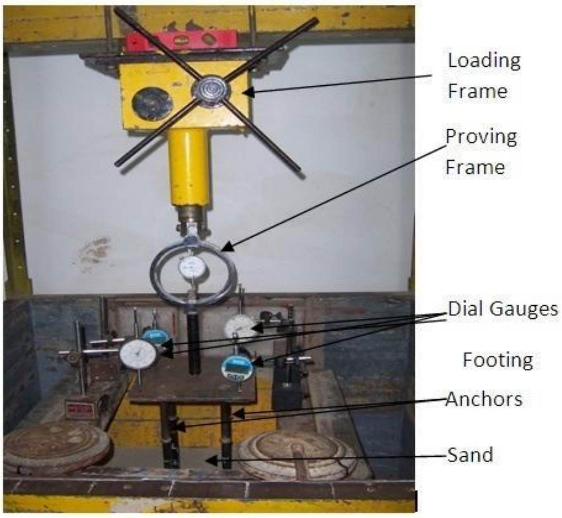

Figure 1: Complete setup for Pull-out Test of 4 Helical Screw Anchors

4 Parametric Study

Parametric study was conducted to determine the improved apparent coefficient of friction (f*) between the anchor and the soil and also increase in the value of angle of internal friction due to installation of anchor in soil.

Apparent coefficient of friction between the anchor and the soil (f*) plays an important role in determining the strength of anchors. In these experiments the value of f* ranged between 1.02 and 4.76. Typical values of f* for a group of 1, 2, 3 and 4 anchors are shown in the Table 1.

Table 1: Values of f* for a group of N_a = 1, 2, 3 and 4 helical screw anchors

n_b	H/B	f*			
		N_a=1	N_a=2	N_a=3	N_a=4
1	4	1.34	1.02	1.07	1.06
1	6	2.14	1.53	1.44	1.41
1	8	3.29	2.3	2.05	2.06
1	10	3.22	1.99	2.34	2.08
2	4	1.95	1.6	1.49	1.57
2	6	2.99	1.9	1.9	1.89
2	8	3.88	2.51	2.37	2.43
2	10	3.78	2.65	2.78	2.41
3	4	2.28	1.95	1.82	1.86
3	6	4.02	2.53	2.57	2.58
3	8	4.76	2.92	2.91	2.92
3	10	4.44	3.08	3.02	2.82

The increase in the value of φ can be calculated from the plate load test. The plate load tests were conducted on virgin soil and also on soil with 1, 2, 3 and 4 double helical screw anchors. A plate of dimension 150 X 150 mm was fixed on the top of the anchor with the help of nuts and bolts.

The ultimate bearing capacity for square footing was computed from the equation

$$q_u = 0.4\gamma_d \ B \ N_\gamma \quad \ldots\ldots\ldots\ldots\ldots\ldots\ldots\ldots\ldots\ldots.. \quad (1)$$

where, q_u is ultimate bearing capacity, γ_d is dry unit weight of soil = 15.7 kN/m^3, B is width of the footing plate= 150 mm and N_γ = bearing capacity factor. Putting above values eq. 1 becomes as,

$$q_u = 0.942 \ N_\gamma \quad \ldots\ldots\ldots\ldots\ldots\ldots\ldots\ldots\ldots\ldots.............(2)$$

The value of q_u was obtained from plate load tests for each test condition (i.e. on virgin soil and with 1, 2, 3 and 4 double helical screw anchors). The value of N_γ was then obtained by using Eq. 2. The value of φ for a particular N_γ was obtained from Mittal and Shukla (2009). The values of q_u, N_γ and corresponding φ are shown in Table 2.

This table shows that the value of angle of internal friction of the soil increased to approx 48^o after placing 4 screw anchors whose value was approx 37^o initially without any anchor. This indicates a significant increase in the value of φ after insertion of helical screw anchor.

Table 2: Values of increased φ for double helical screw anchor

Soil and Anchor	q_u (kN/m^2)	N_γ	φ
Virgin soil	69.76	74.05	37.12
Soil with 1 anchor	174.42	181.69	42.23
Soil with 2 anchors	283.41	295.22	45.24
Soil with 3 anchors	392.4	408.75	46.39
Soil with 4 anchors	566.8	590.42	48.24

5 Test Results and Discussions

Total 48 pullout (tension) tests were conducted by varying the following parameters

1. No. of anchors (N_a = 4, 6, 8 and 10)

2. No. of screw blades in anchor (n_b = 1, 2 and 3)

3. H/B ratio of anchor (H/B = 4, 6, 8 and 10) where H is the depth of the bottom of the anchor from the soil surface and B is the diameter of the screw blade.

The values of the ultimate pullout load of 1, 2, 3 & 4 numbers of helical screw anchors obtained from laboratory testing are tabulated in Table 2.

Table 2 Ultimate Pullout Loads of 1, 2, 3 & 4 Anchors Obtained from Laboratory Tests

n_b	H/B	$(Q_{up})_1$ (N)	$(Q_{up})_2$ (N)	$(Q_{up})_3$ (N)	$(Q_{up})_4$ (N)
1	4	93	137	221	294
1	6	373	539	760	991
1	8	1079	1545	1991	2747
1	10	1717	2158	3823	4513
2	4	118	196	270	392
2	6	490	613	883	1275
2	8	1226	1619	2197	3139
2	10	1962	2796	4414	5101
3	4	132	245	319	441
3	6	638	736	1177	1619
3	8	1471	1767	2600	3679
3	10	2256	3188	4689	5837

In the present experimental investigation, the experiments were carried out on a group of 2, 3 and 4 number of anchors arranged in linear, equilateral triangle and square pattern respectively.

An attempt has been made to express ultimate pullout capacity of multiple anchors in terms of single anchor. This is because it is relatively easy to test and analyse single anchor compared to multiple anchors. Keeping this point in mind the graphs of ultimate pullout capacity of multiple anchors with respect to single anchor have been plotted. A sample graph for four anchors versus one anchor is shown in Fig. 2. These curves provide the equations for ultimate pullout capacity of multiple anchors in terms of 1 anchor.

Based on the equations obtained for 2, 3 and 4 number of helical screw anchors from plots of ultimate pullout capacity of multiple helical screw anchors versus single helical screw anchor, a single equation for the determination of the ultimate pullout capacity of multiple anchors is proposed as mentioned in Equation 1.

$$(Q_{up})_n = N_a \, (Q_{up})_1^{\,m} \qquad (1)$$

where, $(Q_{up})_n$ = ultimate pullout capacity of multiple helical screw anchors where n=2, 3 and 4 in our study, N_a = number of anchors whose value is equal to 2 for two number of anchors, 3 for three number of anchors and 4 for four number of anchors, $(Q_{up})_1$ = ultimate pullout capacity of single helical screw anchor and, m= a constant whose value we proposes as 0.95.

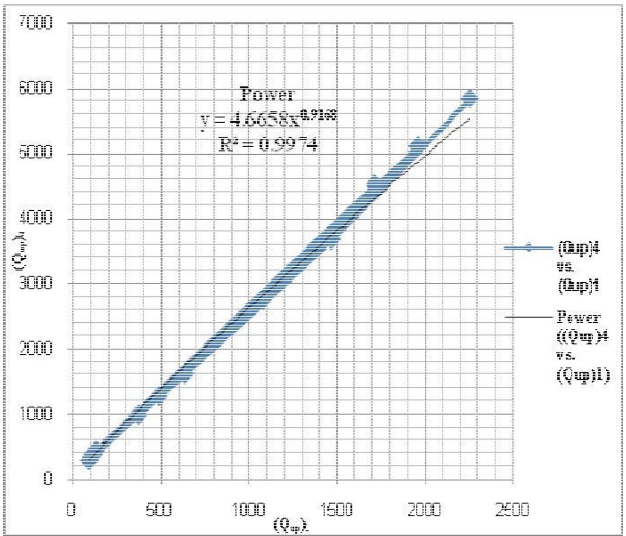

Fig. 2 Graph of ultimate pullout capacity of 4 anchors versus 1 anchor

By assuming the values of m and n as mentioned above, the values of ultimate pullout capacity of 2, 3 and 4 number of helical screw anchors has been calculated using Eq.1 as mentioned in Table 3. Now two sets of values of ultimate pullout capacity of 2, 3 and 4 number of helical screw anchors are available – one from the experimental investigation carried out in the laboratory, and the other from the equations proposed for multiple number of helical screw anchors as mentioned in Equation (1).

The empirical equation proposed here has some limitations.

Table 3 Ultimate Pullout Loads of 2, 3 & 4 Anchors Based on Equation Proposed

n_b	H/B	$(Q_{up})_2$ (N)	$(Q_{up})_3$ (N)	$(Q_{up})_4$ (N)
1	4	148	222	296
1	6	554	831	1108
1	8	1516	2274	3032
1	10	2370	3555	4740
2	4	186	279	372
2	6	716	1074	1432
2	8	1716	2574	3432
2	10	2682	4023	5364
3	4	206	309	412
3	6	926	1389	1852
3	8	2036	3054	4072
3	10	3062	4593	6124

(1) This is presuming that embedment depth, diameter and material of the anchor are same.

(2) All the soil properties i.e. relative density and angle of internal friction are same.

6 PLAXIS Finite Difference Analysis

The main objective of modeling helical anchor behaviour was to define the failure mechanism and load transfer behaviour. Upon calibration-verification with the experimental data, FEM provided insight into the effects of anchor loading on the surrounding soil. Based on the findings of the model and full-scale load test results, a methodology for calculating the anchor capacity was developed.

To account for the unique geometry of the problem a three-dimensional soil-foundation interaction software program, namely PLAXIS 3D Foundation Suite, was selected. A linearly elastic perfectly plastic model namely Mohr–Coulomb model was selected from those available in PLAXIS to describe the non-linear sand behaviour in the work. PLAXIS incorporates a fully automatic mesh generation procedure, in which the geometry is divided into elements of basic element type, and compatible structural elements. Five different mesh densities are available in PLAXIS ranging from very coarse to very fine. In this study fine mesh was adopted throughout which was shown in Fig. 3.

The numerical model was constructed to match the full scale geometry of the anchor in all regards excluding the helical shape of the bearing plates, which were modeled as circular discs rather than pitched plates. The Mohr–Coulomb model was used to represent the soil behaviour, for which cohesion and friction angle values were obtained through triaxial test results.

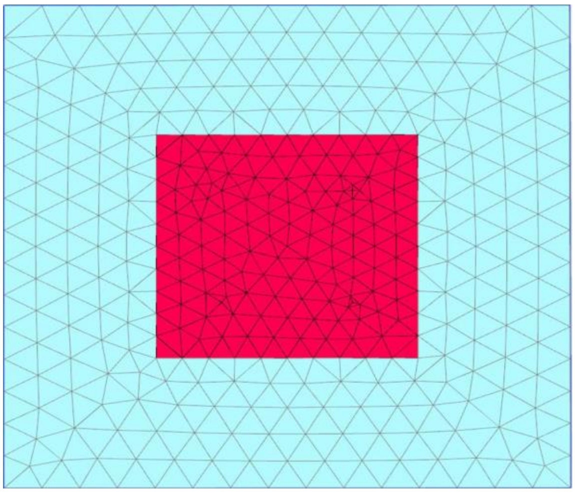

Fig. 3 Fine Mesh used in PLAXIS analysis

Values of soil parameters used in the investigation are shown in Table 4.

The helical screw anchor is represented by node-to-node anchor coupled with a circular plated attached to it. In PLAXIS soil/structure interface behaviour may be modeled using parameters generated using an interaction coefficient, Ri defined as the ratio between the shear strength of soil/structure interface and the corresponding shear strength of the soil. Fully rough interface conditions, $R_i = 1$, were assumed in this study.

Table 4: Properties of soil used in PLAXIS

Type of Soil	Loose	Medium Dense	Dense
c (Pa)	0	0	0
Φ	28	32 and 36	38 and 40

γ_d (kN/m^3)	13.73	15.7	17.66
N	0.25	0.3	0.4
E (MPa)	20	40	65

7 PLAXIS Results

In PLAXIS, pullout tests were carried out for embedment depth ratio of 4, 6 and 8. PLAXIS pullout results for 3 no. of anchors are shown in Table 5.

Table 5: PLAXIS Results of Pullout Tests for N_a=3

n_b	H/B	Φ (Degree)	γ (kN/m^3)	Failure Load, P_f (N)
1	4	32	15.7	716
1	4	40	13.73	167
1	6	38	15.7	245
1	6	40	17.66	284
1	8	32	15.7	355
2	4	32	15.7	148
2	6	38	15.7	85
2	6	40	17.66	282
2	8	36	13.73	442
3	4	32	15.7	147
3	4	36	15.7	163
3	4	38	15.7	85
3	6	38	15.7	192
3	6	40	17.66	232
3	8	36	13.73	430
3	8	36	17.66	533

To validate the results obtained from the laboratory tests, comparison of its results were done with PLAXIS results. This comparison was done in non-dimensional form. For comparison purpose a non-dimensional factor $P_f/(\gamma_d BH\delta_f)$ was defined where P_f is the failure load, γ_d is the unit wt. of sand, B is the diameter of the helical screw of the anchor, H is the embedment depth of the anchor and δ_f is the deformation of the anchor at failure.

The results obtained by conducting PLAXIS runs on the model similar to the one on which laboratory experiments were conducted were compared with results obtained by laboratory experiments themselves. Table 6 shows the comparison in non-dimensional form. From this table it is clear that the difference between laboratory test and PLAXIS results is within 10% which can be neglected.

Table 6: Comparison of Non-dimensional Parameter $P_f/(\gamma_d BH\delta_f)$ from Laboratory Experiment and PLAXIS Run for Pullout Tests

N_a	n_b	H/B	$P_f/(\gamma_d BH\delta_f)$		% diff
			LAB Test	PLAXIS	
1	1	4	759.43	694.32	8.56
1	1	6	529.15	562.21	6.05
1	2	6	203.99	184.14	9.36
1	3	6	304.39	279.05	8.22
2	1	6	208.25	186.61	10.09
2	2	6	179.51	161.88	9.49
2	3	6	289.38	260.78	9.69
3	1	6	258.16	232.95	9.69
3	2	6	305.29	278.83	8.52
3	3	4	1737.88	1923.37	9.62
4	1	4	435.49	400.20	8.04
4	1	6	344.23	311.16	9.59
4	3	4	2956.75	2734.12	7.54

8 Conclusions

The effect of interference due to a number of multiple helical screw anchors placed vertically in a granular sandy medium at different embedment depths has been investigated in this work by conducting a series of small scale model tests. As compared to the single isolated anchor, a group of two, three and four anchors yields a greater magnitude of uplift resistance.

Ultimate pullout capacity of helical screw anchor increase with increase in the embedment depth ratio of the anchor, no. of anchors and no. of screw blades in the anchor. Moreover, the increase is more pronounced with embedment depth ratio and no. of anchors whereas with no. of screw blades the increase is very marginal.

The ultimate aim of this work was to express ultimate pullout capacity of multiple helical screw anchors in terms of single helical screw anchor. So we have plotted graph of ultimate pullout capacity of 2, 3 and 4 number of anchors with respect to one anchor. In this way we have found equations to calculate ultimate pullout capacity of multiple anchors in terms of one anchor. The percentage difference between the values of ultimate pullout load obtained from laboratory tests and from the equation proposed falls within 10%. Hence it can be said that the proposed equation designs the anchors assembly amicably.

Acknowledgements

The research is supported by a fellowship to second author from MHRD, Govt. of India. This support is gratefully acknowledged.

References

[1] Ghaly, A. M. and Hanna, A. M. (1991), "Uplift behaviour of screw anchors in sand.1: Dry Sand", J. Geotech. Engg. ASCE, 117 (5), pp. 773-793.

[2] Hanna TH, Sparks R, Yilmaz M (1972), "Anchor behavior in sand", J Soil Mech Found Div ASCE, Vol. 98, No. 11, pp. 1187–1207.

[3] Larnach WJ (1972), "The pull-out resistance of inclined anchors installed singly and in groups in sand", Ground Eng 5(4):14–17.

[4] Larnach WJ (1973), "Anchors 3-the behavior of grouped inclined anchors in sand", Ground Eng 6(6):34–41.

[5] Merifield and Smith (2010), "The ultimate uplift capacity of multiplate strip anchors in undrained clay", Computer Geotechnics, Vol. 37, No. 4, pp. 504–514.

[6] Meyerhof, G. G., and Adams, J. I. (1968), "The ultimate uplift capacity of foundations", Canadian Geotech. J., Vol. 5, No. 4, 224-244.

[7] Meyerhof, G. G. (1973), "Uplift resistance of inclined anchors and piles", Proceedings of 8th ICSMFE, Vol. 2, pp. 167-172.

[8] Mitsch, M. P., and Clemence, S. P. (1985), "The uplift capacity of helix anchors in sand: Uplift behaviour of anchor foundation in soil", Proceedings. ASCE New York, 26-47.

[9] Mittal, S. and Mukherjee, S. (2013), "Vertical uplift capacity of a group of helical screw anchors in sand", Indian Geotechnical Journal, Vol. 43, No. 3, pp. 238-250.

[10] Mittal S, Shukla JP (2009) Soil testing for engineers. Khanna Publishers, India

SECM/15/108

Vibration Characteristics of Various Wide Flange Steel Beams and Columns

H.F. Ozel[1], A. Saritas[1,*] and T. Tasbahji[1]

[1] Middle East Technical University, Ankara, Turkey
[*]E-Mail: asaritas@metu.edu.tr, TP: +90 312 210 5458

Abstract: Vibration characteristics of steel framed structures are affected by accurate modelling of the mass and stiffness matrices of beam and column members. In this regards, wide flange sections are the most popularly used steel sections, and calculation of axial, flexural and shear responses of these sections become critical. In this study, a mixed formulation frame finite element is developed from three-fields Hu-Washizu-Barr functional. Consistent mass matrix of the element is obtained such that determination of vibration frequencies of members with varying geometry and material distribution is modelled without any need for specification of different displacement shape functions for each individual case. An accurate shear correction coefficient for wide flange I and H sections is taken into account in order to get closer match with exact solutions. Comparative study is undertaken by the use of proposed beam finite element solutions and 3 dimensional solid finite element analyses in ANSYS. Results indicate that proposed beam finite element can get fundamental and higher modes of vibration for varying aspect ratios of wide flange beams and columns.

Keywords: Steel framed structures; Wide Flange Sections; Finite element modelling; Vibration characteristics

1. Introduction

The strength of the members in a structure determines the performance of the whole system. Likely, deformations have crucial influence on the serviceability of the structures, where different types of deformations have consequential effects on each other due to the continuum phenomenon of the bodies. Shear deformations can be crucial for the determination of the lateral flexibility of steel moment resisting frames. The study by Charney et al. [1] clearly shows the effects of shear deformations for various structural steel beam and column sections. Consideration of the shear effects on the members are provided via the definition of effective shear area. The studies on the shear effects of the cross sections on linear basis [2] or nonlinear basis [3, 4] presented various ways to take into account such effects.

In this study, the members examined in [1] that are W36x135, W24x250 and W14x730 sections and European sections that are HEB180, IPE270 and IPE750x147 are modelled with ANSYS [5] finite element program to verify the performance of the proposed beam model in this paper. The beam finite element model proposed in this research study relies on Hu-Washizu-Barr variational. In order to calculate an accurate stiffness and mass matrix, force-based interpolation functions are used, and the shear correction coefficient suggested by [1] is adopted.

2. Frame Element Formulation

2.1 Kinematic Relations

Displacements on a material point on the section of a beam that deforms in *xy*-plane can be obtained through Timoshenko beam theory as follows;

$$\begin{Bmatrix} u_x(x,y) \\ u_y(x,y) \end{Bmatrix} = \begin{Bmatrix} u(x) - y\theta(x) \\ v(x) \end{Bmatrix} \quad (1)$$

where u_x(x,y) and u_y(x,y) are the displacements in *x* and *y* directions, respectively of any point in the section. $u(x)$ is the displacement of the point (x,0) along *x*-axis. $v(x)$ is the transverse deflections of the point (x,0) from *x*-axis in *y* direction. $\theta(x)$ is the small rotation of the beam cross section around *z*-axis.

The non-zero strain components $\boldsymbol{\varepsilon}$ include the normal strain in the *x* direction and shear strain with *xy* component, where these are calculated from section deformations as follows;

$$\boldsymbol{\varepsilon} = \begin{Bmatrix} \varepsilon_{xx} \\ \gamma_{xy} \end{Bmatrix} = \begin{Bmatrix} u'(x) - y\theta'(x) \\ -\theta(x) + v'(x) \end{Bmatrix} = \begin{Bmatrix} \varepsilon_a(x) - y\kappa(x) \\ \gamma(x) \end{Bmatrix} = \mathbf{a}_s(y,z)\,\mathbf{e}(x) \tag{2}$$

where $\mathbf{e}(x)$ is the section deformation vector given as follows;

$$\mathbf{e}(x) = \begin{bmatrix} \varepsilon_a(x) & \gamma(x) & \kappa(x) \end{bmatrix}^{\mathrm{T}} \tag{3}$$

In Equation (3), $\varepsilon_a(x)$ is the axial strain of the reference axis, $\gamma(x)$ is the shear deformation along y-axis and κ is the curvature about z-axis. Section deformations can be easily obtained from section reference displacements through a one to one comparison of the terms in Equation (2). Furthermore, section compatibility matrix, $\mathbf{a}_s(y,z)$ introduced in Equation (2) is written as follows;

$$\mathbf{a}_s(y,z) = \begin{bmatrix} 1 & 0 & -y \\ 0 & 1 & 0 \end{bmatrix} \tag{4}$$

2.2 Basic System without Rigid Body Modes and Force Interpolation Functions

Element formulation is proposed in xy-plane, where the formulation considers two end nodes and relies on a transformation from complete system to basic system. In the whole structure, the element has 3 degrees of freedom (dof) per node, resulting in 6 dofs in total, where the nodes are placed at element ends. The complete system is proposed such that the axis of the element is aligned with horizontal x-axis. The basic system is prescribed for the purpose of removing rigid body modes of motion, and the basic system is chosen as the cantilever beam as shown in Figure 1, where the fixed and free ends are the left and right ends, respectively. The transformation matrix, **a** for an element with length L is used to relate element end forces in complete system to basic element forces as follows;

$$\mathbf{p} = \mathbf{a}^{\mathrm{T}}\mathbf{q}; \quad \text{where} \quad \mathbf{a} = \begin{bmatrix} -1 & 0 & 0 & 1 & 0 & 0 \\ 0 & -1 & -L & 0 & 1 & 0 \\ 0 & 0 & -1 & 0 & 0 & 1 \end{bmatrix} \tag{5}$$

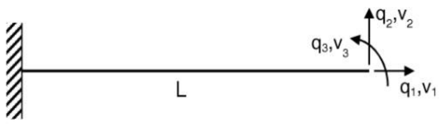

Figure 1:Cantilever basic system forces and deformations

It is also possible to relate basic element deformation vector **v** to displacements in complete system by separating 3 rigid body modes and keeping only the basic deformation modes for the element. By this way, it is feasible to derive flexibility matrix that would have been impossible to get in the complete system because of the singularity caused by rigid body modes. Basic element deformations **v** can be calculated from nodal displacements **u** in complete system as follows;

$$\mathbf{v} = \mathbf{a}\mathbf{u} \tag{6}$$

Basic element forces at free end, **q** are shown in Figure 1 and given in Equation (5). These forces can be related to internal section forces, $\mathbf{s}(x)$ by using the force interpolation matrix $\mathbf{b}(x,L)$ for the cantilever beam configuration as follows;

$$\begin{gathered} \mathbf{s}(x) = \begin{bmatrix} N(x) & V(x) & M(x) \end{bmatrix}^{\mathrm{T}} = \mathbf{b}(x,L)\,\mathbf{q} + \mathbf{s}_p(x) \\ \mathbf{b}(x,L) = \begin{bmatrix} 1 & 0 & 0 \\ 0 & 1 & 0 \\ 0 & (L-x) & 1 \end{bmatrix} \quad \text{and} \\ \mathbf{s}_p(x) = \begin{bmatrix} L-x & 0 \\ 0 & L-x \\ 0 & (L-x)^2/2 \end{bmatrix} \begin{Bmatrix} w_x \\ w_y \end{Bmatrix} \end{gathered} \tag{7}$$

By using Equation (7), it is possible to attain exact equilibrium between the forces at free end of the element and forces at any section that is x units away from the fixed end. Section forces are axial force $N(x)$, shear force in y direction $V(x)$, and moment about z-axis $M(x)$. In above equation $\mathbf{s}_p(x)$ is the particular solution for uniformly distributed loads in the axial and transverse directions, i.e. w_x and w_y, respectively. By the way, with this approach, it is easy to calculate the particular solution under arbitrary inter element loads that are concentrated or distributed.

2.3 Variational Base and Finite Element Formulation of the Element

Variational form of the element is written by considering independent element nodal displacements **u**, element basic forces **q**, and section deformations **e** by using three-fields Hu-Washizu functional and implemented as part of beam finite elements by Taylor et al. [6] and Saritas and Filippou[7]. Extension to dynamic case is achieved through introduction of inertial forces $\mathbf{m}\ddot{\mathbf{u}}$ acting at nodes by considering D'Alembert's principle to get the following variational form of the element

$$\begin{aligned}\delta\Pi_{\mathrm{HW}} &= \int_0^L \delta\mathbf{e}^{\mathrm{T}}\left(\hat{\mathbf{s}}(\mathbf{e}(x)) - \mathbf{b}(x,L)\,\mathbf{q} - \mathbf{s}_{\boldsymbol{p}}\left(x\right)\right) dx \\ &- \delta\mathbf{q}^{\mathrm{T}}\int_0^L \mathbf{b}^{\mathrm{T}}(x,L)\mathbf{e}(x)\; dx + \delta\mathbf{q}^{\mathrm{T}}\mathbf{a}_g\mathbf{u} \\ &+ \delta\mathbf{u}^{\mathrm{T}}\mathbf{a}_g{}^{\mathrm{T}}\mathbf{q} + \delta\mathbf{u}^{\mathrm{T}}\mathbf{m}\ddot{\mathbf{u}} - \delta\mathbf{u}^{\mathrm{T}}\mathbf{p}_{app} = 0\end{aligned} \tag{8}$$

Above equation can also be obtained by considering the general Hu-Washizu variational form with extension to dynamic case by Barr [8]. Equation (8) should hold for arbitrary $\delta\mathbf{u}$, $\delta\mathbf{q}$ and $\delta\mathbf{e}$, thus the following three equations should be satisfied in order for the Hu-Washizu-Barr variational to be zero.

$$\mathbf{m}\ddot{\mathbf{u}} + \mathbf{p} \equiv \mathbf{p}_{app}; \quad \text{where} \quad \mathbf{p} = \mathbf{a}_{\mathrm{g}}{}^{\mathrm{T}}\mathbf{q} \tag{9}$$

$$\mathbf{v} \equiv \int_0^L \mathbf{b}^{\mathrm{T}}(x,L)\,\mathbf{e}(x)\,dx; \quad \text{where} \quad \mathbf{v} = \mathbf{a}_{\mathrm{g}}\mathbf{u} \tag{10}$$

$$\hat{\mathbf{s}}(\mathbf{e}(x)) \equiv \mathbf{b}(x,L)\mathbf{q} + \mathbf{s}_{\boldsymbol{p}}\left(x\right) \tag{11}$$

Equation (9) is the equation of motion that holds for linear or nonlinear material response, and this equation can be collected for each element to get structure's equation of motion. A numerical time integration scheme can be employed to get a solution. Consequence of viscous damping can be simply achieved by adding $\mathbf{c}\dot{\mathbf{u}}$ to the left hand side of the equation, where **c** is the damping matrix. It is also possible to determine resisting forces **p** not only in terms of displacements **u** but also as a function of velocities $\dot{\mathbf{u}}$ through the use of a material model that considers time-dependent effects, such as visco-elastic or visco-plastic material models.

For linear elastic material response, section deformations can be calculated as $\mathbf{e}=\mathbf{k}_s^{-1}\hat{\mathbf{s}}$ to obtain the section deformations from section forces through the use of section stiffness matrix $\mathbf{k}_s$. Substitution of section deformations **e** to Equation (10) gives:

$$\mathbf{a}_{\mathrm{g}}\mathbf{u} = \mathbf{v} = \mathbf{f}\;\mathbf{q}; \qquad \text{where} \quad \mathbf{f} = \int_0^L \mathbf{b}^{\mathrm{T}}(x,L)\mathbf{f}_s\,(x)\,\mathbf{b}(x,L)\,dx \tag{12}$$

In above equation f is the flexibility matrix of the element in the basic system. $\mathbf{f}_s$ is the section flexibility matrix that can be calculated from the inversion of the section stiffness matrix $\mathbf{k}_s$. Further substitution of above equation for linear elastic response in Equation (9) results in

$$\mathbf{m}\ddot{\mathbf{u}} + \mathbf{k}\mathbf{u} = \mathbf{p}_{app}; \quad \text{where} \quad \mathbf{k} = \mathbf{a}^{\mathrm{T}}\mathbf{f}^{-1}\mathbf{a} \tag{13}$$

where **k** is the 6×6 element stiffness matrix in the complete system.

As a remark, Equations (10) and (11) are related to the element state determination, i.e. these equations can be solved independent of Equation (9), and then the solution can be condensed out into Equation (9) such that the equations of motion can be assembled for all elements. This process was demonstrated above for the linear elastic case. In general, state determination of the element requires an iterative solution in the case of nonlinear behavior, where Equations (9) to (11) are needed to be solved. This solution requires also the calculation of element flexibility matrix **f** under nonlinear response, where taking derivative of element deformations **v** in Equation (10) with respect to element forces **q** results into the same flexibility integration expression given in Equation (12), but this time the section stiffness will be nonlinear, as well.

2.4 Section Response

Section response can be obtained by the basic assumption that plane sections before deformation remain plane after deformation along the length of the beam by the use of following section compatibility matrix as given in Equation (2), where the section compatibility matrix now contains the shear correction factor κ_s as follows

$$\mathbf{a}_s = \mathbf{a}_s(y) = \begin{bmatrix} 1 & 0 & -y \\ 0 & \kappa_s & 0 \end{bmatrix} \tag{14}$$

Shear correction factor κ_s is taken as the inverse of the form factor suggested by Charney et al. [1] for I-sections:

$$\kappa_s = 1/\kappa; \quad \text{where} \quad \kappa = 0.85 + 2.32\frac{b_f t_f}{d\, t_w} \tag{15}$$

In above equation, b_f and t_f stand for the width and thickness of flange, respectively; d is the depth of the section and finally t_w is the thickness of the web.

The section forces are obtained by integration of the stresses that satisfy the material constitutive relations $\boldsymbol{\sigma} = \boldsymbol{\sigma}(\boldsymbol{\varepsilon})$ according to

$$\mathbf{s} = \int_A \mathbf{a}_s^{\mathrm{T}} \boldsymbol{\sigma}\, dA; \quad \text{where} \quad \boldsymbol{\sigma} = \begin{pmatrix} \sigma_{xx} \\ \sigma_{xy} \end{pmatrix} \tag{16}$$

The derivative of section forces from (16) with respect to the section deformations results in the section tangent stiffness matrix

$$\mathbf{k}_s = \frac{\partial \mathbf{s}}{\partial \mathbf{e}} = \int_A \mathbf{a}_s^{\mathrm{T}} \frac{\partial \boldsymbol{\sigma}(\boldsymbol{\varepsilon})}{\partial \mathbf{e}}\, dA = \int_A \mathbf{a}_s^{\mathrm{T}} \mathbf{k}_m \mathbf{a}_s\, dA \tag{17}$$

The material tangent modulus $\mathbf{k}_m$ is obtained from the stress-strain relation according to $\mathbf{k}_m = \partial\boldsymbol{\sigma}(\boldsymbol{\varepsilon})/\partial\boldsymbol{\varepsilon}$. Gauss-quadrature, the midpoint or the trapezoidal rule can be used for the numerical evaluation of the integrals in (16) and (17). While Gauss-quadrature gives better results for smooth strain distributions and stress-strain relations, the midpoint rule is preferable for strain distributions and stress-strain relations with discontinuous slope.

2.5 Force-Based Consistent Mass Matrix

The derivation of the consistent mass matrix requires the determination of the section mass matrix, where the mass is considered like a distributed load along the length of the beam in cantilever basic system for this derivation. The section mass matrix is easily computed by the following equation through the use of section compatibility matrix that is given in Equation (4) without the presence of shear correction:

$$\mathbf{m}_s(x) = \int_A \mathbf{a}_s^{\mathrm{T}} \rho(x,y)\, \mathbf{a}_s\, dA; \tag{18}$$

Mass matrix of the force-based element, which will be used in Equation (9), is written in 6×6 dimension by the method provided by [9], i.e. in the complete system with 3 degrees of freedom per node, as follows:

$$\mathbf{m} = \begin{bmatrix} \mathbf{m}_{00} & \mathbf{m}_{0L} \\ \mathbf{m}_{L0} & \mathbf{m}_{LL} \end{bmatrix} \tag{19}$$

where the components of element mass matrix are calculated from following sub-matrices

$$\begin{aligned}
\mathbf{m}_{LL} &= \mathbf{f}^{-1} \int_0^L \mathbf{b}^{\mathrm{T}}(x,L)\mathbf{k}_s^{-1}(x) \\
&\quad \cdot \left(\int_x^L \mathbf{b}^{\mathrm{T}}(x,\xi)\mathbf{m}_s(\xi)\mathbf{f}_p(\xi)\mathbf{f}^{-1} d\xi \right) dx \\
\mathbf{m}_{L0} &= \mathbf{f}^{-1} \int_0^L \mathbf{b}^{\mathrm{T}}(x,L)\mathbf{k}_s^{-1}(x) \\
&\quad \cdot \left(\int_x^L \mathbf{b}^{\mathrm{T}}(x,\xi)\mathbf{m}_s(\xi)\left(\mathbf{b}^{\mathrm{T}}(0,\xi) - \mathbf{f}_p(\xi)\mathbf{f}^{-1}\mathbf{b}^{\mathrm{T}}(0,L)\right) d\xi \right) dx \\
\mathbf{m}_{0L} &= \mathbf{m}_{L0} = -\mathbf{b}(0,L)\mathbf{m}_{LL} \\
&\quad + \int_0^L \mathbf{b}(0,x)\mathbf{m}_s(x)\mathbf{f}_p(x)\mathbf{f}^{-1} dx \\
\mathbf{m}_{00} &= -\mathbf{b}(0,L)\mathbf{m}_{L0} \\
&\quad + \int_0^L \mathbf{b}(0,x)\mathbf{m}_s(x)\left(\mathbf{b}^{\mathrm{T}}(0,x) - \mathbf{f}_p(x)\mathbf{f}^{-1}\mathbf{b}^{\mathrm{T}}(0,L)\right) dx
\end{aligned} \tag{20}$$

In above equations, element flexibility matrix $\mathbf{f}$ is obtained as given in Equation (12). The partial flexibility matrix $\mathbf{f}_p$ is calculated as follows:

$$\mathbf{f}_p(x) = \int_0^x \mathbf{b}^{\mathrm{T}}(\xi,x)\mathbf{k}_s^{-1}(x)\mathbf{b}(\xi,x)\, d\xi \tag{21}$$

3. Numerical Examples

In this paper, for the numerical example, the proposed model is verified with the 3D model created in ANSYS environment. For the verification of the proposed model, the section used in the study given in the literature [1], i.e. W36x135, W24x250 and W14x730 sections and in addition European sections HEB180, IPE270 and IPE750x147 are considered. For the verification of the proposed model different types of sections are utilized. ANSYS model could be accepted as control model of this study.

To have a fair comparison with the model data, the use of solid finite elements is a suitable modelling approach for simulation. For this purpose, the ANSYS Workbench Design Modeller is selected to perform 3-D finite element analyses after implementing bodies geometries and utilizing certain mesh conditions. In such a numerical model, modelling approximations would have great influence on the finite element analysis, like the considered element type, meshing elements number and size, boundary conditions and environment representations.

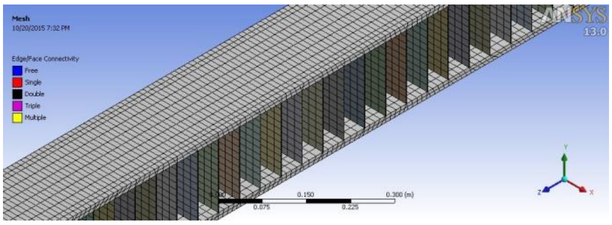

Figure 2: Representative ANSYS model sketch for one section

During the geometry implementation of the wide flange beams, 1 mm thick stiffeners, with very low mass density 1E-10 kg/m^3, are supplemented along the length of the elements to constraint the flanges and reduce their inordinate behaviour relatively; adopting such flange constraining approach converges to a more realistic behaviour of wide flange beams in structures. This way mode stabilization is achieved, where capturing clear axial, bending and shearing modes become possible for ANSYS simulations. The beam elements and the stiffeners in ANSYS model are both considered of solid type. After the geometry employment, quadrilateral mesh is generated using Solid187. This method uses linear elements to just obtain the correct results using the enhanced strain formulation. In the beams models, the number of mesh elements used changes from a test to another, but as a common value, the element size is set to 0.03 for all the beams. Yet, to set up conformal meshing among the body parts of the beams, the available Shared Topology tool is used to share faces and edges creating an analogous topology.

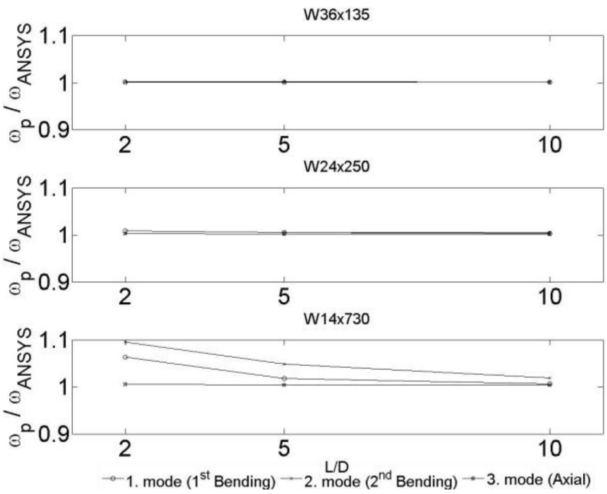

Figure 3: Natural frequency proposed over ANSYS result ratios for W-Section profiles

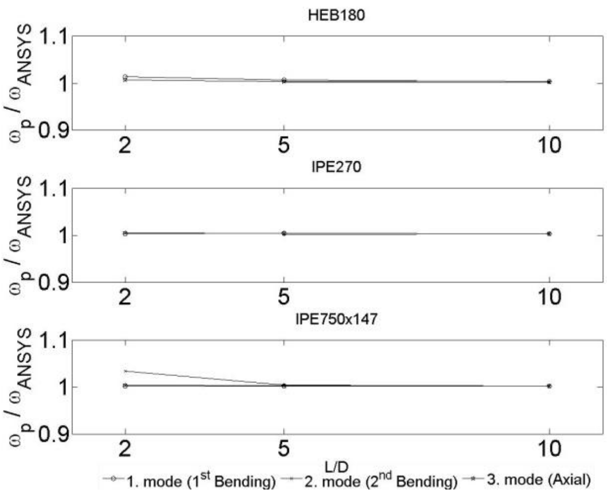

Figure 4: Natural frequency proposed over ANSYS result ratios for European section profiles

Figures (3) and (4) represent the ratio of the frequency results obtained by proposed model to ANSYS model. Here, in this study, the ANSYS FEM model is considered as control model, i.e. numerically converged exact solution for comparison. Thus, the ratio will represent the error between these control models and proposed model presented in this paper.

The results of the cantilever beams are represented separately for its first, second bending and axial modes of beams for different length over depth ratios. For the two groups of cross-sections, that are taken from study [1] and European sections, chubby and moderate sections represent significantly low errors, however, for the deep sections, approximately 10% error is obtained for smaller length over depth ratios. Yet, the effect of the shear can be better observed for the short beams, the effect on the deep sections should be further investigated.

4. Conclusions

The aim of this study is to gather and verify the modal behaviour of various I-sections under different length over depth ratios with the proposed beam finite element model.

The result of the study shows that the proposed model has satisfactory accuracy in capturing the real behaviour according to the verification carried on control models in ANSYS. The results prove that the error between the ANSYS model and proposed model is low and biased. However, the deep sections for both groups of sections, represents relatively larger errors, around 10%, which needs to be assessed in detail. Introducing stiffeners to the ANSYS model prevents the local modal deformations along the sections such as flange deformations independent from the bending deformations. Such deformations resulted into higher errors with the proposed model, since the proposed model can only show 2D frame deformation except from 3D local deformations like the results of the ANSYS FEM. For a fair comparison between a beam finite element model and 3D finite element models, it is necessary to define both top and bottom flanges and the web act together.

Acknowledgement

The authors thank for the support provided by Scientific and Technological Research Council of Turkey (TUBITAK) under Project No: 113M223.

References

[1]. Charney, F.A., Iyer, H., and Spears, P.W.,"Computation of major axis shear deformations in wide flange steel girders and columns", Journal of Constructional Steel Research, Vol. 61, pp. 1525–1558, 2005.

[2]. Gruttmann, F., Wagner, W., "Shear correction factors in Timoshenko's beam theory for arbitrary shaped cross-sections", Computatonal Mechanics, Vol. 27, pp. 199-207, 2001.

[3]. Chróscielewski, J., Pietraszkiewicz, W., Witkowski, W., "On shear correction factors in the non-linear theory of elastic shells", International Journal of Solids and Structures, Vol. 47, pp. 3537-3545, 2010.

[4]. Pai, P.F., Schulz, M. J., "Shear correction factors and an energy-consistent beamtheory",International Journal of Solids and Structures, Vol. 36, pp. 1523-1540, 1999.

[5]. ANSYS, Workbench 2.0 Framework, 2011.

[6]. Taylor, R.L., Filippou, F.C., Saritas, A., Auricchio, F.,"Mixed finite element method for beam and frame problems", Computational Mechanics, Vol. 31, No. 1-2, pp. 192-203, 2003.

[7]. Saritas, A., Filippou, F.C.,"Inelastic axial-flexure–shear coupling in a mixed formulation beam finite element", International Journal of Non-Linear Mechanics, Vol. 44, No. 8, pp. 913-922, 2009.

[8]. Barr, A.D.S.,"An Extension of the Hu-Washizu variational principle in linear elasticity for dynamic problems", Journal of Applied Mechanics, Vol. June, pp. 465, 1966.

[9]. Molins, C., Roca, P., Barbat, A.H.,"Flexibility-based linear dynamic analysis of complex structures with curved-"3D members", Earthquake Engineering & Structural Dynamics, Vol. 27, No. 7, pp. 731-747, 1998.

SECM/15/122

COMPARISON OF DESIGN METHODS OF WATER RETAINING STRUCTUERES USING THE PROVISONS OF INTERNATIONAL CODES

Ahamed M.A.A[1*] and Madushanka P.N.M[1]

[1]University of Peradeniya, Peradeniya, Srilanka
*E-Mail: aaqibest@yahoo.com, TP: +94773886192

Abstract: Durability and impermeability in a water-retaining structure are of prime importance if the structure is to fulfill its function over its design life. In addition, serviceability cracking tends to govern the design of water retaining structures. This research concentrates on load-induced cracking specifically that due to pure bending and to direct tension in water retaining structures. At present Sri-Lankan designers tend to use British standards in the design of water retaining structures. But today the countries in the world have adopted different codes with the belief that the code adopted will best fulfill the requirements in designing water retaining structures for their particular exposure. Even with the proper design using that selected code, a question arises about the acceptability of the design with regard to other international codes. Thus, Comparison of these international codes is of paramount importance. ACI 350M, AS 3735, BS 8007 and EN 1992-3 were the codes that were selected to do the comparison. Identifying the major contributors for cracking as flexure and direct tension load case according to the given procedure for each code to control cracking spreadsheets were developed. During the project several parameters were varied and by analyzing the obtained results, an effort was taken to evaluate the design approaches given in each code to control cracking.

Keywords: comparison of design methods, water retaining structures, control cracking, international codes.

1. Introduction

Reinforced concrete construction is commonly used, for a wide variety of liquid containing and liquid excluding structures. Failure to achieve an adequate standard of water tightness may result in leakages which could violate the main purpose of the structure. Today different countries use their own standard with the belief it is the most suitable norm for their environmental conditions. At present a need has arisen to compare the different types of design methods used in these international codes.

Crack controlling is most important to the serviceability of the structure to perform its functional aspect. The objective of the current study is to analyse the design methods used in different standards to control cracking in water retaining structures.

2. Literature review

The literature review was focused mainly on methods of Crack controlling. Though there are numerous international codes to design water retaining structures there may be occasions where the specified crack width limit from those codes may not satisfy the leakage requirement according to the investigation done my L.G Mrazek (2001). Here the author presents a review of crack width limitations for structures that are subjected to leakage and compares these limitations with field measurements of cracks in environmental engineering concrete structures as well as concrete parking structures. Finally advises designers not to use ACI 318-99 for design of water retaining structures as leakages noticed from cracks in field measurements were below the crack width limit specified. However, In most of the literature that were found related to crack controlling, research in comparisons between codes and standards were a common gap that was found. So in order to compare between codes the discussion was categorized into eight categories. They were, Design working life, Approach for the design, Specified crack with limits, Permitted cement types, maximum water cement ratios, methods adopted to control cracking, water tightness classification, partial safety factors and finally exposure classifications. Though some aspects (e.g. design working life) were more or less the same in each code, it was understood that some specifications were defined uniquely for a particular code. (E.g. water tightness classification – EN 1991-1-3). Furthermore the method of crack controlling given in each code is very much different to each other. The ACI 350R-2006, EN 1991-1-3 2006 codes give more than one method of crack controlling whereas BS 8007 1985 and AS 3735 2001 gives only one particular method of crack controlling. After studying these codes it was clear that each code has its own approach and method of crack controlling in water retaining structures.

3. Scope

3.1 Structural Configuration

The conference proceedings will be published in standard book (170mm x245 mm) size with two column layout for text. Diagrams and tables should be in portrait orientation with either one or two column width.

Here, basically two types of structures were considered

a) Wall of a circular tank – diameter of the tank is 20 m
b) Base panel of a rectangular tank- dimension of the panel is 8 m by 4 m

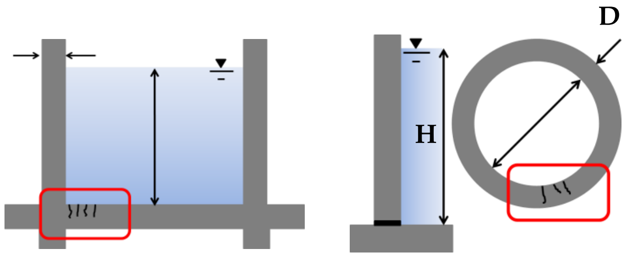

Figure 1: Structural Configuration

3.2 Fixed Design Parameters

$f_{ck,cylinder}$	= 30 MPa
$f_{ck,cube}$	= 37 MPa
$f_{ct,eff}$	= 2.9MPa
f_y	= 500 MPa
E_s	= 200 GPa
Υ_w	= 1000kg/m3
Cover	= 50 mm.

3.3 Physical Parameters

Height of the water column (H):
Water depth was varied from one to five meters for flexural load case and two to twelve meters for direct tension case for the crack width calculation.

Section thickness (h):
Section thicknesses 250 mm, 300 mm, 350 mm, 400 mm, 450 mm, and 500 mm were considered.

Bar diameter (φ):
Diameters of 16 mm, 20 mm and 25 mm were selected.

Spacing (s):
Spacing for bars were varied for 75 mm, 100 mm, 150 mm, 200 mm, and 250 mm.

3.4 International codes selected

- BS 8007: 1985 with BS 8110-1
- EN 1992-1-3 2006 with part1:2004
- AS 3735:2001 with AS 3600:2001
- ACI 350R:2006 with ACI 318:2011

4. Methodology

Under each code a procedure for control of cracking was formulated and using spread sheets varying the parameters within the scope results were derived.

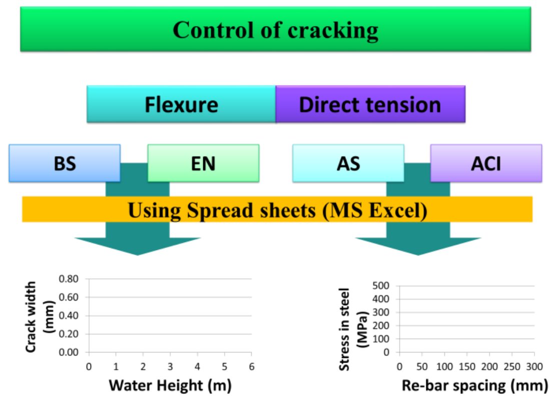

Figure 2: Methodology

5. Results

Results of the deterministic analysis of BS8007, EN1992-3, AS3735 and ACI350M serviceability limit state crack controlling for flexural and tensile load-induced cracking in WRS were obtained in this section. Microsoft excel was used as the tool during this process to calculate crack widths, crack width limits and limiting stresses in reinforcements.

Results were obtained by varying the parameters within the scope for the given structural configuration as discussed in section 3. In this field of study for the EN1991-1-3 and BS 8007 the crack width vs. water height was plotted and compared with the specified crack width limits given in the code and for the AS 3735 and ACI 3600 the stress induced in the reinforcement steel vs. spacing between bars were graphically presented and compared with the specified limiting stress values.
As results, 345 figures were obtained and more than 500 combinations or situations could be checked. By that analysis for a given case the acceptability and the compatibility of the four codes could be decided.

5. Conclusions

- Although EN also covers a method to control cracking based on spacing and limiting stress BS and EN mainly control cracking by calculating the crack widths and controlling those crack widths within certain limit.
- ACI and AS approaches for control cracking are by limiting the stresses in tension reinforcements and also by controlling spacing within those reinforcements.
- EN1992-3 specifies a range of crack width limits from 0,2 mm to 0,05 mm for through-cracks, depending on H/h, whereas BS 8007 specifically limits a value for the crack width. (0.2mm or 0.1mm) for very severe condition and when Aesthetic appearance is critical.
- Euro code uniquely introduces water tightness classification which describes the amount of leakage allowed for each class.
- Because of the decreasing limiting crack width in EN 1992-3, it results in a substantial increase in reinforcement and increase in section geometry for both flexural and tension cracking.
- For flexural load case, when the sectional thicknesses are greater than 300 mm, crack width values from EN will be more conservative than BS results. When the section thickness is less than 300 mm BS will give more conservative values.
- Only the re-bar diameter is concerned to control stresses in re-bars about in AS, ACI give more conservative limiting stress values, as the bar diameter and spacing increases. Also unlike AS, ACI 350 applies different stress limits for different exposure conditions

Acknowledgement

First and foremost our very special thanks goes to Mr. H. Abeyruwan who has been supporting us throughout the project. Next, our heartily deepest gratitude goes to the project panel members, Dr. H.D. Yapa and Dr. (Mrs) C.K. Pathirana. Finally would like to thank the non academic staff members and other parties for supporting us during the research.

References

[1]. Exposure classes for designing durable concrete by Vijay R. Kulkarni, The Indian Concrete Journal, pp. 23-43, 2009 march.
[2]. What is the crack width in concrete structures to prevent leakage? By L.G Mrazek, ACI special publication pp.237248, Design and construction practices to mitigate cracking, 2001.
[3]. British standards 1997,BS 8110-Part 1-code of practice for design and constructions BS 8007-Design for concrete structures for retaining aqueous liquids
[4]. Euro standards (2006), EN 1992-1-1-Design for concrete structures, EN 1992-3Liquid retaining and containment structures.
[5]. Australian standards AS 3735(2001) concrete structures for retaining liquids, AS 3600 (2001) – concrete structures.
[6]. American standards ACI 350R (2006) - code requirements for environmental engineering concrete structures, ACI 318 (2014) - Building code requirements for structural concrete

SECM/15/123

An Experimental Study on Pre-tensioned Concrete Members

A. Donmez[1*], S. Ataoglu[1] and Z. Abdulaliyev[1]

[1] Istanbul Technical University, Faculty of Civil Engineering, Civil Engineering Department, Maslak, 34469, Istanbul, Turkey
*E-Mail: donmezab @ itu.edu.tr, TP: +905363508881

Abstract: Prestressed concrete elements are highly being used in the construction industry. For these kind of precast members, exposure to the loading starts at the fabrication processes. There might be high level of stress fields inside the element because of the prestressing. Exact values of these stresses are being assumed according to the linear homogenous design criteria. However, modeling a pre-tensioned prestressed concrete member via photoelastic experimental procedure could lead to make exact stress analysis in a pointwise manner. The analogy between the prestressing phenomena with photothermoelasticity led to make a pretensioned concrete model with using the "frozen-stress" method of photoelasticity. Two sorts of three-dimensional photoelastic models are prepared and analyzed with using the experimental techniques of three-dimensional photoelasticity and aimed to deal with the investigation of the pre-stress distribution after the fabrication process of the pre-tensioned reinforced concrete members. With considering the technical literature, insufficient information requires to make an investigation of the stress distribution at the vicinity of the free edges and bonding area of the reinforcing material of the pre-stressed structural members. Finally, obtained results show that some regions in a prestressed member have to endure high level of compressive and shear forces immediately after the release of prestress. This study mainly deals with the determination of the critical regions in a prestressed member and taking some precautions in order to keep the safe design margins.

Keywords: Pretensioned concrete, photothermoelasticity, photoelastic modelling, anchorage zone.

1. Introduction

Limited tensile strength of reinforced concrete made the large-span system constructions impossible to undertake in the past. Highly utilized compressive strength of concrete is facilitated by prestressing phenomena. The concept has experienced essential developments with high technology in response to the architectural needs [1, 2]. Partially PC, external PC, highly eccentric prestressing and extradosed prestressing are among the viable innovative advancements [3]. The prestressed concrete as a major structural material has still some problems despite to contributions to technological improvement of its constituent materials. Steel corrosion, concrete creep, prestress loss and environmental effects deteriorate the structural durability in decades. Particularly, prestress loss, bond slips and transfer length assumptions are being made for pretensioned concrete materials in order to ensure the structural safety [4, 5]. Regarding the bond mechanism of pretensioned concrete members, a much more sophisticated analysis is required to handle with this kind of self-equilibrated internal stress state at the fabrication process. A photoelastic experimental procedure is able to tackle with a pointwise stress analysis.

A pretensioned concrete material is a type of composite member consists of concrete and steel tendons. Photoelastic modeling of a composite structure is possible with using the "frozen-stress" method of 3-D photoelasticity. If a birefringent material is loaded at its critical temperature, T_c, and then cooled down to room temperature in a slow rate, internal stresses are locked after this freezing cycle. This type of behaviour allows to make the photoelastic analysis of 3-D models with using slice method [6, 7].

2. Experimental Procedure

In this study, two types of three-dimensional photoelastic models (3DModel1 and 3DModel2) are implemented in addition to a two-dimensional photoelastic stress analysis (2-DModel) made before [8]. Let the composite structure made in n dissimilar materials. For a proper photoelastic modelling the Eq. [1] must hold at the freezing temperature (T_f), between the materials used in prototype and model.

$$\frac{E_{pi}}{E_{p(i+1)}} = \frac{E_{mi}}{E_{m(i+1)}}; \quad i = 1,2, \ldots n \qquad (1)$$

where E denotes the elastic moduli of the ith material, p and m the prototype and model. Models presented herein consist of 2 types of birefringent material (araldite1 and araldite2) and an opaque plastic material (nylon6). Young moduli variation of the used materials according to temperature change are shown in Fig. 1.

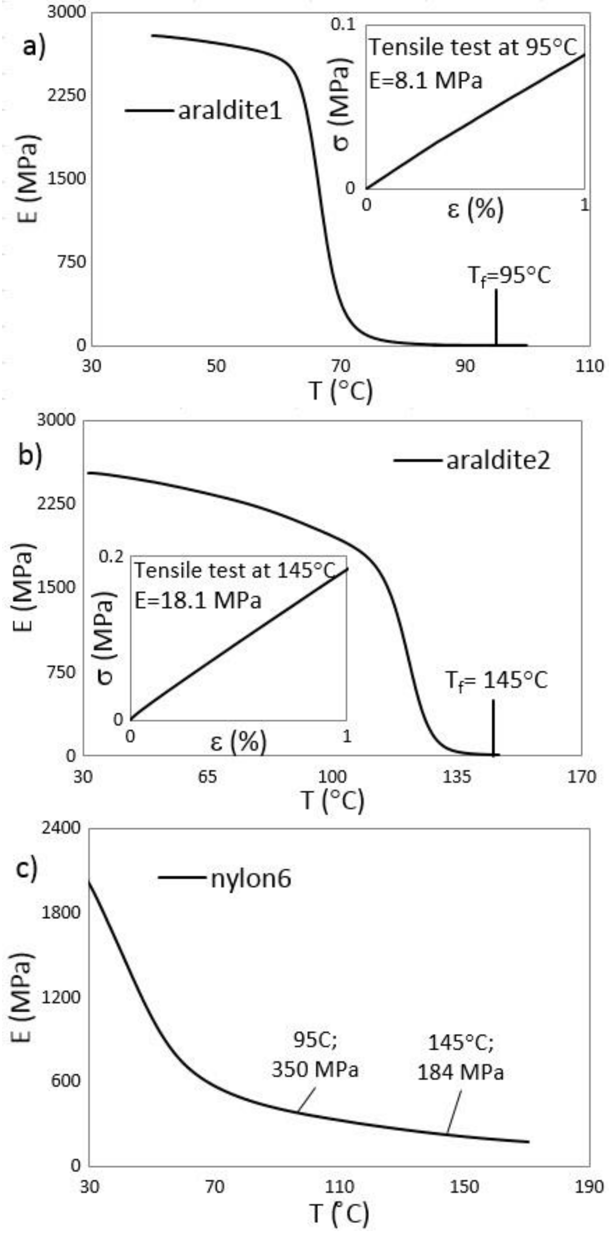

Figure 1: Temperature-Young Modulus curves for a) araldite1, b) araldite2, and c) nylon6 with tensile test results at freezing temperatures

Based on the test results, implemented by DMA (Dynamical Mechanical Analyzer), nylon6 and araldite2 compliance the aforementioned modular ratio for the prototype which consist of concrete and steel materials. These two materials form the 3DModel1. For the sake of comparison another 3-D Model (3DModel2) is made by araldite1 and nylon6 with having a modular ratio of E_n/E_a=43.

Calibration is needed to make the photoelastic analysis. Optical sensitivities of both araldite specimens are determined with photoelastic disk specimens for each material (Fig.2).

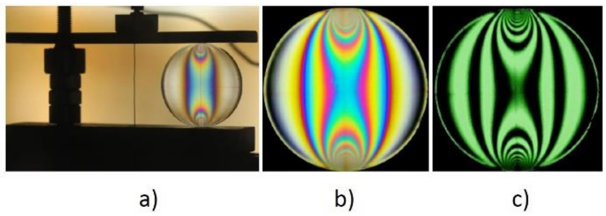

Figure 2: a) Loading frame in digitally controlled oven, b) fringe pattern of the disks in white light, c) monochromatic light

With using the polarizer microscope the centroid fringe numbers are obtained. Following relationship is used to assess the optical sensitivity constant which holds for the center point of the disk.

$$\sigma_0^{1.0} = \frac{4P}{\pi \mu \mathrm{R}} \qquad (1)$$

where $\sigma_0^{1.0}$ is the optical sensitivity constant, P the applied load, μ fringe number and R radius. Using the Eq. [1] optical constants of araldite1 and araldite2 is found as 0.25 and 0.22 respectively.

The preparation of the models consists of the following steps.

2.1 Prestressing

Applying the prestress forces to the model is conducted via "freezing cycle", which leads to lock the stresses in the photoelastic materials (Fig. 3a). Frozen-stress work is made with regarding the critical temperatures of the optical materials which are 95°C and 145°C for araldite1 and araldite2, respectively. There is an analogy between the photothermoelasticity and stress distribution of the prestresses pretensioned concrete members. In line with this analogy the prestress forces are applied on the birefringent materials via compressive loads which are representing the concrete part of the prototype. The stability and compressive yield strength controls are made with analytical and experimental work to determine the weights. It is supposed that the stress level of a prestressed member immediate after the fabrication process are below the strength limits of used materials.

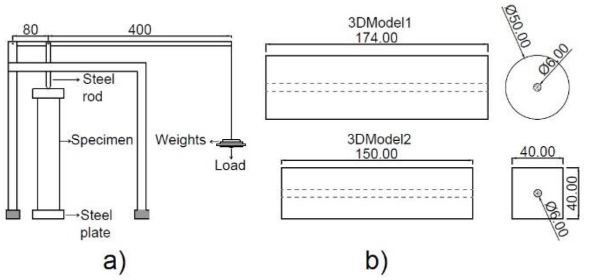

Figure 3: a) Loading frame, b) 3-D Models

Therefore the compressive stresses frozen in the araldite specimens are 0.20 MPa and 0.15 MPa for the 3DModel1 and 3DModel2 respectively (Fig. 3b).

2.2 Drilling

In regard with the defined geometrical similarity ratio, ¼, araldite specimens are drilled with 6mm diameter drilling bit. Only a single hole at the center of the cross sections, created for each 3-D models.

2.3 Placing the bars

Nylon6 rods, with having a diameter of 6mm, is sited inside the holes with using a claw mechanism and prepared epoxy glue (Fig. 4 a-c).

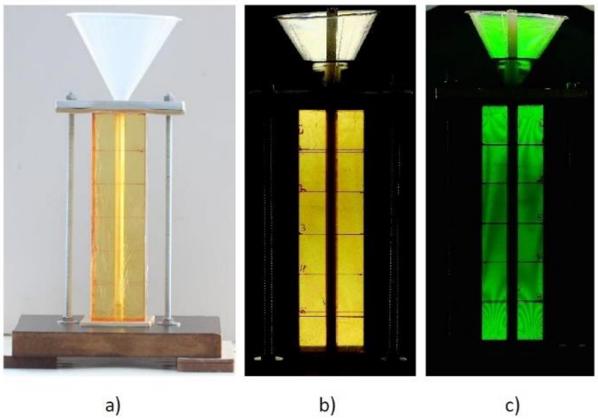

Figure 4: a) Placing and gluing the inclusion, and polariscopic photographs of 3DModel2 on b) white, c) monochromatic light

2.4 Releasing

After the completion of the models, another freezing cycle is implemented in order to release the prestresses which are already locked in the araldite part of the specimens. To fulfil the freezing operation, models are heated with 3°C/h rate to its freezing temperature, halt at this temperature for 3 hours and cooled down to the room temperature consecutively at the same rate with heating up. The generated interference fringe pattern of the models after the release of prestresses is shown in Fig. 5 a, b.

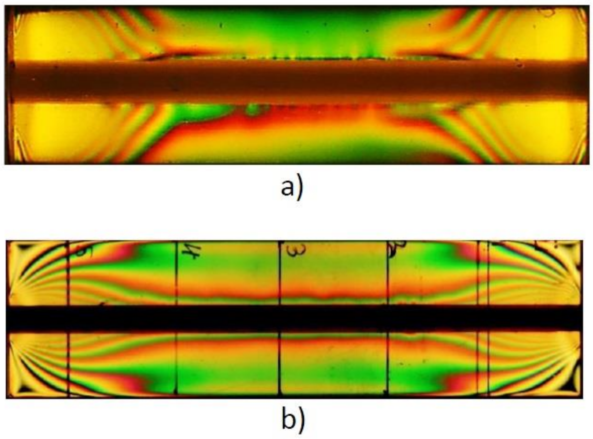

Figure 5: Fringe pattern of the a) 3DModel1 and b) 3DModel2 after the release

Frozen stress phenomena leads to make a comprehensive photoelastic analysis of 3-D models with using slicing method of photoelasticity. Regions of interest are sliced from the 3-D models and defined points are measured with Leica polarizing microscope.

3. Experimental Analysis

Stress results of the models are obtained with the aforementioned photoelastic work. Stress values of the model must be transformed to prototype correspondent. Thus following relationship holds for the model-prototype relationship.

$$\sigma_p = \frac{1 - \vartheta_p \varepsilon_{0p} E_p}{1 - \vartheta_m \varepsilon_{0m} E_m} \sigma_m \tag{2}$$

where ϑ, ε_{0p}, E and σ represent for the Poisson's ratio, initial pre-strain, Young modulus and stress respectively. Suffixes of p and m refer to prototype and model. With using Eq. [2] conversion factors, $n=\sigma_p/\sigma_m$, are found and shown in Table 1.

Table 1: Model-prototype conversion parameters

Model	ε_{0m}	ε_{0p}	n
2DModel	0.014	0.0015	162
3DModel1	0.011	0.0015	205
3DModel2	0.019	0.0015	266

3.1 2D Model

The detailed information about the 2DModel can be found in [8, 9], which is a model of prestressed concrete slabs. It consists of araldite2 for concrete and nylon6 for prestressing tendon. Experimental analysis results along the interface is shown in Fig.4.

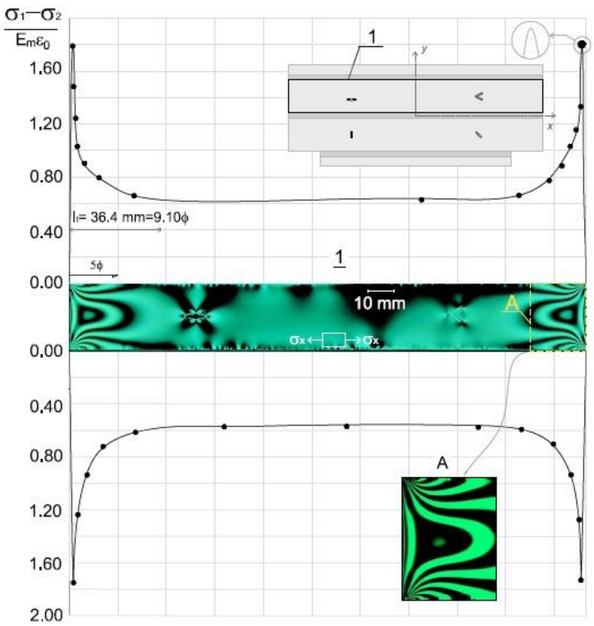

Figure 4: Normalized stress distribution along the interface of 2DModel, (ϕ= 4 mm, l_t: transfer length, E_m: Young modulus araldite2, ε_0: initial value of frozen strains on the araldite part of the model)

In the Fig. 4, σ_1 and σ_2 define the principal stresses at the certain points on the concrete steel interface. The normalization is made by initial prestress value (frozen-prestress), which equals to $E_m\varepsilon_0$ (0.28 MPa for 2-DModel). The difference of the principal stress values is called as Tresca stresses. Half of the Tresca stress values equal to the maximum shear stress. It can be deduced from the figure shown above that maximum shear stresses are 0.9~1 times of initial prestress. Considering the converted stress, this value is much higher than the shear strength limit, assuming that the shear strength is equal to $\sqrt{f_c}$, in which f_c is the compressive strength of concrete. And the transfer length is measured about 9.1 times of used tendon diameter.

3.2 3DModel1

The concrete part of 3DModel1 is represented by araldite2. Modular ratio of the materials comply with the prototype. The model has *50 mm* diameter cross section with *6 mm* diameter nylon6 rod which represents the tendon. Sample1 from the 3DModel1 is cut during the slicing operation (Fig. 5)

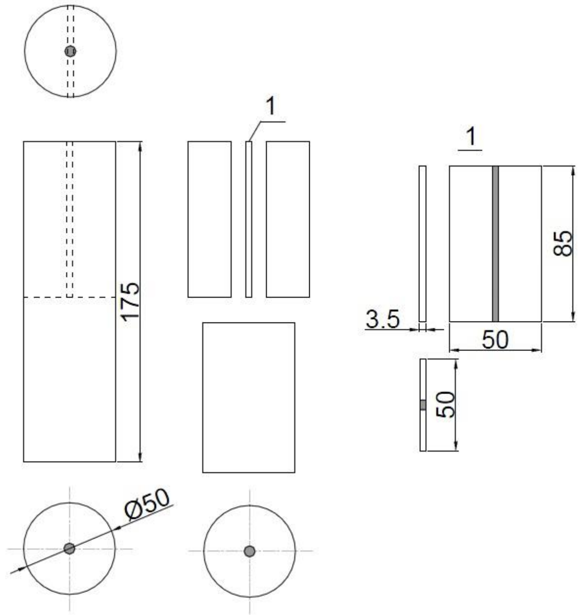

Figure 5: Sliced sample1 from 3DModel1

Sample1 represents the anchorage zone of the model. Stress concentrations are located at the free ends of the interface region. The graphical representation of the measured stress values on sample1 is shown in Fig. 6.

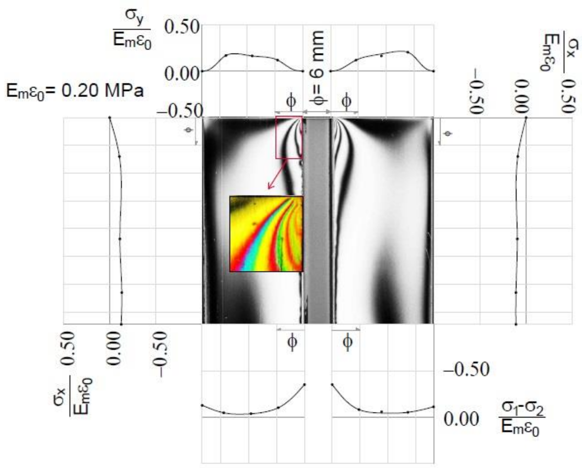

Figure 5: Experimental stress analysis of 3DModel1 at its edges (σ_1, σ_2: principal stresses)

Principal stress differences at the edges of 3DModel1 is shown in Fig. 6. The stress values called as Tresca stresses normalized with the initial prestress which is *0.20 MPa* for this case. As a result of the investigation of the stress field yielded at the edges of the prestressed member, attention is called at the edges on anchorage zone. The top end of the member undergoes high tensile stresses on concrete part (more than *8 MPa*). This value is much higher than the assumed tensile strength of a regular concrete. High concentration of stress in the anchorage zone threatens the structural safety. Maximum shear stress in this field could be as higher as more than *41 MPa*. Interface regions would bear overloaded transmission forces at the transfer length. This problem may come out as tendon slips after the fabrication process.

3.3 3D Model2

3DModel2 consists of araldite1 and nylon6 materials. The concrete part is simulated by araldite1 and nylon6 for steel. Modular ratio is about 40. The model has square cross-section with a 6 mm tendon diameter.

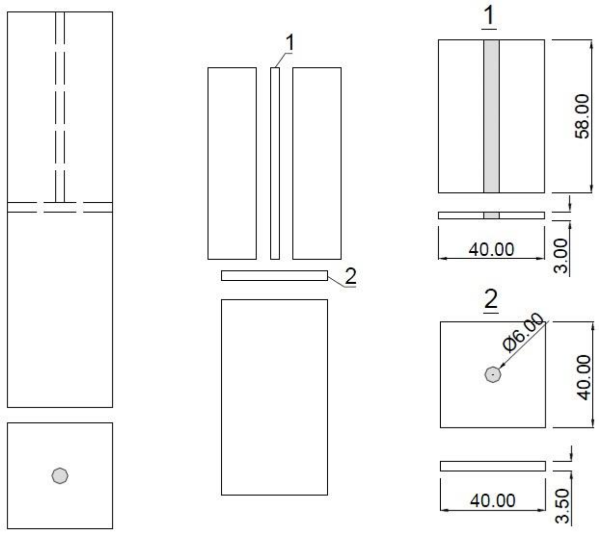

Figure 5: Cut samples of 3DModel2 via slice method

The geometry and dimensions of sample 1 and sample2 of 3DModel2 are shown in Fig. 5. The anchorage zone analysis is made on sample 1. Concentrated fringe pattern at the free ends of the interface can be seen on Fig. 6. Sample 2 is cut at the transverse plane to the applied prestress load (Fig. 7). The slice operations are made with using milling machine. Precautions are taken in order to provide the sample against residual stresses which could be generated at the cutting operations.

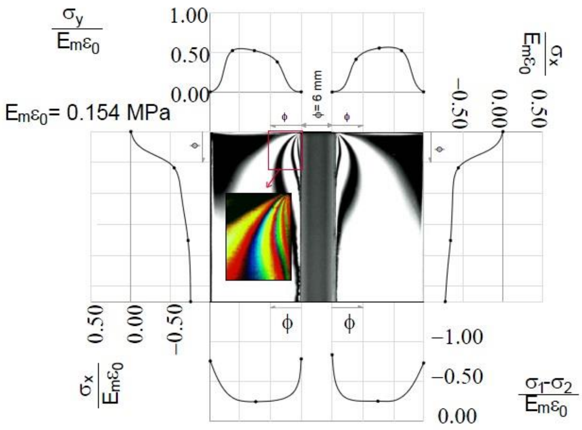

Figure 6: Cut sample 1 from 3DModel2 via slice method

It can be seen from Fig. 6 that tensile forces at the anchorage end of the member can reach up to half of the initial prestress force. According to Eq. [2] and Table 1, tensile stress at this part is about 20 MPa which certainly can cause the cracking. The tensile stress value at these regions is 8 MPa for 3DModel1 which has the proper modular ratio with the prototype. The maximum shear stress at the anchorage zone is approximately 60 MPa. Which is 41 MPa for the previous 3-D model. These values are much higher than the elastic limits if one consider a regular normal weight concrete.

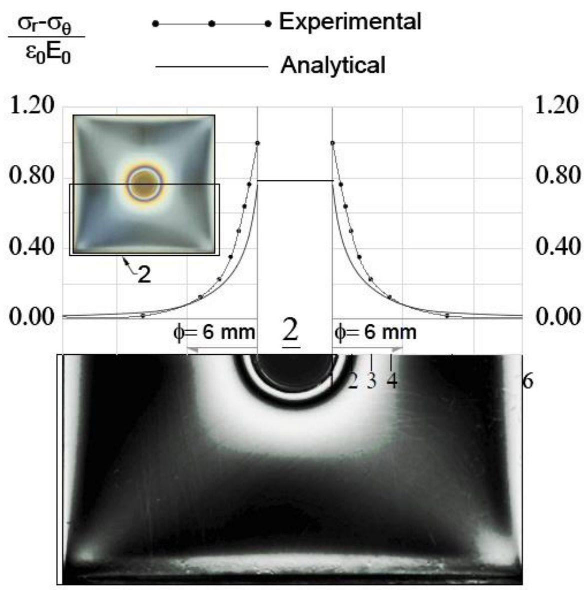

Figure 6: Cut sample 1 from 3DModel2 via slice method

Fig 6 represents for the transverse cut sample 2 of 3DModel2. It can be deduced from the analysis of sample 2 that with releasing the prestress forces contact interface bears considerably high radial stress.

4. Conclusions

Experimental simulations of prestressed concrete members are made by using the thermoelastic analogy. The mechanism of stress transmissions of different material joints in a uniform heat flow led to use the frozen-stress method of photothermoelasticity for the simulations of prestressed elements. The photoelastic analysis with help of the conversion to prototype techniques yield in significant results about the stress levels of prestressed materials, immediate after the fabrication process. The most notable conclusions are derived at the anchorage zone and at the free ends of the member. The bond regions between concrete and prestressed tendons acquires considerably high shear and radial stress values which may result in reinforcement slips with prestress loss.

Acknowledgement

The authors thank to Can Kurtulan due to his efforts on the experimental work and the Management of Scientific Research Projects of Istanbul Technical University.

References

[1]. Harajli, M. H., "Strengthening of Concrete Beams by External Prestressing", Precast/Prestressed Concrete Institute, Journal, Vol. 38, No. 6, pp.76-88, 1993.

[2]. Mathivat, J., (1988) "Recent Development in Prestressed Concrete Bridges", FIP Note, Vol. 38, No. 6, February, pp.15-21, 1988.

[3]. Mutsuyoshi, H., and Hai, N. D., "Recent Technology of Prestressed Concrete Bridges in Japan", IABSE-JSCE Joint Conference on Advances in Bridge Engineering-II, August 8-10, Dhaka, Bangladesh, 2010.

[4]. Han, S. J., Lee, D. H., Cho, S., Ka, S., and Kim, K. S., "Estimation of Transfer Lengths in Precast Pretensioned Concrete Members Based on a Modified Thick-Walled Cylinder Model", Structural Concrete, 2015 doi: 10.1002/suco.201500049.

[5]. Bymaster, J. C., Dang, C. N., Floyd, R. W., and Hale, W. M., "Prestress Losses in Pretensioned Concrete Beams Cast With Lightweight Self-consolidating Concrete", Structures, Vol. 2, pp.50-57, 2015.

[6]. Frocht, M. M., Photoelasticity, Volume 1, Pergamon, Oxford, 1948.

[7]. Frocht, M. M., Photoelasticity, Volume 2, Pergamon, Oxford, 1948.

[8]. Abdulaliyev, Z., Donmez, A., and Ataoglu, S., "Photoelastic Stress Analysis of pre-tensioned concrete elements (in turkish)" El-Cezeri Journal of Science and Engineering, Vol. 2, No. 3, pp.60-66, 2015.

SECM/15/140

BOND STRENGTH BEHAVIOR OF HEADED REINFORCEMENT BAR WITH VARYING EMBEDMENT LENGTH

S. Gond[1] and Prof. S. M. Kulkarni[1*]

[1]Parul Institute of Engineering and Technology, Limda, Vadodara, Gujarat, India
*E-Mail:Suhasini.kulkarni@paruluniversity.ac.in

Abstract: Headed reinforcement is a relatively new product and has not been used in many applications. Headed reinforcing bars have been extensively used in the construction of offshore oil platforms where hooked bars have traditionally been used to anchor longitudinal reinforcement or bars bent for ties and transverse reinforcement. Hooks and bent-bar ties create a large amount of congestion in the reinforcing cage which leads to difficulties during construction. Using headed reinforcement removes the tail extensions of hooks and allows fewer larger bars to be used, greatly reducing the congestion of the reinforcing cage. It has been found that the use of headed reinforcement can greatly decrease the time needed to erect the reinforcement resulting in large cost savings. Headed reinforcement has also been used in a few projects for strengthening and repairing footings of highway structures.

A total 81 Pullout test were performed to the study of Bond behavior of Headed reinforcement bar in concrete with different Embedment length with various diameters of bars, various grade of concrete and various sizes of cubes.

In this research project, it is proposed to execute experimental work by using headed reinforcement bars. The effect of different parameters like embedment length, head shapes and concrete grades, threaded headed reinforcement bars can be study. The results will be used to develop design recommendations for the application of headed reinforcement bars.

Keywords: headed reinforcement; pullout; embedment length; diameter of bars.

1. Introduction

Headed bars are created by the attachment of a plate or nut to the end of a reinforcing bar to provide a large bearing area that can help anchor the tensile force in the bar. Figure 1.2 shows an example of a headed bar. The tensile force in the bar can be anchored by a combination of bearing on the ribs and on the head. This chapter discusses the current state-of-the-art of headed bar technology.

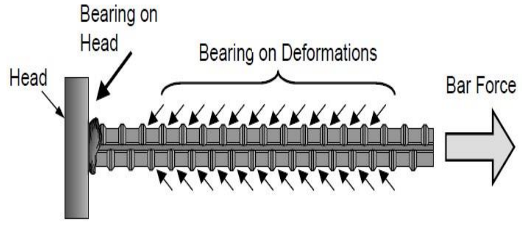

Figure 1.1: Anchorage of a headed bar

$$\text{Relative Head Area} = \frac{\text{The net head area}}{\text{The nominal bar area defined by ASTM A615}}$$

A_{nh} = the net head area

A_{gh} = the gross head area

A_b = the nominal bar area defined by ASTM A615

1.1: ASTM Code: Designation A970/A970M − 13A

Standard Specification for Headed Steel Bars for Concrete Reinforcement. Specification covers deformed steel reinforcing bars in cut lengths, with a head attached to one or both ends for concrete reinforcement. Heads are forge-formed machined from bar stock, or cut from plate. Attachment can be accomplished through

Welding Integrally hot forging of a head from the reinforcing bar end Internal threads in the head mating to threads on the bar end Separate threaded nut to secure the head to the bar. Head dimensions shall define the head geometry including thickness, diameter

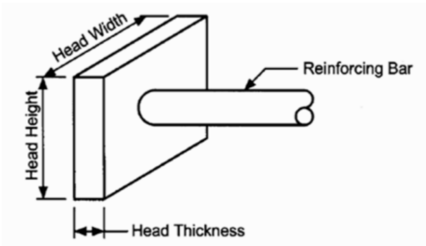

Figure 1.2: Headed Reinforcing Bar

1.2 Commentary Section 12.6 IN ACI 318 States

The limitation on obstructions and interruptions of the deformations is included in Code Section 3.5.9 because there are a wide variety of methods to attach heads to bars, some of which involve obstructions or interruptions of the deformations that extend more than $2d_b$ from the bearing face of the head. These systems were not evaluated in the tests used to formulate the provisions in Code Section 12.6.2, which were limited to systems that meet the criteria in Code Section 3.5.9." Some of the types of headed bars added to this specification after the 2009 version may have obstructions or interruptions in deformations exceeding the requirements of ACI 318 and thus not comply with the design requirements. Those types of headed bars explicitly satisfying the geometrical requirements in A970/A970M – 09 and Annex A1, comply with the minimum requirements provided in ACI 318, Sections 3.5.9 and 12.6.

2. Preparation for Experiment

- Heads and Bars 20 mm , 16 mm , and 12 mm
- For 20 Mm Φ Bars
  Cube size (300X300X300)
  Headed bar Size
  1. Square (50X50X10) mm,
  2. Rect.(105 X30X10) mm,
  3. Circular 57 mm dia.

  or height and width of the head.
- For 16 MM Φ Bars
  Cube size   (250X250X250)
  Headed bar size
  1. Square (40X40X8)mm,
  2. Rect.   (67X30X8) mm,
  3. Circular 46 mm dia.
- For 12 MM Φ Bars
  Cube size (200X200X200)
  Headed bar size
  1. Square (30X30X6)mm.
  2. Rect. (38X30X6) mm.
  3. Circular 34 mm Dia
- No's of Specimens:

Grade of Concrete	Shape of Heads			Total No's of Specimens
	Rec.	Square	Circular	
M20	9	9	9	81
M30	9	9	9	
M40	9	9	9	

Diameter of Bar Db mm	Area of Bar (A_b) mm^2	Embedment Depth/Length (E_d) mm				Thickness of Head (Th)mm		A_{nh} mm^2
12	113.076	$10D_b$	120	160	200	$0.5D_b$	6	$8A_b$
16	201.024	$12D_b$	144	192	240		8	
20	314.1	$14D_b$	168	224	280		10	

Square	Size	Rectangular	Size	Circular	D_h mm	Formwork size (A)
904.608	30x30	904.608	38x30	1152	34	200x200x200
1608.192	40x40	1608.192	67x30	1536	46	250x250x250
2512.8	50x50	2512.8	105x30	1920	57	300x300x300

3. Work Done

- Heads and Bars 12 mm, 16 mm, 20 mm
- Headed bar length is 1 m for all dia. of bars
- Specimen’s formworks
- Specimen’s castings

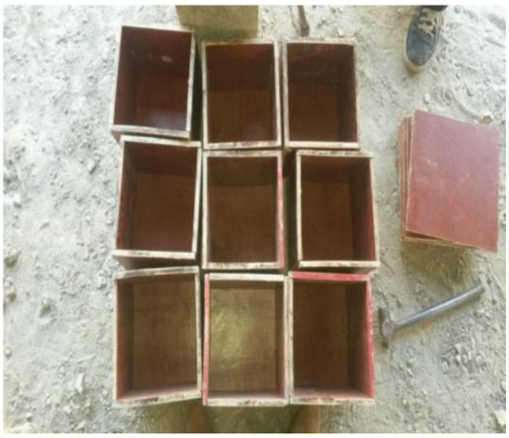

5.Embedment lengths of headed bars

Sr. No	Dia. Of Bar	Grade of Concrete	Embedment length (mm)	Shape of Heads		
				Rectangular	Square	Circular
1	20	M20	10 x20 = 200	2R1	2S1	2C1
2	20	M20	12 x 20 = 240	2R2	2S2	2C2
3	20	M20	14 x 20 = 280	2R3	2S3	2C3
4	20	M30	10 x20 = 200	3R1	3S1	3C1
5	20	M30	12 x 20 = 240	3R2	3S2	3C2
6	20	M30	14 x 20 = 280	3R3	3S3	3C3
7	20	M40	10 x20 = 200	4R1	4S1	4C1
8	20	M40	12 x 20 = 240	4R2	4S2	4C2
9	20	M40	14 x 20 = 280	4R3	4S3	4C3

Sr. No	Dia. Of Bar	Grade of Concrete	Embedment length (mm)	Shape of Heads		
				Rectangular	Square	Circular
1	16	M20	10 x16 = 160	2R1	2S1	2C1
2	16	M20	12 x 16 = 192	2R2	2S2	2C2
3	16	M20	14 x 16 = 224	2R3	2S3	2C3
4	16	M30	10 x16 = 160	3R1	3S1	3C1
5	16	M30	12 x 16 = 192	3R2	3S2	3C2
6	16	M30	14 x 16 = 224	3R3	3S3	3C3
7	16	M40	10 x16 = 160	4R1	4S1	4C1
8	16	M40	12 x 16 = 192	4R2	4S2	4C2
9	16	M40	14 x 16 = 224	4R3	4S3	4C3

Sr. No	Dia. Of Bar	Grade of Concrete	Embedment length (mm)	Shape of Heads		
				Rectangular	Square	Circular
1	12	M20	10 x12 = 120	2R1	2S1	2C1
2	12	M20	12 x 12 = 144	2R2	2S2	2C2
3	12	M20	14 x 12 = 168	2R3	2S3	2C3
4	12	M30	10 x12 = 120	3R1	3S1	3C1
5	12	M30	12 x 12 = 144	3R2	3S2	3C2
6	12	M30	14 x 12 = 168	3R3	3S3	3C3
7	12	M40	10 x12 = 120	4R1	4S1	4C1
8	12	M40	12 x 12 = 144	4R2	4S2	4C2
9	12	M40	14 x 12 = 168	4R3	4S3	4C3

5.1 Notifications of Specimens of 20mm

- 2R1,2R2,2R3 are the M20 Grade of Concrete Rectangular Head with different Embedment Length 200mm,240mm and 280mm respectively
- 3R1,3R2,3R3 are the M30 Grade of Concrete Rectangular Head with different Embedment Length 200mm,240mm and 280mm respectively
- 4R1,4R2,4R3 are the M40 Grade of Concrete Rectangular Head with different Embedment Length 200mm,240mm and 280mm respectively
- 2S1,2S2,2S3 are the M20 Grade of Concrete Square Head with different Embedment Length 200mm,240mm and 280mm respectively
- 3S1,3S2,3S3 are the M30 Grade of Concrete Square Head with different Embedment Length 200mm,240mm and 280mm respectively
- 4S1,4S2,4S3 are the M40 Grade of Concrete Square Head with different Embedment Length 200mm,240mm and 280mm respectively
- 2C1,2C2,2C3 are the M20 Grade of Concrete Circular Head with different Embedment Length 200mm,240mm and 280mm respectively
- 3C1,3C2,3C3 are the M30 Grade of Concrete Circular Head with different Embedment Length 200mm,240mm and 280mm respectively
- 4C1,4C2,4C3 are the M40 Grade of Concrete Circular Head with different Embedment Length 200mm,240mm and 280mm respectively.
- These notifications are also applicable in 16mm dia. of Bars (embedment depth 160mm , 192mm, 224mm) and 12 mm dia. of bars (embedment depth 120mm,144mm,168mm) respectively.

5.2 Specimens testing photos

(1) 2R1 = M20 Rect. Head with Embedment length 200mm (20mm dia. of Bar)

Specimens Set-up

Cracks Develops

Splitting failure of Cube (SFC)

pull out headed bar

(2) 2S1 = M20 Square Head with Embedment length 200mm (20mm Dia. of Bar)

Specimens Set-up

Splitting failure of Cube

Pull out headed bar

(3) 4R1 = M40 Rect. Head with Emb. Length 200mm (20mm Dia. of Bar)

Specimens Set-up

Cracks formation

Thread failure

(4) 3C2 = M30 Circular Head with Emb. Length 240mm (20mm Dia. of Bar)

Specimens Set-up

Crack formation

Thread failure

5.3 Results & Conclusion

(20mm,16mm,12mm Dia. Of Bars)

- **Bond Stress - Different Embedment Length**

(a) Rect. Head, 20mm Dia., M20, M30 & M40

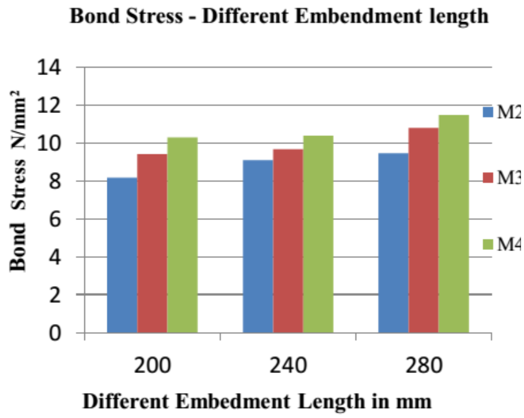

(b) Square Head, 20mm Dia., M20, M30 &M40

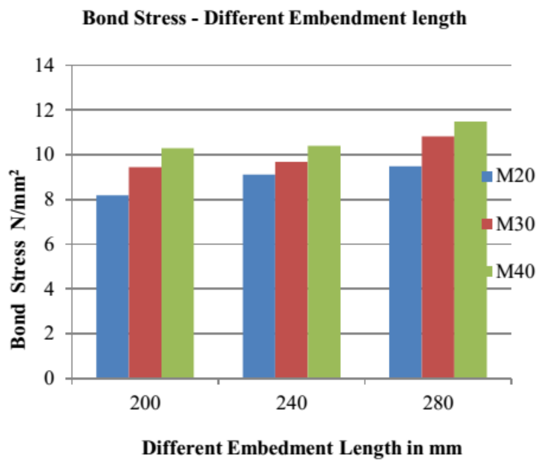

(c) Circular Head,20mm Dia.,M20,M30& M40

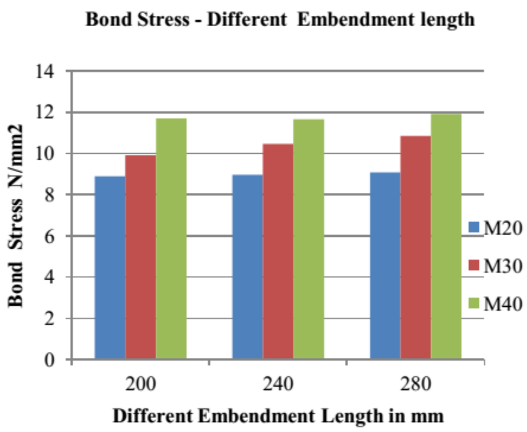

➢ **Bond Stress – Max load**

(a) Rect. Head, 20mm Dia., M20, M30 & M40

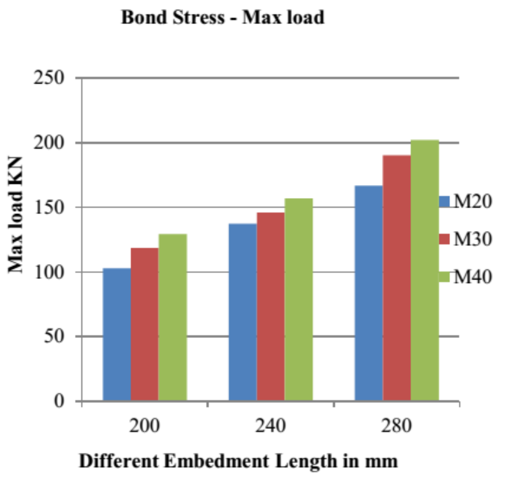

(b)Square. Head, 20mm Dia., M20, M30 & M40

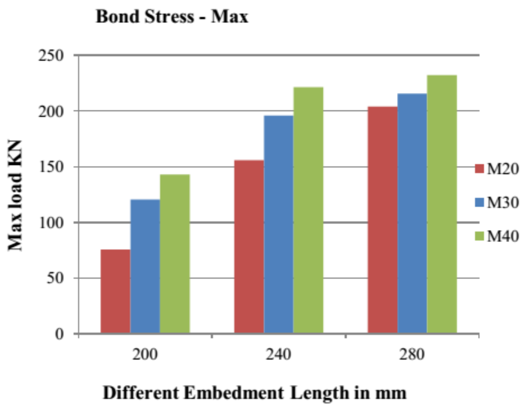

(c)Circular. Head, 20mm Dia., M20, M30 & M40

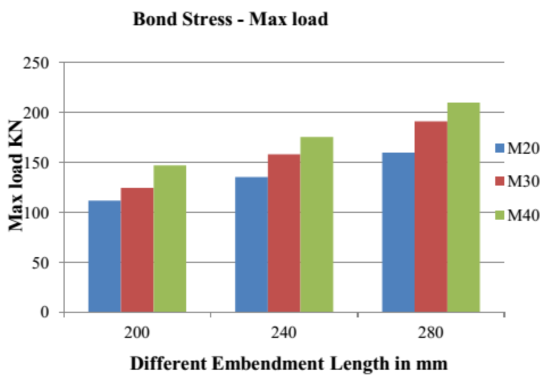

➢ These kinds of results are also found in 16mm dia. of Bars (embedment depth 160mm , 192mm, 224mm) and 12 mm dia. of bars (embedment depth 120mm,144mm,168mm) respectively

➢ Bond stress increases with increment in embedment length.

- Pull out load increases with increment in embedment length.

Abbreviations:

- A_{brg}: Net Bearing Area Of The Head
- A_b: The Bar Area
- Db: Diameter of Bar
- Ed: Embedment Length
- Ah: Area of Head
- Dh: Diameter of Head
- La: Anchorage Length
- Sh: Size of Head
- Hd:EmbedmentDepth

Acknowledgement

I would like to gratefully acknowledgement my Guide **Prof. S M Kulkarni (PIET VADODARA) and my institutes (PIET VADODARA)** for his precious guidance, constant inspiration and encouragement throughout the period of my dissertation.

References

[1]. ACI CODE A318 – 08 "Building Code Requirements for Structural Concrete"

[2]. ASTM A 970/A 970 M – 13 Standard Specification for Headed Steel bars for Concrete Reinforce.

[3]. Dong uk – choi "Test of Headed Reinforcement pullout" (IJCSM august 30, 2006.

[4]. Dong uk choi ". Test 0f Headed Reinforcement pullout" KCI JOURNAL SEP 5, 2002.

[5]. www.hrc-europe.com

[6]. www.erico.com

[7]. www.utexas.edu

SECM/15/144

The use of flexible flaps in improving the settlement resistent behaviour of raft foundations

J.M.C.J.Jayasundara[1*], B.M.K.L.K.Basnayake[1] and K.G.H.C.N.senaviratne[1]

[1]University of Peradeniya, Kandy, Srilanka
*E-Mail: j.m.c.j.jayasundara@gmail.com, TP: +949714990049

Abstract: Today shallow foundation construction in soft soils faces many problems due to low bearing capacity of soft soil. Although deep foundations can be used as an alternative, considering the costs and the time involved, the approach is proven to be uneconomical. This has led many researchers to design innovative shallow foundation systems for construction on soft soils, with adequate bearing capacity, while minimizing the settlement. Two such foundations are the “Cakar Ayam foundation” and “Akar foundation”, which are currently used in construction industry in countries like Malaysia.

Two vertical flexible flaps attached to the underneath of a raft were used as a modified foundation model in this project to see it the foundation is capable of reducing the settlement when built on soft soil. The physical models of the modified foundation were built by varying the flap length and tested under different loads. Further, the models were analysed using finite element package, PLAXIS. The results obtained from physical modelling and finite element analysis showed that the foundation can be used to reduce excessive settlement on soft soil. The settlement reduces with the increase of flap length. Finally, the results verified that the modified foundation can be used as a temporary foundation to build a working platform for construction vehicles to pass through the working site.

Keywords: Settlement, Flexible, Foundations, Raft, Flap

1. INTRODUCTION

Good quality soils are always preferred in civil engineering projects, where the bearing capacity of the grounds is sufficiently high and the resulting settlement is non-excessive. However, these sites may not be readily available with the increase in world population and land use, making it inevitable to construct on less favourable soils [3].The common solution adopted in such difficult cases is to construct deep foundations such as pile foundations. Although the piles serve the purpose well by transferring the load to a firm stratum deep down in the subsoil, the scale of machinery, materials, labour, costs and time involved are inevitably high. Thus, the approach may prove to be uneconomical and even unwise with over-designs to counter the poor soil quality.

Countries like Malaysia have extensive deposits of peat and organic soils which makes development on such areas a challenging task for civil engineers. This has led many researchers to design innovative shallow foundation systems on soft soils which have adequate bearing capacity while minimizing the settlement. Two such foundations are the “Cakar Ayam foundation” [1],[4] and “Akar foundation”[2]. Dr. Ir. Sedyatmo (1961) from Indonesia, proposed the use of the locally termed “Cakar Ayam” or “Chicken Feet” [4] foundation system that consisted of a reinforced concrete slab resting on a number of reinforced concrete pipes. The passive soil pressure creates a stiff condition of slab-pipe system, enabling the thin concrete slab to float on the supporting soils with the pipes kept in vertical positions. The foundation system, termed the “Akar Foundation”, literally translates as “Root Foundation”. It is a lightweight platform supported by a group of pipes. This foundation mainly serves dual functions; to collectively exert a stronger grip of the soft soils hence giving higher bearing capacity, and to spread the imposed structural load evenly into the subsoil thus avoiding excessive and non-uniform settlements. Research conducted has shown the effectiveness of both foundations depending on several parameters such as compatibility of the pipe spacing, individual pipe lengths, raft dimensions and the load applied. In a promising light, the reduced settlement of both foundations when compared to a raft foundation, has

illustrated the potential of the "Akar foundation" [2] and "Cakar Ayam foundation" [1]as economical and effective foundation systems in soft soils.
In this study, the ability of a shallow foundation; which is made of a rigid raft, underneath to which two flexible vertical flaps are attached, to reduce the settlement was identified as the modified foundation system. The objectives was to investigate the model behaviour of the modified foundation in a soft soil and to compare the observed behaviour of the proposed foundation with that predicted by the finite element analysis. The study was limited to identifying only the influence of the flap length and to the behaviour of the foundation, while keeping all the other parameters such as raft dimensions constant and connectivity between flaps and the raft fixed. The finite element analysis of the foundation was carried out using only finite element software, PLAXIS and only a 2D model of the foundation was analysed.

2. MATERIALS & METHODS

2.1 Selection of a location for soil sample collection and soil testing

First task of the project was to identify a location with soft soil with suitable soil parameters and collect samples of that soil for physical model testing. For this task, four locations in Panideniya town, Kandy were identified. Vane shear tests were then carried out in those four locations to find the in-situ shear strength of the soil at depths 0.5m and 1m from the ground level. The location with the least shear strength was identified as the most suitable location and soil samples were obtained at a depth of 0.5m from the surface. The collected soil samples were protected and preserved with wax at the laboratory, to find soil properties of the selected soil. Finally laboratory tests were carried out to identify required soil parameters (Table 2.1).

Table 2.1: Properties of the soil

Property	Value
Natural moisture content	51%
Liquid limit	45%
Plastic limit	24%
Plasticity index	20 %
Organic content	6.8%
Specific gravity	2.58
Undrained shear strength	14 KPa
Young's modulus	1800 KPa

2.2.Theoretical calculations

According to the theory of elastic settlement of foundations by Steinbrenner in 1934, elastic settlement, Si = C_s q b ($\frac{1-v2}{Es}$) [7], [6]. Using above equation elastic settlement of the raft was calculated for further verifications.

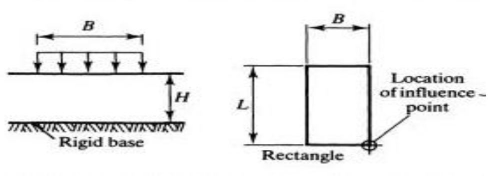

Since L/B = 75/4 = 1.875 and H/B = 200/4 = 5, from figure 3.7, C_S= 0.50.
Substituting the data, Es = 1800 KPa, v= 0.495, C_S= 0.50 and q= 17.5 KPa (Elastic failure under raft foundation – found from Plaxis) for the equation,

$$S_I = C_S\, Q\, B\, \left(\frac{1-v2}{Es}\right)$$
$$= 0.50 * 17.5 * 0.08*\left(\frac{1-0.4952}{1800}\right)$$
$$= 294*10^{-6}\ \text{m}$$

Therefore, elastic settlement at the mid span of the raft is 0.294mm.

2.3 Dimensions of the model

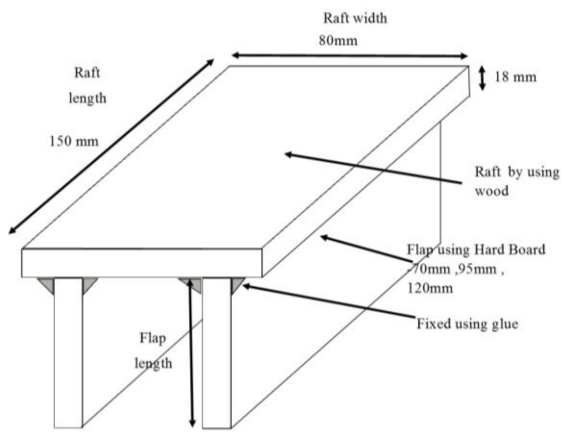

Figure 2.1: Proposed model

Selected dimensions for the foundation,
Raft – 18*80*150 mm
Flap depths – 70, 95, 120 mm
Flap thickness, length – 3mm, 150mm

2.4 Finite element model analysis using Plaxis

The Plaxis analysis was performed for 2-D model of the proposed foundation using Mohr-Coulomb model under plane strain conditions. The boundary was the dimensions of the soil box and the boundary conditions were fixed[5]. 15 node triangular elements were used in developing the mesh. The input parameters for the soil such as Young's modulus, unit weight, cohesion used in the Plaxis analysis were the results from the soil tests. The Poisson's ratio of the soil was used as 0.495 assuming incompressibility of soil. The rigid material was assigned with the material properties of wood and the flexible material were assigned with material properties of hardboard.
The Plaxis analysis was carried out for the foundation model by varying the length of the flaps. A rigid raft was used as the control model to find the effectiveness of the proposed foundation.

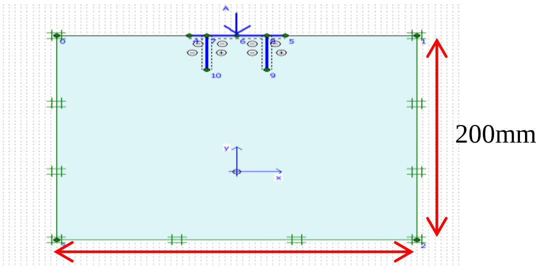

Figure 2.2: the foundation model used in the analysis

The length of the flap was varied in the model as 70mm, 95mm and 120mm and the variation of the vertical mid-point deflection of the raft with the flap length was determined. In each case, the behaviour of the raft and the flap was analysed individually.

2.5 Physical model testing

The rigid raft- flexible flap combination was the only foundation model that was used for physical testing, since it was the main aim of the project. Thus prepared physical models were tested under different loads to identify the settlement behaviour of this foundation on soft soil. The results obtained from physical testing were compared with the finite element analysis results obtained on the same models.

2.5.1 Model Preparation

Four models were prepared which included three physical models of the proposed foundation (rigid raft to which two flexible flaps are attached underneath) with flap lengths 70mm, 95mm, 120mm and the control model (a rigid raft). Hardboard was used for the flap and wood was used for the raft. The two flaps and the raft were joined together with glue. The experimental model is shown in Figure 2.3.

Figure 2.3: The experimental model

The loading from a triaxial apparatus was used to apply the load to the physical model when conducting the experiment. Since the loading applied through the tri-axial apparatus was through one point, a loading arrangement that would provide a distributed loading was required.
Figure 2.4 shows the loading arrangement that was designed and made with steel to suit this purpose.

Figure 2.4: The loading arrangement

2.5.2 Test procedure

First, the experimental model was placed in the soil sample such that the raft was seated on the top soil surface and the two flaps were inserted into the soil, but the vertical edges visible through the glass box as shown in Figure 2.5. In order to ensure the visibility of these vertical edges of the flaps, they were painted with white paint prior to inserting into the soil. The horizontal bar of the loading arrangement was placed along the groove made along the center line of the raft, while the vertical bar was connected to the tri-axial apparatus. A dial gauge with a least count of 0.002mm was placed on the horizontal bar of the loading arrangement, to measure the mid span vertical deflection of the raft. Then, the load was applied at a rate of 0.05mm/min to the model, until the ultimate load of 5.76 kN/m was achieved. The consequent load applied to the model was measured using a 250lb proving ring connected to the loading frame of the tri-axial apparatus. At the end of the test, the deflected shapes of the flaps were marked on the Perspex wall before withdrawing it from the soil sample. The same procedure was repeated for all the other models.

Figure 2.5: The physical model testing

3 RESULTS AND DISCUSSION

3.1 Physical model testing

Variation of the mid-point vertical displacement of the raft with the load applied for the rigid raft-flexible flap model with different flap depths and the rigid raft are shown in Figure 3.1.

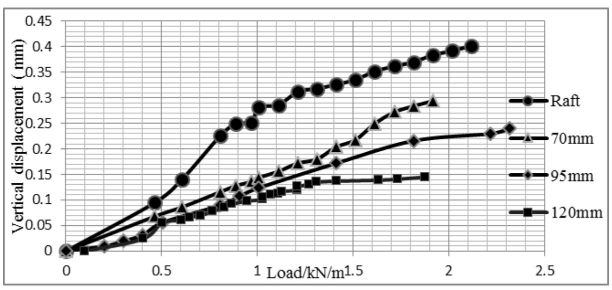

Figure 3.1: Variation of mid-point deflection of the raft with the load applied for the rigid raft-flexible flap model with different flap length and the rigid raft

The variation between the mid-point deflection of the raft and the load applied was obtained for rigid raft-flexible flap foundation model through physical model testing as depicted in Figure 2.5. It is clear from the results obtained, that when the flap length increases, the mid span deflection of the raft reduces.

3.2 Plaxis analysis results

The mid-point vertical displacement of the raft of rigid raft - flexible flap model with different flap lengths 50mm, 95mm, 120mm, 175mm and 225mm, at different loads applied (1kN, 2kN, 3kN,4kN, 5kN and 5.6kN) were obtained as follows. The model had a fixed spacing between the two flaps of 50mm. The behaviour of the raft was only analysed here.

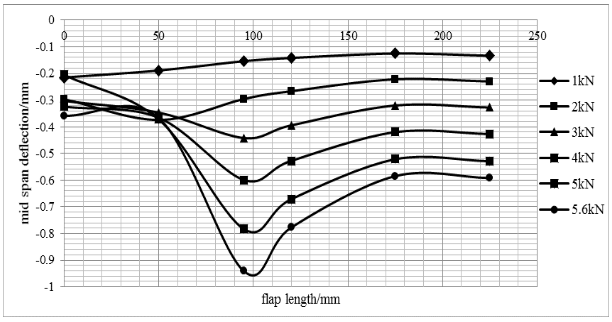

Figure 3.2: Variation of the mid span deflection with the flap length for different applied loads

When considering the above results, it is clear that with the increase in the applied loads, the mid-span deflection of the raft increases in the models with the flap length up to 100mm. But in the models with the flap length more than 100mm, the mid span deflection of the raft starts to reduce gradually.
Therefore, it is evident that the models with flap length less than 100mm exhibits a rigid behaviour by punching into the soil continuously with the application of loads and the models with flap length more than 100mm exhibits a flexible behaviour by bending the flaps.
When the lateral deflection and the bending moments of only the flaps were analysed, some of the flaps showed behaviour similar to that of a short or rigid pile, while some other flaps exhibited behaviour similar to a long elastic pile. This is illustrated in Figure 3.3 and Figure 3.4.

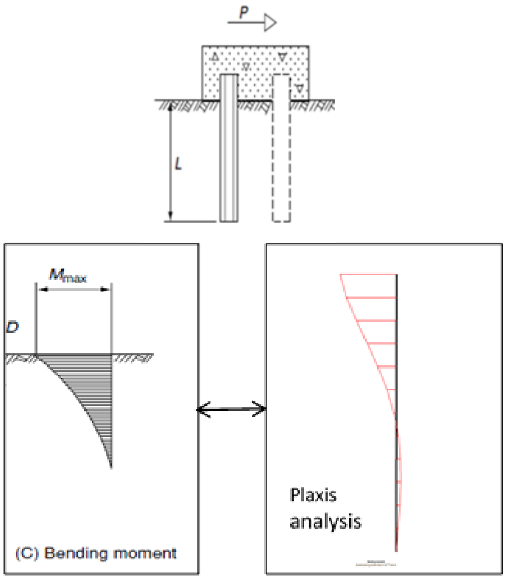

Figure 3.3. The similarity in the bending behaviour of short piles to that of the bending behaviour of 50mm flap

For a pile to behave as a short or rigid pile, the ratio between the length of the pile and relative stiffness coefficients in clay should be less than or equal to two. From calculations, the ratio obtained for 50mm flap was 1.82 which proves that theoretically the flap behaves as a rigid pile. The limiting length value of a flap length to raft width is 0.33 in order to behave as a short pile.

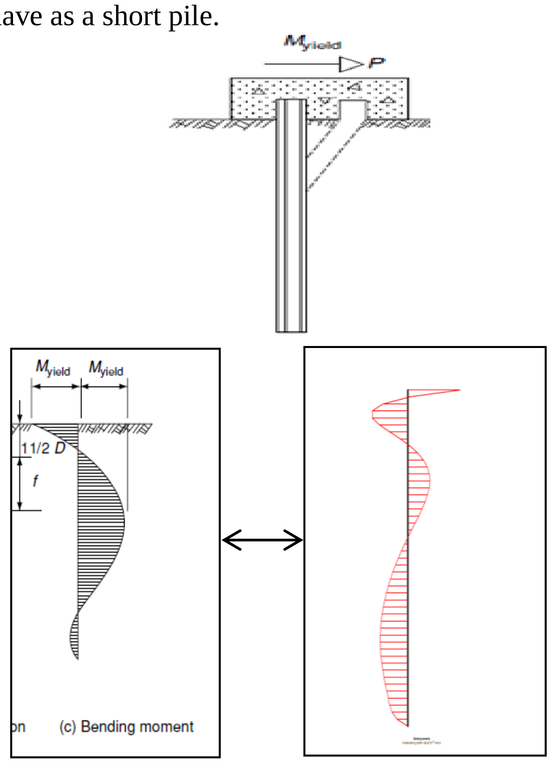

Figure 3.4. The similarity in the bending behaviour of short piles to that of the bending behaviour of 175mm flap

For a pile to behave as a long or elastic pile, the ratio between the length of the pile and relative stiffness coefficients in clay should be greater than 4.5. The value of this ratio obtained for the 175mm flap was 6.4, which is well above 4.5 . Thus this flap behaves similar to a long pile. The limiting value of flap length to raft width 0.83 is required to behave as a long piles.
So any flap length to raft width ratio between 0.33 and 0.83 behaves as an intermediate pile.

3.3 behaviour of the raft

Figures 3.5,3.6,3.7,3.8 indicate the individual comparison between physical test results and Plaxis analysis result for rigid raft- flexible models with flap lengths 70mm,95mm,120mm) and rigid raft.
1. Rigid raft

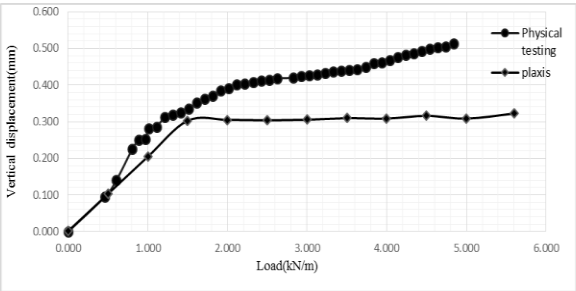

Figure 3.5: Variation of the vertical displacement of the mid-point of the raft with the load applied for the rigid raft

2. Rigid raft-flexible flap model with flap length 70mm

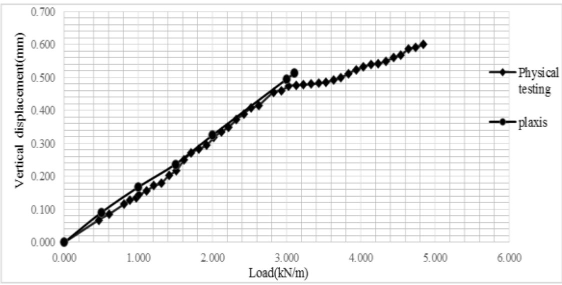

Figure 3.6: Variation of the vertical displacement of the mid-point of the raft with the load applied for the rigid raft-flexible flap model with flap length 70mm

3. Rigid raft-flexible flap model with flap length 95mm

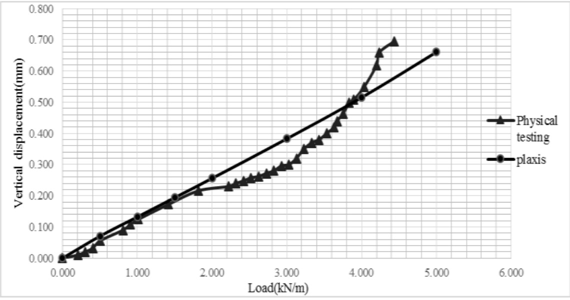

Figure 3.7: Variation of the vertical displacement of the mid-point of the raft with the load applied for the rigid raft-flexible flap model with flap length 95mm

4. Rigid raft-flexible flap model with flap length 120mm

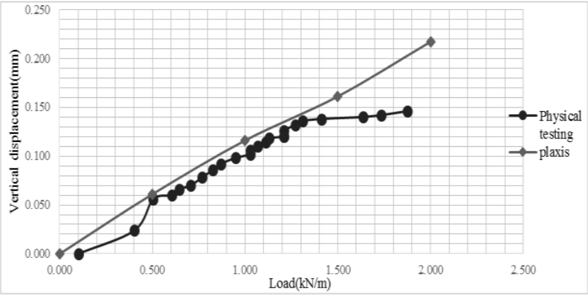

Figure 3.8: Variation of the vertical displacement of the mid-point of the raft with the load applied for the rigid raft-flexible flap model with flap length 120mm

Although the values obtained for the vertical displacement of the raft at a specific load applied, is nearly equal in both physical testing and Plaxis analysis, there are deviations between the physical testing and Plaxis analysis results. These variations may be due to, errors in carrying out the physical testing, initial disturbance to the soil sample when obtaining it and inserting the model, errors in the instruments used and absorption of moisture in the soil by the hardboard.

3.4 Behaviour of the flap

Figure 3.9: Behaviour of flap in physical testing for the rigid raft-flexible flap model with flap length 70mm

The similarity in the behaviour of the flap in physical testing and Plaxis analysis is shown in Figure 3.9 and Figure 3.10 for the model with 70mm flap length. Other models 90mm and 120mm flap length models also showed a similar pattern.

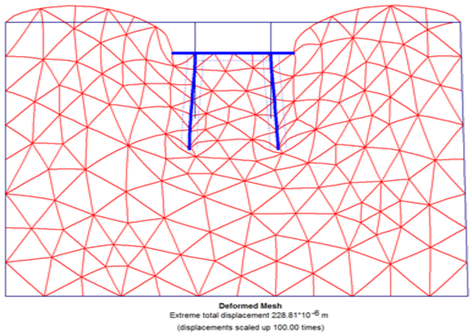

Figure 3.10: Behaviour of flap in Plaxis analysis forthe rigid raft-flexible flap model with flap length 70mm

3.5 Behaviour of the soil

During the physical model testing, the soil on either side of the raft exhibited a bulging behaviour outwards, with the increase in the load application. This behaviour is clearly shown in Figure 3.11.

Figure 3.11: The bulging behaviour exhibited by the rigid raft-flexible flap foundation model under applied loads

The same behaviour is shown by the model analysed using Plaxis and thus can be explained using plaxis. Figure 3.12 shows the total displacement of the soil in the model. According to this figure, the soil underneath the raft moves vertically downwards. This movement causes the soil near to the flap to move laterally and ultimately vertically upward, away from the raft this results in the soil bulging.

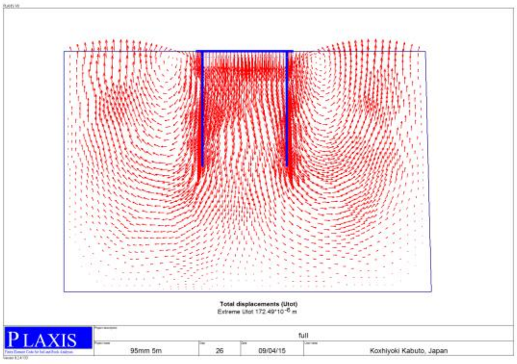

Figure 3.12: The bulging behaviour exhibited by the rigid raft-flexible flap foundation model under applied loads

4. CONCLUSIONS

In this project, the settlement behaviour of the physical model and the finite element Plaxis model which was made of a rigid raft, underneath to which two flexible vertical flaps were attached was analysed and the following conclusions can be summarized by observing the results.

(1) The improvement of the settlement resistant behaviour is remarkably increased in both physical model and finite element Plaxis model with the increase of the flap length. The vertical displacement pattern of the raft in both physical model and finite element model are similar.

(2) A decrease in the vertical displacement of the raft is seen with the increase of the flap lengths and also a reduction in the horizontal displacement of the flaps occur with the increase of flap length.

(3) The vertical displacement undergone by all the points on the raft are all most similar in value in rigid raft model, which is similar to a punching behaviour.

(4) When the soil underneath the raft undergoes a vertical movement due to the applied load, in order to keep the total strain constant, a quantity of soil has to move in the lateral direction resulting in a horizontal deflection of the flaps connected to the raft. Thus, the flap and the raft mutually influence each other's deflection behaviour.

(5) The same soil bulging behaviour shown by the model when analysed using Plaxis was shown when conducting physical testing. Thus it can be explained using the total dispalcement behaviour of soil in Plaxis. When the soil underneath the raft moves vertically downwards the soil near to the flap try to move laterally and ultimately vertically upward, away from the raft resulting in the soil bulging.

(6) The percentage reduction in settlement is highly depended on the flap length of the two flaps.

(7) When comparing with laterally loaded pile behaviour, the flap lengths to raft width ratio lesser than 0.33 behave similar to the short piles, and flap lengths to raft width ratio more than 0.83 behaves similar to long piles.

Acknowledgement
We would like to thank our project supervisor Prof: K.G.H.C.N. Seneviratne for supervising and guiding us to make our project a successful one and the panel members, Prof. U. de S. Jayawardana and Dr. (Mrs.) D. de S. Udakara for evaluating and instructing us.

References

[1]. Ahmad, H.M.N. , Yahuda, A.Y. & Pakir, F. , 2014. Analysis of Lightweight Concrete "Cakar Ayam" Foundation for Road Construction using Plaxis 3d Foundation Software. Applied Mechanics and Materials, Vol. 695 (2015), p. 729- p.733.

[2].Chee, M.C., Pik, Y.W. & Chai,C.L.,2010.Subsidence Control of Construction on Soft Soils with "Akar foundation. Modern Applied Science, Vol. 4, No. 8.

[3].Taha, M.R. & Majeed, Z.H., 2000. Effect of Nanomaterial Treatment on Geotechnical Properties of a Penang Soft Soil. Journal of Asian Scientific Research, Vol. 2(11), p. 587- p.592.

[4].Tandjiria, V., 1999 .Numerical modelling of Chicken-Foot Foundation. Dimensi Teknik Sipil, Vol. 1(1).

[5].Teshome, F. & Ismail, A., 2011. Analysis of Deformations in Soft Clay due to Unloading. Master Of Science Thesis in the Master's Programme Geo and Water Engineering, Vol. 23.

[6]. Gunaratne, M., 2006. Foundation Engineering Handbook. Taylor & Francis Group, Boca Raton. Chapter 8, Pg. 328.

[7]. Bowles, J.E., 1976. Foundation Analysis and Design. Fifth Edition. The McGraw-Hill Companies, Inc., Singapore. Chapter 16.15, p.929, Chapter 18.7, P.1062

SECM/15/146

Investigation on Ground Vibration Induced by Construction Traffic and Normal Traffic

P.H.D.P. Chandarasiri [1*], G.H.M.J.S. De Silva [1] and G.S.Y. De Silva.[1]

[1]Faculty of Engineering, University of Ruhuna.
*Email: dilankapc@gmail.com

Abstract: With the development of infrastructure facilities all over the country, many construction activities are carried out causing the construction traffic increased. As a result of movement of heavy vehicles, people feel annoyances so that many complaints against this construction traffic have been arisen. Objective of this study is to investigate the characteristics of the ground vibrations induced by construction traffic and normal traffic.

A road construction site and a road near to stone crusher were selected. Ground vibrations induced by five dump trucks and one vibrating roller at 1m away from the edge of the road were measured using the four channel seismograph. Ground vibration levels experienced during period of construction traffic were greater than that for normal traffic and dominant in vertical direction. When operating a dump truck, Peak Particle Velocity (PPV) of the ground vibration in the vertical direction was in the range of 0.127-1.400mm/s while transverse and longitudinal directions ranges were 0.079-0.730mm/s and 0.127-0.825mm/s, respectively. Maximum vibration range experienced was 2.70-4.16mm/s induced by vibrating roller in vertical direction. Their transverse direction and longitudinal directions vibrations levels ranged from 1.41 mm/s to 2.05mm/s and from 1.49 mm/s to 3.35 mm/s, respectively. Vibrations induced by passenger vehicles ranged from0.079 mm/s to 0.143mm/s in all three directions. People may feel annoyances from construction traffic because the construction traffic moves continuously and induced greater PPV compared with normal traffic.

Key words: Construction traffic, Ground vibration, People annoyance, Seismograph

1. Introduction

Construction traffic has been widely increased in Sri Lanka with the development of infrastructure facilities around the country. Heavy vehicles are moving and several construction activities are performing in construction processes. Significant ground vibration levels were reported from construction activities including rock blasting [1] pile driving and soil compaction [2], although movements of heavy vehicles including dump trucks, vibrating rollers, excavators and backhoe loaders are very common in and around construction sites. Due to these unlimited movements of heavy vehicles, vibrations are induced on the ground. Those vibrations propagate towards the building as well as humans.

There are three types of seismic waves; compression waves (P), shear waves (S) and surface waves (R). Among these waves, surface waves propagate with high intense towards humans and buildings and result annoyances and failures on them [3]**.** It has been found that 26% of the energy transmitting through these waves goes into shear waves, 7% goes into compression waves (longitudinal waves) and 67% of input energy goes into surface waves (Rayleigh waves) [4]. It proves that higher amount of input energy transmits through Rayleigh waves.

People, who live in the area, where infrastructure facilities are being developed, experience annoyances due to ground vibration induced by construction traffic. Among the annoyances and damages that people have to face, 37% of the people have experienced annoyances and damages due to the vibrations induced by construction traffic and 8% were seriously bothered [5]. Therefore many complaints have been arisen against the vibrations induced by construction traffic. When implementing the Southern Transport Development Project (STDP) in Sri Lanka, among 424 complaints which were received to the contractor of this project, China Harbour Engineering Company, upto December, 2008, 61 complaints (14%) have been recorded due to the vibration induced by movement of heavy vehicles. It was only seconded to the complaints arisen against ground vibrations due to pilling, heavy machinery (91 complaints, 21%) [6]. As part of the resource consent process, there is an increasing requirement for road controlling authorities and their consultants to establish whether or not vibrations generated during road construction will be problematic to structures, buildings and occupants of these buildings so that management of such vibrations can be specifically addressed in the construction management plan.

Typically, these vibrations are more likely to cause annoyance. Vibrations may be unacceptable to occupants of buildings because of annoying physical sensations produced in the human body, interference with activities such as sleep and conversation, rattling of window panes, loose objects and fear of damage to the building and its contents. This emphasizes the need to investigate characteristics of ground vibrations induced by construction traffic, in order to reduce the annoyance to people.

2. Objectives

Objective of the current study is to investigate the characteristics of the ground vibration induced by construction traffic and to compare them with the characteristics of ground vibration induced by normal traffic.

3. Methodology

The ground vibrations were measured using a four channel seismograph (Figure 1) which is capable of measuring ground vibrations in all the three directions (i.e., transverse, vertical and longitudinal). Seismograph consists of a standard transducer which senses the ground vibrations propagating through the ground where the transducer is located. The ground spikes were screwed into the bottom of the standard transducer and pushed fully into the ground. The standard transducer, geophone, was leveled on the ground and the arrow mark located on the top of the standard transducer was pointed in the perpendicular direction to the movement of a heavy vehicle which induces the ground vibration. Before measuring vibration, the instrument was set up to the standard mode.

For measuring the vibration induced by construction traffic, it was selected three sites: a highway construction site, a road near to stone crusher and a normal transportation road. The selected sites were free from vibrations induced by other sources.

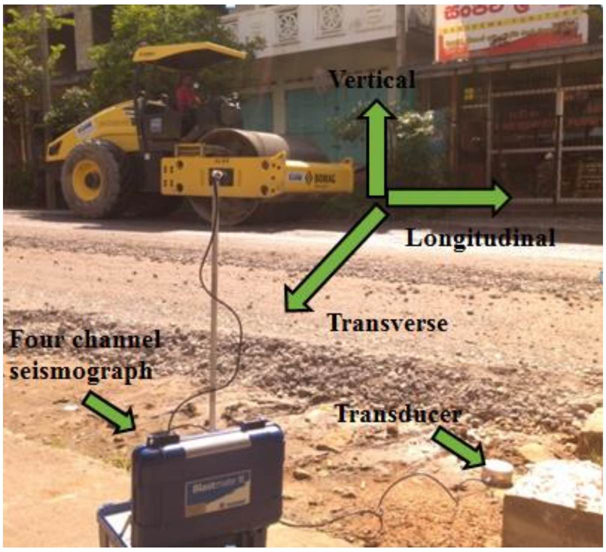

Figure 1 : Measuring ground vibration induced by a vibrating roller

To investigate the vibration induced by construction traffic, it was mainly considered two types of heavy vehicles: dump truck and vibrating roller. In the case of measuring ground vibrations induced by normal traffic, it was selected 4 types of vehicles; car, van, three wheel and bus. The vehicle induced ground vibration was measured at 1m away from the edge of the road. This distance was selected because if the distance to the measuring point was more than 1m away from the road, there were many obstacles which might be capable of damping the vibrations propagating through them.

For investigation of vibration induced by dump truck, measuring was performed for 5 types of dump trucks. When measuring the vibration, it was ensured that the minor vibration from the other sources and the disturbances from the surrounding environment were controlled up to minimum level. . When measuring vibration induced by a vibrating roller (Figure 1), only one vibrating roller was selected and vibration induced at five different working capacities was measured. The working capacities were based on the induced vibration levels and the moving speeds of the vibrating roller. The operator was instructed to move the vibrating roller by changing the speed and the level of vibrations induced on the road. Among the ground vibrations induced at various working capacities, it was selected highest five vibrations records induced by the vibrating roller. The magnitude of vibration is presented by peak particle velocity (PPV) in the unit of mm/s. However, as the effect of vibrations induced by movement of heavy vehicles lasts for a certain time, in addition to PPV, root mean square (rms) value was also determined. PPV presents the maximum velocity of the vibrations propagated during the time period of one second while rms presents the root of square of all the vibration induced during the period of one second. It might not be appropriate to relay on only the PPV induced by vehicles since during the time of one second which the seismograph records, it is possible that the surrounding vibrations may superimpose with the vibration induced by vehicle at the time when the vibrations are measured. As a total representative of the vibrations induced by vehicles throughout one second, rms indicates reliable and acceptable results.

4. Results and Discussion

Peak particle velocity (PPV) and root mean square (rms) of the ground vibration induced by five different types of dump trucks are shown in Tables 1 and 2, respectively. The ground velocity waves induced by dump truck 4 (i.e., DT4) is shown in Figure 2.

Table 1 : Peak particle velocity of vibration induced by dump trucks

Dump Truck	Trans. (mm/s)	Vert. (mm/s)	Long. (mm/s)
DT 1	0.730	1.400	0.825
DT 2	0.079	0.143	0.143
DT 3	0.127	0.222	0.254
DT 4	0.460	1.290	0.825
DT 5	0.111	0.127	0.127

DT: Dump Truck

When moving a dump truck, ground vibration represented in PPV in vertical direction is generally higher than other two directions (Figure 2, Table 1). However, dominant vertical ground vibration induced by each dump truck is evident in magnitudes presented by rms. (Table 2). The maximum vibration level induced by a dump truck was 1.4mm/s (PPV) (Table 1) and 0.451mm/s (rms) (Table 2) in vertical direction. The vibration range in vertical direction was from 0.127mm/s to 1.4mm/s (PPV), (from 0.037mm/s to 0.451mm/s (rms)) while for transverse and longitudinal directions they were in the range of 0.079mm/s - 0.730mm/s (PPV) (0.023mm/s - 0.265mm/s (rms)) and 0.127mm/s -0.825 mm/s (PPV) (0.035mm/s - 0.302mm/s (rms)), respectively. Vibrations in the level of 0.3 mm/s to 1 mm/s might be perceptible in residential environment (BS 5228-2 [7]). Since the dump trucks induce the vibration with the magnitude greater than 0.3 mm/s, people who are exposure to the vibrations induced by dump truck will percept the vibration and experience annoyances. It will cause complaints against construction traffic.

Table 2 : Ground Vibrations induced by dump trucks in rms

Dump Truck	Transverse (mm/s)	Vertical (mm/s)	Long. (mm/s)
DT 1	0.265	0.451	0.302
DT 2	0.023	0.037	0.041
DT 3	0.035	0.062	0.057
DT 4	0.138	0.314	0.225
DT 5	0.030	0.039	0.035

DT: Dump Truck

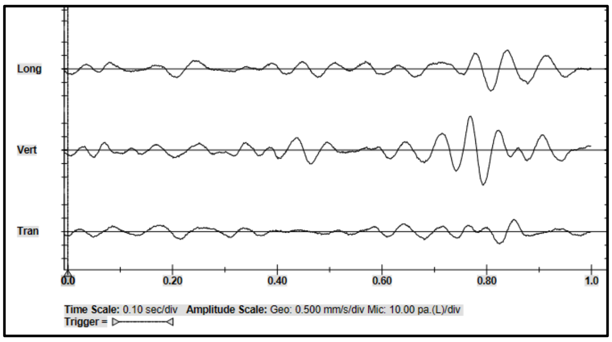

Figure 2 : Ground velocities induced by a dump truck (DT4)

Peak particle velocity (PPV) and root mean square (rms) of the ground vibration induced by a vibrating roller at different working time are listed in Tables 3 and 4, respectively. The ground velocity waves induced by vibrating roller at working time 1 (w.t.1) is shown in Figure 3.

Table 3 : Ground Vibrations induced by vibrating roller in rms

Vibratin g roller	Trans. (mm/s)	Vert. (mm/s)	Long. (mm/s)
w.t.1	1.73	3.71	2.40
w.t.2	1.70	3.40	2.25
w.t.3	1.41	2.70	1.49
w.t.4	1.75	4.16	3.35
w.t.5	2.05	4.00	2.78

w.t.: working time

Similar to dump trucks, vibrating roller induced significant ground vibrations in vertical direction compared with other two directions (Figure 3, Tables 3 and 4). The maximum vibration level induced by a vibrating roller is 4.16mm/s (PPV) (Table 3) (2.808mm/s (rms) (Table 4)) in vertical direction. Vibration level in vertical direction ranged from 2.70mm/s to 4.16 mm/s (PPV) (from 1.207 mm/s to 2.808mm/s (rms)) whilst it was from 1.41mm/s to 2.05mm/s (PPV) (from 0.634mm/s to 1.091mm/s (rms)) and from 1.49 mm/ to 3.35mm/s (PPV) (0.598mm/s to 1.970mm/s (rms)) in transverse and longitudinal directions, respectively. The minimum vibration level induced by vibrating roller is 1.41 mm/s (PPV) which is even higher than the maximum vibration induced by dump truck (1.4 mm/s (PPV)). The vibration induced in the range of 1mm/s to 10 mm/s (PPV) is very hard to tolerate for the people (BS 5228-2 [7]). Even minimum level of the ground vibration (1.41 mm/s (PPV)) induced by vibrating roller is greater than 1mm/s. People who are exposure to this level of vibrations induced by vibrating roller would hardly tolerate the perceptions and annoyances. They will tend to make complaints against the ground vibrations induced by the construction traffic.

Table 4 : Ground vibrations induced by a vibrating roller in rms

Vibrating roller	Trans. (mm/s)	Vert. (mm/s)	Long. (mm/s)
w.t.1	0.968	2.318	1.370
w.t.2	0.770	1.993	1.085
w.t.3	0.634	1.207	0.598
w.t.4	0.856	2.808	1.970
w.t.5	1.091	2.610	1.606

w.t.: working time

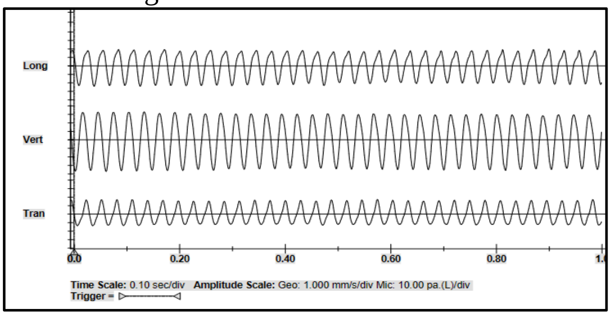

Figure 3 : Ground velocity induced by vibrating roller at working time 1

PPV and rms of the ground vibrations induced by normal traffic (consists of car, van, three wheel and bus) is shown in Tables 5 and 6, respectively.

Table 5 : Ground Vibrations induced by normal traffic in PPV

Vehicle type	Trans. (mm/s)	Vert. (mm/s)	Long. (mm/s)
Car	0.079	0.143	0.127
Van	0.111	0.143	0.143
Three wheel	0.111	0.127	0.111
Bus	0.079	0.127	0.127

Table 6 : Ground Vibrations induced by normal traffic in rms

Vehicle Type	Trans. (mm/s)	Vert. (mm/s)	Long. (mm/s)
Car	0.024	0.035	0.034
Van	0.034	0.036	0.026
Three wheel	0.022	0.029	0.025
Bus	0.025	0.043	0.040

Ground vibration induced by normal traffic (i.e., car, van, three wheel and bus) is approximately equal in all the three directions: transverse, vertical and longitudinal, considering both PPV and rms values (Tables 5 and 6). The maximum vibration level induced by normal traffic was 0.143mm/s (PPV) (Table 5) and 0.043 mm/s (rms) (Table 6). Ground vibrations induced by normal traffic varied from 0.079mm/s to 0.143mm/s (PPV) (0.022mm/s to 0.043mm/s (rms)) considering all the three directions. Vibration up to 0.14 mm/s (PPV) might be just perceptible in the most sensitive situations for most vibration frequencies associated with construction (BS 5228,[7]). Although some components of vibrations (0.143 mms/ (PPV)) induced by normal traffic slightly exceeded the limit recommended in BS 5228 -2 [7] (0.14 mm/s (PPV)), most of the vibrations are below the just perceptible limit.

The dominant vertical frequency contents of the vibrations induced by dump trucks are shown in Table 7.

Table 7 : Frequency content of the ground vibrations induced by dump truck

Dump Truck	Trans. (Hz)	Vert. (Hz)	Long. (Hz)
DT1	2	2	2
DT2	13.5	16	38
DT3	18.5	18.5	53.5
DT4	13	15	15
DT5	16.5	11	12

Unlike vibrating roller, the frequency component of the ground vibrations induced by dump truck is not limited to a single frequency (Figures 4, 6 and Table 8). Vibrating roller induces ground vibration in a single frequency (34.5Hz) (Figure 5 and Table 8) while each dump truck generates frequency range which is unique to particular dump truck. Since dump trucks induced dominant vibrations in vertical directions, the dominant frequency in vertical direction ranged from 2Hz to 18.5Hz which is a lower frequency range that makes high perception to people (Table 7).

Table 8 : Frequency range of the ground vibration induced by construction traffic and normal traffic

Vehicle Type	Trans. (Hz)	Vert. (Hz)	Long. (Hz)
Dump truck	2-18.5	2-18.5	2.53.5
Vibrating roller	34.5	34.5	34.5
Car	95.5	22	54.5
Van	92	90	92
Three wheel	94.5	55	54.5
Bus	12.5	17.5	36.5

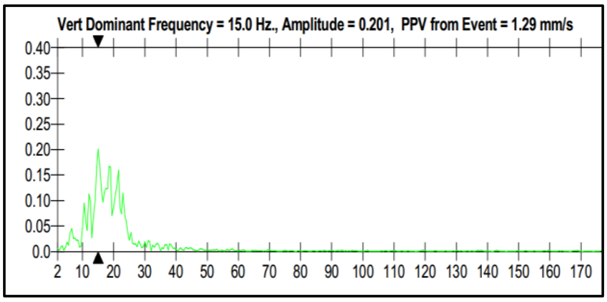

Figure 4 : Fast Fourier Transformation (FFT) of the vertical ground vibration induced by Dump Truck (DT) 4.

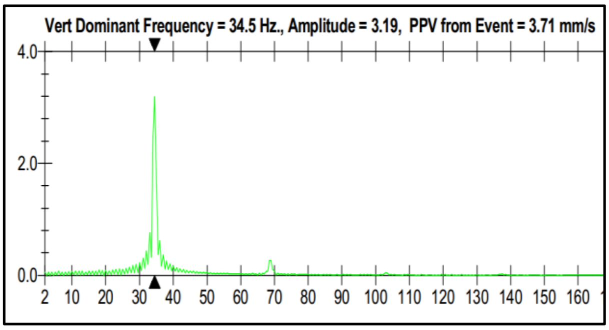

Figure 5 : Fast Fourier Transformation (FFT) of the vertical ground vibration induced by a vibrating roller at working time (w.t.) 1.

Therefore, people might have felt annoyances due to ground vibration at these low frequencies and tended to make complains against ground vibrations induced by construction traffic.

In previous studies, the significant component of ground vibration has been found in transverse direction for construction activities [8]. However, this study confirms that construction traffic induced ground vibration, which is dominant in vertical direction. Unlike ground vibration induced by normal traffic (0.079mm/s-0.143mm/s (PPV)) people may experience more annoyances due to ground vibrations induced by construction traffic (exceed even 4mm/s (PPV)).

5. Conclusion

In this study, the ground vibrations due to construction traffic were investigated and compared with that of normal traffic.

It was found that when construction traffic is on the move, it induces dominant vertical ground vibration. Unlike construction traffic, the ground vibrations induced by normal traffic show minor discrepancy between three directions (i.e., transverse, vertical and longitudinal). Among dump truck and vibrating roller, vibrating roller induces greater PPV of 4.16 mm/s compared to that of dump truck (1.4 mm/s). The ground vibration induced by construction traffic exceeds the minimum perceptible level of 0.3mm/s. The normal traffic induces vibrations range from 0.079 mm/s to 0.143 mm/s (PPV) which is significantly lower magnitude compared to ground vibrations induced construction traffic.

Dump trucks generate ground vibrations in the frequency range of 2-53.5H while vibrating roller owns single frequency of 34.5 Hz, when they are on the move. People may feel annoyances because construction traffic moves continuously and induced ground vibration with greater magnitude at lower frequencies compared that with normal traffic.

Acknowledgement

Authors would like to express their gratitude to National Research Council (Research Grant NRC 11-193) for providing necessary supports to conduct the research work presented in this paper.

References

[1]. Wickramasinghe,S.A.N.S.,Masakorala,S. R., Jayasinghe, E.A.T.P., Subashi De Silva, G.H.M.J. and De Silva,G.S.Y.,“Effect of Blast Vibration on Wall Panels”, Transactions, Annual Sessions of the Society of Structural Engineers, Sri Lanka, November, 2011, pp. 23-28

[2]. Jayawardhana, W.A.P.D., Jayawardhana, B.M.B.H.,Subashi De Silva, G.H.M.J. and De Silva, G.S.Y., “Investigation on Characteristics of Vibration Induced by Soil Roller Compaction and Effectiveness of Damping Layer to Reduce the Vibration”, Special Session on Design & Construction, Proceedings of 5th International Conference on Sustainable Built Environment (ICSBE-2014),Kandy, Sri Lanka, December, 2014, pp. 129-136.

[3]. Haramy, K.Y. and Henwood, J.T., “Vibrations induced by Construction Traffic”, Case study, Federal highway administration, Denver ,2002.

[4]. Gutowski, T.G. and Dym, C.I., “Propogation of Ground Vibration”, Sound and Vibration, 1976, vol. 49, pp 179-193.

[5]. Watts, G.R., “Traffic Induced Vibrations in Buildings”, Research, Department of transport, Berkshire, 1990.

[6]. Southern Transport Development Project, “Environmental Impact Monitoring”, Annual report, 2008.

[7]. BSI, “Code of practice for noise and vibration control on construction and open sites – Part 2 : Vibration (BS 5228-2:2009)”.

[8]. Wanniarachchi, W.A.M., Welhena, C.M., Subashi De Silva, G.H.M.J.and De Silva, G.S.Y., “Investigation of Characteristics of Vibration induced by Construction Activities and its Effects on Structural Responses”, Proceedings of International Conference on Structural Engineering and Construction Management (ICSECM-2013), Kandy, Sri Lanka, December 13-15, 2013, paper no. SBE/13/141.

SECM/15/153

Prediction of Residual Buckling Strength in Corroded Steel Bridge Members

W.K.N. Sandamali1*, H.P. Wijesena[1] and J.M.R.S. Appuhamy[1]

[1]Faculty of Engineering, University of Ruhuna, Galle, Sri Lanka
*E-Mail: nirashakarunarathna@gmail.com, TP: +94717714086

Abstract: At present, degradation process of steel bridges has become major problem in all over the world. Steel bridges are exposed to numerous degradation processes during long year operation period, which causes various types of defects. Corrosion is one of major cause of deterioration process of steel bridge structures. Because of the corrosion, remaining load carrying capacities of steel bridge structures are gradually decreased. So it is very important to carefully evaluate the remaining strength of steel bridges in order to understand the feasibility of those steel structures for the current usage and to evaluate the necessity of retrofitting of selected corroded members to strengthen the existing structures. There are lots of researches have been conducted in order to find out remaining tensile strength of corroded steel bridge members. To find out remaining buckling strength of corroded steel, previously conducted tensile test results are not accurate. So evaluation of buckling strength is an essential source of information for carrying out a comprehensive evaluation of its current buckling strength capacity and also the parameters involve in the method should be easily measurable.

There is a need of more brisk and accurate assessment method which can be used to make reliable decisions affecting the cost and safety. This study proposes a new method to calculate the remaining buckling strengths by using minimum thickness ratio based on the results of many buckling strength tests conducted on specimens of corroded steel bridge plates with different corrosion conditions based on the results of many compression coupon tests of actual corroded plates. And also, it is an impossible task to predict remaining buckling strength capacities of each and every aged bridge structure by conducting experiments and so nowadays, the finite element analysis method has become the most common, powerful and flexible tool in structural analysis and makes it possible to predict the strength of complex structures more accurately than existing classical theoretical methods. Further, since it is not easy to measure several thousands of points, to accurately reproduce the corroded surface by numerical methods and to predict their buckling behaviours, a simple and reliable analytical model is proposed by measuring only the maximum corroded depth (tc,max), in order to estimate the remaining strength capacities of actual corroded members more precisely.

Keywords: Corrosion, Remaining buckling strength, Steel bridges, Finite element analysis

1. Introduction

Use of steel in structures goes over 100 years. There are many advantages of use of steel in structures, such as steel exhibits a desirable physical property that makes it one of the most versatile structural materials in use and also due to its great strength, uniformity, light weight, ease of use, toughness, ductility, durability and many other desirable properties makes it the material of choice for numerous structures such as steel bridges, high rise buildings, towers, and other structures. Structural steel has a very high yield stress both in compression and tension. As a result of that, the amount of steel used in building to produce the equivalent performance is much less than that of using ordinary reinforced concrete. So as construction material steel was used during last few decades. And also steel is an efficient and economical material for bridge structures.

But major disadvantage of using steel for construction is the quick deterioration in steel with compare to other construction material. Due to the exposure to aggressive environmental conditions and inadequate maintenance, and often causes in reduction in their carrying capacities, Steel structures are prone to age related deterioration, such as corrosion wastage, fatigue cracking, or mechanical damage during their service life can give rise to significant issues in terms of safety, health, environment and financial costs. Corrosion is the most important causes of deterioration of steel bridges. It has been proven that the corrosion played a significant role in the catastrophic collapse of both the Silver Bridge (Point Pleasant, WV) in 1967 (Silver river bridge, 2014)[4] and the Mianus River Bridge (Connecticut) in 1983, USA (Mianus River Bridge, 2014)[3].

Due to the corrosion, remaining load-carrying capacities of steel bridge structures are gradually decreased. So it is essential to carefully evaluate the remaining strength of a steel bridge in order to understand the feasibility of the steel structure for the current usage and to evaluate the necessity of retrofitting of selected corroded members to strengthen the existing structure.

Many researchers have conducted tests on corroded steel based on tensile strength to find out strength reduction due to the corrosion. Although the tensile is most conservative method to evaluate strength reduction but it is not more accurate to calculate remaining strength when a member is subjected to a buckling load. This paper is mainly based on developing a methodology for remaining buckling strength of the corroded steel members with the relation of corroded condition parameters such as maximum corroded depth of corroded steel members. Experimental results can't be used for all the structures practically. Because it is important to conduct numerical analysis due to the difficulty of measuring several thousands of points, to accurately reproduce the corroded surface by numerical methods and to predict their behaviours under compression load, a simple and reliable analytical model is proposed to estimate the remaining strength capacities of actual corroded members more precisely. Actual structures can be analysed based on the numerical analysis. By using experimental results, numerical method can be validated. Then those validated results can be used for the practical application very easily. If it is possible to derive an equation or any numerical analysis with parameters can be measured with respect to the initial thickness, like depth of corroded pit or remaining thickness of the elements then remaining strength can be easily calculated.

2. Methodology

2.1 Experimental Methodology

The specimens were collected from corroded steel bridges. Totally 14 numbers of specimens were prepared from corroded steel plates and two specimens from non-corroded places of each steel bridges were prepared to find out actual material properties of the steel. For that the specimens were tested under tension.

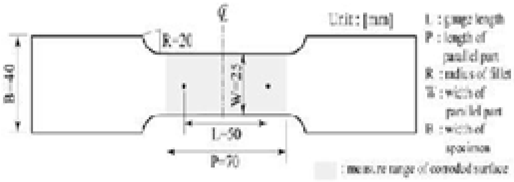

Figure 1: JIS 05 Standard Specimen size for tensile test

Figure 1 shows the JIS standard specimen size used for tensile test. For the compression test 200mm*80mm specimens were prepared.

Figure 2**:** Prepared specimen for the compression test

Figure 2 shows the specimen prepared for compression test. After preparation of specimens all the rust was carefully removed. The thickness of the corroded steel plates should be measured very accurately. The thicknesses of all specimens were measured by using 3D laser measurement system. From the data obtained from thickness measurements the specimens were categorized into three different corrosion conditions according to the minimum thickness ratio (μ). In here the tensile tests were conducted in order to clarify the material properties of test specimens, such as yield strength, modulus of elasticity, ultimate strength, and Poisson ratio can be calculated. Compression test is basically followed to achieve material parameter buckling strength of corroded steel specimens. Here 5mm/min loading speed is provided to the specimen. From the machine it can be obtained Load Vs Displacement graph.

2.2 Classification of Corrosion Levels

All specimens that obtained for the experiment are not being at same corrosion conditions. Hence it is very important to classify corrosion conditions to a few general types for better understanding of their remaining strength capacities considering their visual distinctiveness, amount of corrosion and their expected mechanical and ultimate behaviors based on the numerical values that were obtained from the thickness measurements of each specimen. Three basic corrosion conditions were introduced during this study to be used for reliable remaining strength estimation of actual corroded steel structures They are,

1. Minor Corrosion
2. Moderate Corrosion
3. Severe Corrosion

Corrosion condition of the specimens categorized according to the μ value of each specimen. And μ value obtained from Appuhamy et al (2011) [1]. Table 1 shows the μ value with corrosion conditions.

Table 1: Categorization of corrosion conditions with μ value

μ Value	Corrosion condition
μ> 0.75	Minor
0.75 ≥μ ≥ 0.50	Moderate
μ<0.50	Severe

Where minimum thickness ratio,

$$\mu = \frac{t_{min}}{t_0} \tag{1}$$

tmin = minimum thickness
t0 = initial thickness

2.3 Numerical Methodology

Non-linear finite element method was performed for corroded specimens with different corrosion conditions. The three dimensional solid elements with hexahedral nodal points (HX8M) and updated Lagrangian method based on incremental theory was employed in this analysis. Von Mises yield criterions was assumed for material properties. Maximum corroded pit was modelled by using the representative diameter (D*) which could account for the stress concentration effect and the material loss due to corrosion was considered by using the representative avg. thickness parameter (t*avg) (Appuhamy et.al, 2011) [1].

These two parameters called CCM parameters. To classify members according to the corrosion level based on minimum thickness ratio (μ) (Appuhamyet.al 2011) [1]. For modeling of the specimens ANSYS software was used. First the model is created based on the CCM parameters. Material properties assign to the model from properties obtain from non-corroded test specimen. Then one end of the specimen was fixed and incremental load was applied to the specimen. The applied load varies from 0kN to 200kN. The analyses were conducted until they reach their pre-defined termination limits and the load-displacement behavior for model was obtained. The values obtained from the numerical analysis were compared with experimental results and obtained relationship between numerical results and experimental results.

3. Results and Discussion

3.1 Experimental Analysis

From tensile test results the material properties were calculated. Actual material properties are similar to the JIS standards property value. So, tested material is in the standard quality of steel. Table 2 shows the tensile test results and table 3 shows standard for JIS No.05 specimens obtained from Appuhamy *et.al* (2010) [2].

Table 2: Tensile test results

Specimen No.	Elastic modulus (GPa)	Yield stress (MPa)	Tensile strength (MPa)	Elongation at braking (%)
1	185.2	269	427	24.8
2	183.6	275	435	26.39
Average 1 &2	184.4	272	431	25.59
3	179	243	426	18.24
4	181.2	249	411	20.01
Average 3& 4	180.1	246	418.5	19.12

Table 3: JIS standard tensile test results

Elastic modulus (GPa)	Yield stress (MPa)	Tensile strength (Mpa)
200	245	400-500

Totally 14 no. of specimens were tested including, 6 severe corrode members and 4 members for both moderate and minor corrode members. For non-corroded specimen buckling load is obtained as 173.08kN. Figure 3 shows the relationship between minimum thickness ratio (μ) and the buckling load with all specimens in experiment. Here having a coefficient of correlation of R^2= 0.9575 indicates the high accuracy of the experimental results.

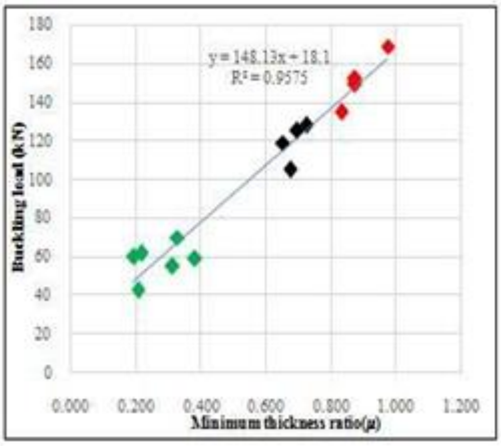

Figure 3: The graph of Minimum thickness ratio Vs Buckling load

From Figure 3,

$$P = 148\mu + 18 \qquad (2)$$

Where,

P= Buckling load

μ= Minimum thickness ratio

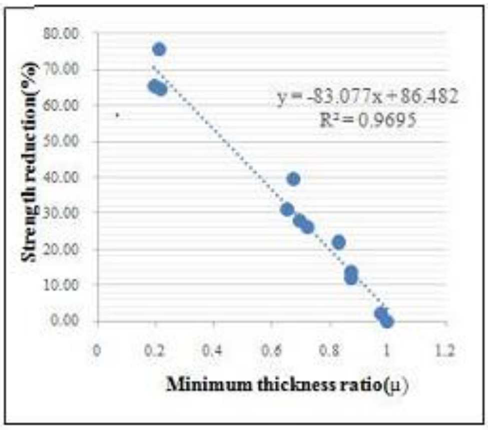

Figure 4: The graph of strength reduction Vs minimum thickness ratio

Figure4 shows the relationship between minimum thickness ratio (μ) and the strength reduction as a percentage with all specimens in experiment. Here having a coefficient of correlation of R^2 = 0.9695. From Figure4,

$$E = -83\frac{t_{min}}{t_0} + 86.5 \qquad (3)$$

Where, E = Strength reduction as a percentage, t_{min}= Minimum thickness ratio and t_0 = Initial thickness.

By this equation strength reduction can be calculated with using easily measurable parameters through a quick and careful site investigation.

3.2 Experimental Analysis

First, analytical modeling of th e non-corroded specimen was done with above des cribed modeling and analytical features to understa nd the accuracy of the adopted procedure. The variation of bucking load vs. displacement is shown in Figure 5. From numerical analysis conducted for non-corroded specimen it was found that the analytical model results were almost same as the experimental results with having a negligible percentage error of 0.05% in buckling strength. So it can be concluded that the conducted numeral analysis is accurate and the developed analytical model is validated.

Then, all other experimentally successful specimens were modelled to find out variation of specimen compare to numerical values. Numerical and experimental buckling load variation of the specimens is shown in Figure 6 and the percentage difference between experimental and numerical buckling strength is almost less than the 5%. So it was revealed that a very good comparison of the strength variation can be obtained for all corrosion specimens for the proposed analytical model. Having a coefficient of correlation of R^2 = 0.99 indicate the accuracy and the possibility of numerical investigation method to predict the buckling strength of actual corroded specimens.

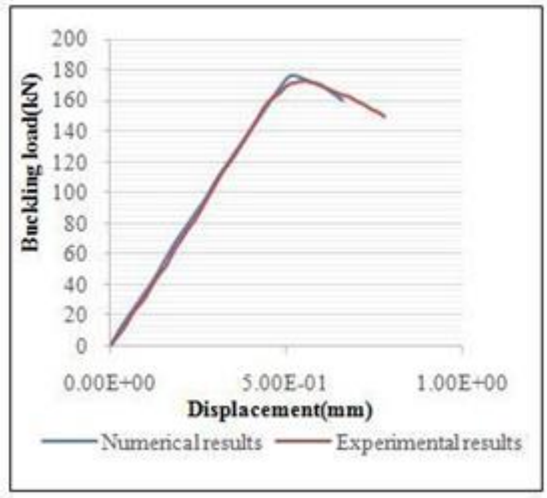

Figure 5: Load displacement variation of non corroded specimen

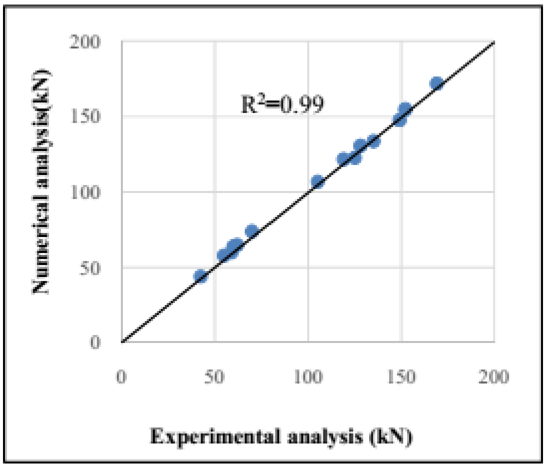

Figure 6: The graph of buckling load vs. Displacement for numerical and experimental

4. Results and Discussion

The residual strengths are decreased with the severity of corrosion and minimum thickness ratio (μ) can be used to for a quick estimation of their strength degradation. Equation obtained for strength reduction due to corrosion,

$$E = -83\frac{t_{min}}{t_0} + 86.5 \quad (4)$$

Where, E = Strength reduction as a percentage, t_{min}= Minimum thickness and t_0= Initial thickness.

Involved parameters of proposed equation are easily measurable and it will reduce the contribution of the errors occurred during the practical investigation of a corroded member. Further this method is simple and hence can be used for the maintenance management of steel bridge infrastructures with better accuracy. Strength reduction can be obtained as a percentage by substituting the minimum thickness of the corroded members in the structure to the above equation. So it will give clear idea about the stability of the member with compression. If the strength reduction percentage is not much higher value, then it can be used as a simple method to strengthen the structure. If the strength reduction of structures is higher, then structure cannot withstand for the load longer time.

Non-linear FEM Analytical results indicated a very good comparison of the experimental and the analytical load-elongation behaviours for all three classified corrosion types. So, it can be concluded that the adopted numerical modeling technique can be used to predict the remaining buckling strength capacities of actual corroded members accurately. So, it is evident that this numerical modelling procedure can be extended to establish a simple and accurate procedure to predict the remaining strength capacities of a corroded steel member by measuring lesser number of points with an acceptable accuracy level in future studies.

Acknowledgement

I thank everyone that who has supported during my research period.

References

[1]. Appuhamy, J. M. R. S., Kaita, T., Ohga, M., and Fujii, K.2011, 'Prediction of residual strength of corroded tensile steel plates',

International Journal of Steel Structures 11, pp 65–79.

[2]. Appuhamy, J.M.R.S., Ohga, M., Kaita, T. and Fujji K. 2010, 'Effect of Measuring Points on Remaining Strength Estimation of Corroded Steel Plates', Proceedings of the 9th Pacific Structural Steel Conference, China, pp. 1504-1516.

[3]. Mianus River Bridge - Wikipedia, the free encyclopedia, 2014. Available from: http://en.wikipedia.org/wiki/Mianus_River_ Bridge. [Available 10 June 2014].

[4]. Silver bridge – Wikipedia the free ancyclopedia, 2014. Available from: http://en.wikipedia.org/wiki/Silver_Bridge. [Available 10 June 2014]

SECM/25/156

Some Engineering Aspects of Ancient Structures

P.L.N. Fernando [1*] and W.P.S. Dias [2]

[1]Research Assistant, University of Moratuwa, Moratuwa, Sri Lanka
[2] Senior Professor, University of Moratuwa, Moratuwa, Sri Lanka *E-Mail: lakshitha_f@yahoo.com, TP: +94779744941

Abstract: Large monumental constructions were a prominent feature in ancient Sri Lanka. Construction materials and techniques used in the past can be of significant interest to the modern engineer. The evolution of brick sizes during four ancient periods of Sri Lanka spanning from 375 B.C to 1350 A.D. was studied by using recorded data of bricks found on ancient construction sites. The calculated ratios and the relationships indicate that the length was relatively significant in the reduction of the brick sizes while breadth and thickness changed roughly in proportion to the length at a lower rate. The effect of ground condition, i.e. rock, strong soil and weak soil; and the effect of pedestals on a solid hemispherical dome type Stupa were analysed using SAP2000. It was found that a stupa, if unrestrained along its horizontal directions, could experience tension being developed at the centre when built on a weak soil. Also, when constructed on poor ground conditions a pedestal reduces the compressive stresses at the base. However, the pedestal causes higher hoop and radial tensile stresses closer to the top and bottom of the outer surface of the dome. Vaulted structures in Sri Lanka exhibit approximately similar span to wall thickness ratios, thus indicating the possibility of the design being governed by the geometry of the structure. Also the development of stresses in vaulted structures indicates that the maximum vertical stress is compressive at the base, while the maximum tensile stress is at the crown intrados.

Keywords: Brick sizes, Foundation, Hoop stresses, Pedestals, Vaulted structures

1. Introduction

1.1 Brick Sizes

Bricks were the most commonly used construction material in ancient constructions. Its sizes have evolved over the years. The lengths, breadths & thicknesses and hence the volume and the cross sectional area have undergone changes over time, with length, breadth and thickness changing from 19.8” to 8.2”, 10.3” to 4.74” and 3.4” to 1.55” respectively. There are claims suggesting the possibility of categorizing bricks and thereby the structures constructed using them into certain historical periods, depending on their dimensions [1], i.e. pre-Christian and post-Christian (0-300AD, 300-800AD and 800-1350AD). As for the dimensions of a brick, it was widely believed that the breadth and thickness of a brick were simple fractions of its length [1]. The methods of manufacturing as well as the reason for using the bricks were key factors for its reduction in size [2]

1.2 Stupas

Ancient stupas in Sri Lanka were built using bricks and this was structurally feasible since the maximum stresses developed in the dome were well below the strength of ancient bricks [3]. Since seismic effects are not of significant concern in Sri Lanka, considering only its self-weight provides a reasonable basis for analysis of stupas [3]. As for the results of stress analysis, the maximum vertical stresses are compressive, while the maximum hoop stresses are tensile [3].

1.3 Vaulted Structures

Vaulted structures, which are not as common as stupas, but found in image houses since the Polonnaruwa period, were also built using bricks. The vaults found in Sri Lanka could be broadly categorized under three types, namely; brick corbelled vaults, brick circular vaults and brick corbelled and circular vaults [2]. The performance of such masonry structures is governed by stability and hence a geometrical factor of safety is probably of relevance [4].

2. Study on Brick Sizes

2.1 Objective

This research sought to identify trends and relationships associated with the changes the brick sizes have undergone, based on the available data [1] over the four historic periods of Sri Lanka.

2.2 Methodology

The parameters considered in the analysis were, length (L), breadth (B), thickness (T), cross sectional area (BT), volume (V), length to breadth ratio (L/B), length to thickness ratio (L/T) and breadth to thickness ratio (B/T). The variations of these parameters with each other were studied [5].

2.3 Results and Discussion

As indicated in Table 1, the B vs L and T vs L relationships suggest that the reduction of the length significantly influenced the reduction of the breadth and thickness through the ages. Even more significant is the dependence of volume on both length and cross sectional area. However, Figures 1 and 2 show that the L/B and L/T ratios were not constant with changes of length. In other words length decreased more rapidly with time than breadth or thickness. This was perhaps the most interesting finding of the study; one that is not alluded to by Parker [1].

Table 1: Regression Coefficients

Quantities	R^2 Values
B vs L	0.659
T vs L	0.603
V vs L	0.905
V vs BT	0.943

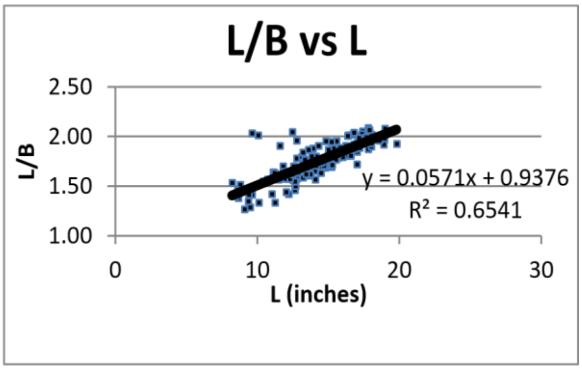

Figure 1: Variation of Length to Breadth ratio vs Length

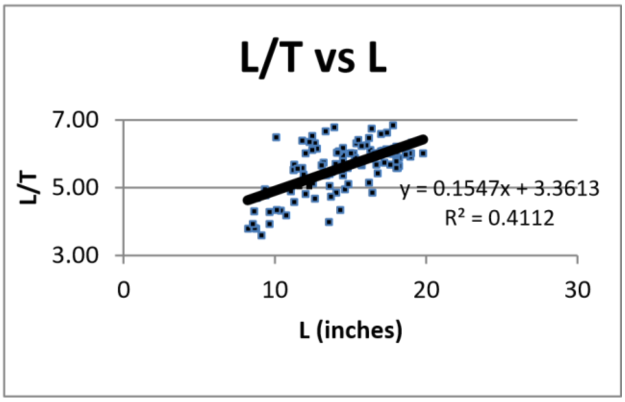

Figure 2: Variation of Length to Thickness ratio vs Length

3. Stupas

3.1 Objective

This component of the research identifies the effect of ground condition, i.e. rock, strong soil, and weak soil; and the effect of the pedestals on a solid hemispherical dome type Stupa. Although stupas were generally constructed from bedrock, modern construction of replicates may take place on less firm strata. The modelled Stupa was analysed using SAP2000 for the above cases to identify the nature and variation of vertical, radial and hoop stresses developed in the dome as well as the variation of the base pressure at the support level.

3.2 Methodology

The Stupa was modelled as a two dimensional axisymmetric structure, using the ASOLID element and then replicated to arrive at the final structure. The replicate angle as well as the material angle was taken as 8 degrees to ensure radial symmetry of the dome. Since it was the dome component that was of interest, the rest of the structure above it was modelled in such a way so that the geometric integrity of the structure remained intact. Furthermore, the dome was assumed to be hemispherical and hence, the actual height of Ruvanwelisaya [3] – a hemispherical stupa - was considered to be equal to the radius of the dome (i.e. 44 m). The stupa was meshed into squares of 3m x 3m and triangles at the curved edge, maintaining the aspect ratios within acceptable limits.

Springs were modelled to capture the effect of soil. The spring constants at supports were obtained by multiplying the modulus of subgrade reaction for the relevant ground condition by the tributary area of each support. Furthermore, to introduce coupling to the behaviour of the springs, the spring constant of the springs at the outer edge of the dome was doubled [6]. The moduli of subgrade reaction for rock, strong soil and weak soil were taken as 800,000 kN/m^3, 80,000 kN/m^3 and 8,000 kN/m^3 respectively.

Initially, the dome was analysed while restraining it only vertically, i.e., either fixed at supports or on springs only in the vertical direction. Next, to consider the friction effect of the soil, it was restrained in the two horizontal directions (radial and tangential), with the aforementioned restraint conditions for the vertical direction.

3.3 Results and Discussion

When unrestrained in the two horizontal directions, thus neglecting the frictional effect of the underlying soil, compressive stresses increase in radial, vertical and tangential directions as the ground conditions vary from rock to weak soil. Furthermore, zones of tensile stress move inwards from the outer surface of the dome to the centre for radial and hoop stresses and the numerical values of the stresses also increase (see Figure 3). This creates an undesirable situation, as tensile stresses in the centre could weaken the structure considerably.

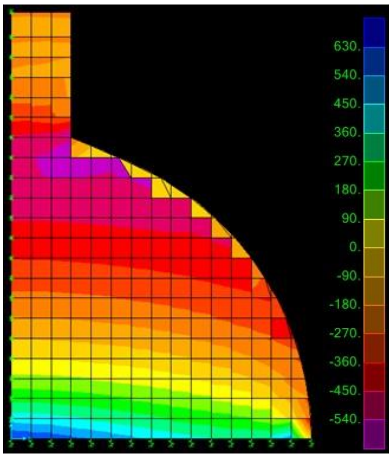

Figure 3: Hoop Stress Variation for Weak Soil Condition (Unrestrained in the Two Horizontal Directions)

However, for more realistic site conditions, the effect of the underlying soil friction should also be accounted for in the analysis. A frictional shear force equal to ($\tan\varphi$ x F_Z) + (c x Tributary area) will be applied by the soil. For this analysis, a friction angle (φ) of 26^{o}and a cohesion (c) of 0 kN/m^2 was used to represent the lower bound for a purely cohesionless soil; while a friction angle (φ) of 0^o and a cohesion (c) of 100 kN/m^2 used to represent the upper bound for a purely cohesive soil(Note: the actual adhesion between soil and foundation would be less than this as well).

The results for the first case indicated that the frictional shear force in the radial direction is greater than the reaction in that direction at each support joint. Therefore, this indicates that the surrounding soil prevents the movement of the structure in the radial direction. Hence, for a purely cohesionless soil, restraining the structure in the two horizontal directions at the support joints would provide a more accurate approximation of the actual state.

However, results for the second case indicated that the frictional shear force in the radial direction is less than the reaction in that direction, even in a very cohesive soil. Hence, stupas on purely cohesive soils may develop internal tension.

When restrained in the two horizontal directions, thus representing the true condition for most cases, tensile hoop stresses are greater than the tensile radial stresses. Maximum tensile radial stresses occur closer to the base, while there are two identifiable tensile zones for hoop stresses; one adjacent to the base and the other adjacent to the top (see Figure 4).

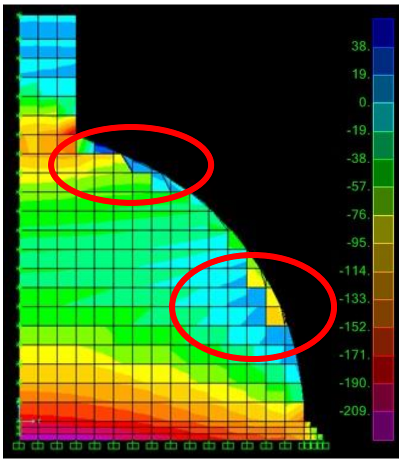

Figure 4: Hoop Stress Variation for Fixed Base Condition (Restrained in the Two Horizontal Directions)

As illustrated in Figure 5, as the foundation condition weakens the maximum hoop tensile stress at the zone closer to the top increases regardless of the presence of the pedestal. However, the stresses with the pedestals are marginally higher than when without pedestals. This may just be because of the additional load from the pedestal.

As far as base pressure is concerned, for the fixed base case, as illustrated in Figure 6, the relatively higher stresses for the case with the pedestals could be due to the added weight of the pedestals. The increase in pressure at the outer edge may be due to the modelling technique of doubling the end spring stiffness. Apart from that, the pressures decrease from centre to edge, somewhat reflecting the weight of the brickwork directly above each point.

However, as illustrated in Figure 7, when on weak soil, once again apart from the outer edge, the pressures from centre to edge are very uniform. This may be because stupas on weak soils display more arch action, creating greater pressure close to the edges and matching those at the centre due to the loads from greater brick heights. Also, the gap between the two lines is much less compared to the earlier case.

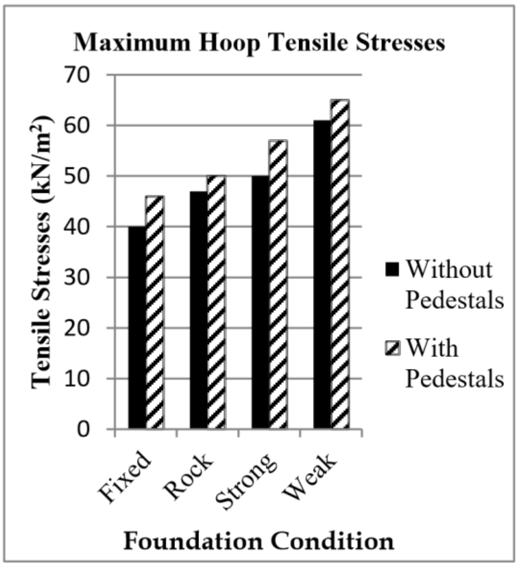

Figure 5: Maximum Hoop Tensile Stresses for Different Foundation Conditions

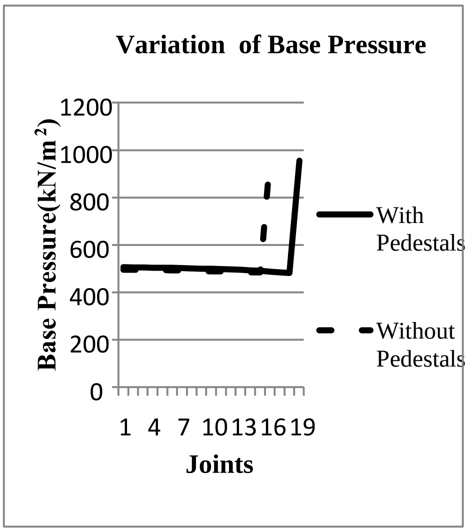

Figure 7: Variation of Base Pressure for Weak Soil Condition

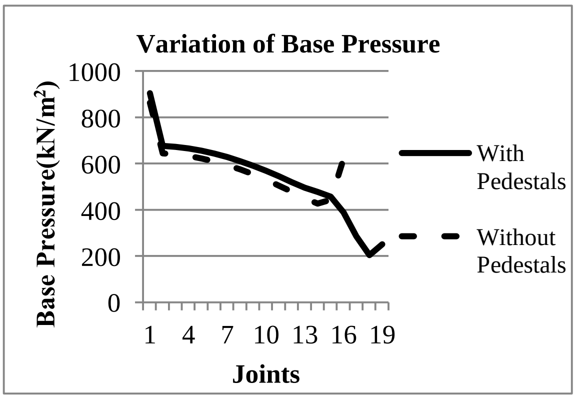

Figure 6: Variation of Base Pressure for Fixed Base Condition

4 Vaulted Structures

4.1 Objective

Since the geometry of the structure is considered critical in arches and vaulted structures, this research looks to identify combinations of spans and wall thicknesses of existing vaulted structures in Sri Lanka. In addition, these were modelled using SAP 2000 to identify the nature and variation of the vertical and horizontal stresses throughout the vault and the variation of the base pressure at the support levels.

4.2 Methodology

The brick masonry vaulted structures at the Thivanka Image House and the Thuparama Image House were considered for the analysis. The dimensions of the former were obtained from the drawings at the Polonnaruwa Branch of the Central Cultural Fund, while the dimensions of the latter were measured at site due to the absence of prerecorded data (see Figures 8 and 9).

A cross section of the vault was modelled in SAP2000, using a plane stress element with 1 m thickness. The structure was meshed into squares, trapeziums and triangles while maintaining the aspect ratios within acceptable limits. Since the drawings for the Thivanka Image House indicated that the structure was placed on a rock foundation at a depth of 1m from the ground level, the support conditions were assigned as fixed.

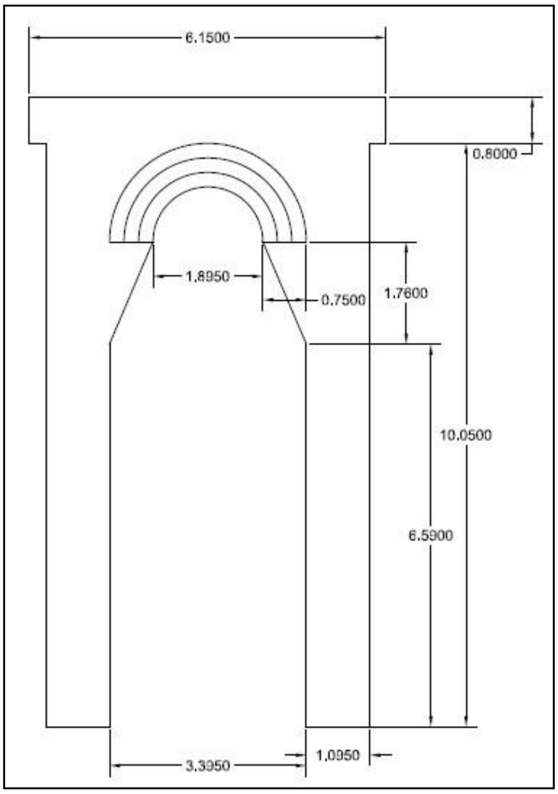

Figure 8: Dimensions of Thivanaka Image House (in meters)

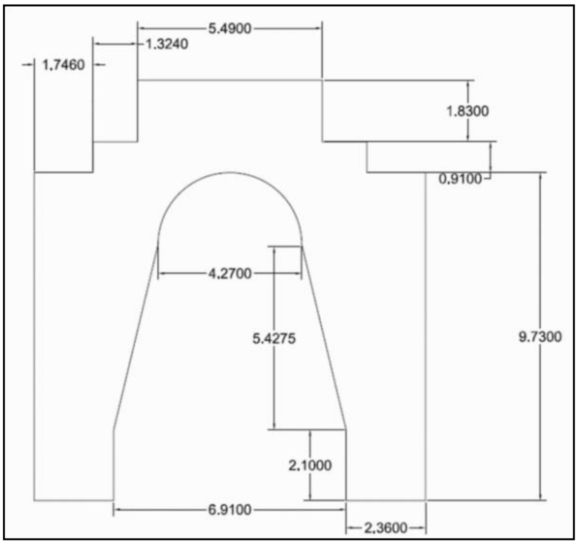

Figure 9: Dimensions of Thuparama Image House (in meters**)**

4.3 Results and Discussion

Table 2 indicates the span to wall thickness ratios that were observed. The two values for the Thivanka image house are from two areas, in the larger one of which only the springings of the arch are visible. The ratios are virtually identical and close to 3, suggesting that it could have been a geometrical design rule.

Table 2: Geometrical Relationships of Thivanka and Thuparama Image Houses

Location	Span (m)	Wall thickness (m)	Span/ Wall thickness ratio
Thivanka-1	3.4	1.12	3.04
Thivanka-2	7.96	3	2.65
Thuparama	6.91	2.3	3.00

As far as stresses are concerned, the maximum tensile stresses in both vertical and horizontal directions occur at the crown intrados of the vault. This could be attributed to the deformed shape under the self-weight of the structure. Furthermore, a small principal tensile stress is developed throughout the entire structure due to the relative magnitudes and directions of the vertical and horizontal stresses.

As for compressive stresses, the higher values at the base would be due to the effect of the selfweight. The horizontal restraint causes the vertical compressive stresses to increase when moving outwards from the structure intrados at base level (Figure 10); but there is an opposite trend at intermediate levels. The deformed shape from the modelling in ref. [5] gives the impression of arch walls bulging outwards due to vertical load, but restrained along the base.

Furthermore, maximum vertical stresses are compressive at the base, while the maximum tensile stresses are at the crown intrados (Figure 11).

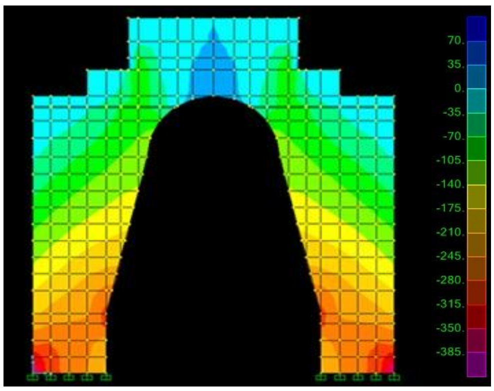

Figure 10: Variation of Vertical Stress in the Thuparama Image House

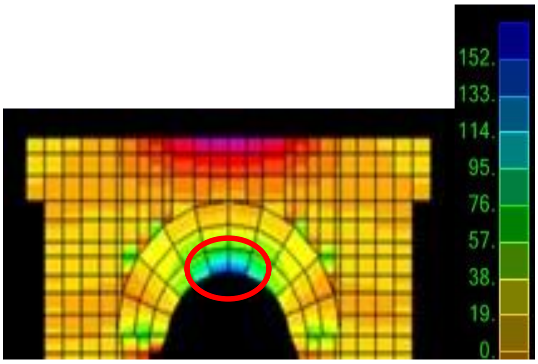

Figure 11: Tensile Zone Due to Horizontal Stresses in the Vault

Table 3: Comparison of Compressive and Tensile Stresses in Stupa and Vaulted Structures

`	Vertical Compressive Stress at Base(kN/m^2)		Maximum Tensile Stress(kN/m^2)		
	Maximum	Range	Value	Direction	Location
Stupa	675	98-675	46	Hoop	Surface
Vault 1	340	207-340	147	Horizontal	Crown, intrados
Vault 2	395	205-395	25.5	Horizontal	Crown, intrados

As indicated in Table 3, the compressive stresses induced in the stupa (fixed base) are much greater than that of the vaulted structures. The much larger self-weight of the Stupa would be the reason for this. Furthermore, the range of variation of compressive stress for the stupa is much greater when compared to the vaults. This could be due to the shape and hence the variation of the mass in the dome of the Stupa.

Table 3 also shows that two distinct vaulted structures with significant variations in dimension, yield somewhat similar variations in stresses, perhaps because they had approximately similar span to wall thickness ratios.

Furthermore, both compressive and tensile stresses are within the strength limits of modern brick work which are around 1.5 N/mm^2 and 0.2 N/mm^2 respectively [7]. However, the likelihood of a tensile failure is greater in the vault.

5. Conclusions

5.1 Brick Sizes

Although reduction of the length significantly influenced the reduction of the breadth and thickness through the ages, length decreased more rapidly with time than breadth or thickness.

5.2 Stupas

The properties of the sub soil, the friction angle and the cohesion in particular, is of significant interest, in designing and constructing a stupa, because a lower frictional shear force could induce undesirable tensile stresses at the centre, when constructed on weak soil.

Stupas on weak soils have more uniform pressure distributions under their bases, while those on rock would have higher pressures at the centre.

The effects of varying ground conditions are much more significant than the variation between a stupa with and without a pedestal.

5.3 Vaulted Structures

Approximately similar span to wall thickness ratios for differing vault spans suggest that a geometrical guideline may have been used in their design. This is confirmed by the fact that two distinct vaulted structures with significant variations in dimension, yield similar variations in stresses for approximately similar span to wall thickness ratios.

Vertical stresses are maximum and compressive at the base, while tensile stresses are maximum at the crown intrados.

Compared to the stupa, the compressive stresses in the vaults are smaller. Compressive and tensile stresses for both the stupa and vaults are less than the characteristic strengths of modern brickwork; however, the likelihood of a tensile failure is greater in the vault.

Acknowledgement

The authors wish to acknowledge the assistance given by the Central Cultural Fund of Sri Lanka and the non-academic staff of University of Moratuwa.

References

[1]. Parker, H., Ancient Ceylon:An Account of the Aborigines and of Part of the Early Civilization.: London: Luzac and Co,
Publishes to the India office, 1909.

[2]. Silva, R., "Men and Monuments: D.T. Devanada: A centennial Tribute," in Central Cultural Fund Sri Lanka, p. 14., 2001.

[3]. Ranaweera, M.P., Dissanayake, D.M.C.J. ,"A Comparative Study of Stresses in Domes of Ancient Stupas of Different Shapes Under Self Weight," in Society of Strutural Engineers, Sri Lanka-Annual Sessions 2011, p. 8., 2011.

[4]. Heyman, J.,The Stone Skeleton: Structural Engineering of Masonry Architecture.: Cambridge University Press, 1995.

[5]. Fernando, P.L.N., Engineering Aspects of Ancient Structures, BscEng. Dissertation, University of Moratuwa,2015.

[6]. Bowles, J.E., Foundation Analysis and Design, McGraw-Hill International
Editions,1988.

[7]. Jayasinghe, M.T.R., Loadbearing brickwork construction for Sri Lanka. Colombo, Sri Lanka: STRAD Consultants (Pvt) Ltd, 1997.

SECM/15/051

Life evaluation of critical members of steel bridges located in different atmospheres

W.T.M.S.M. Wanninayake[1], W.M.P.R. Wasala[1] and C.S. Bandara[1*]

[1]University of Peradeniya, Peradeniya, Sri Lanka
*E-Mail: bandara@civil.pdn.ac.lk, TP: +94 77 540 0273

Abstract: Most of the iron and steel bridges in Sri Lanka are more than 100 years old. Since many of them are reaching or exceeding their design lives, the risk of collapsing those bridges have increased. One of the probable damages which bridges experience due to increasing traffic volume as well as environmental degradations such as corrosion is the corrosion fatigue failure. This problem is severe in bridges located in industrial areas and along the coastal line of the country. Corrosion and corrosion fatigue made a huge attention in the recent past due to many failures of bridges all over the world.

This paper presents a study conducted on assessing the corrosion fatigue damage of steel bridges. It proposes a procedure developed using existing fatigue and corrosion models for evaluating the remaining fatigue life. The procedure includes condition surveys, field loading tests, finite element modelling and analysis, developing S-N curves for different atmospheric conditions, use of corrosion rates and assessing cumulative fatigue damage. The paper also presents a case study: a century old iron and steel (mild steel and wrought iron) railway truss bridge damaged by both corrosion and fatigue. Using details of condition survey, load testing, appropriate corrosion data, finite element modelling and a corrosion fatigue assessment procedure, the remaining life of the bridge was evaluated for two atmospheric conditions; (i) corrosive atmosphere and (ii) noncorrosive atmosphere. The results of the evaluation were then compared to show the impact of the atmospheric condition on the fatigue life of the bridge.

Keywords: metal fatigue, corrosion, steel bridge, damage assessment, life evaluation

1. Introduction

Sri Lanka has large number of railway and roadway steel and iron bridges that are rapidly aging and are in continuous need for regular inspection, monitoring and maintenance. Damage assessment plays a vital role in this. One of the main components of an effective structural damage assessment is determining the remaining fatigue life of the structure.

Corrosion is considered to be an influential factor that significantly contributes to the reduction of the fatigue life. Corrosion process is highly accelerated in marine-industrial regions where chlorides and sulphates are regularly available [1,2]. Laboratory fatigue testing is the most accurate method for determining the fatigue life of materials. The drawbacks are that such tests are costly, time consuming and interpreting lab test data for real structures is difficult [3].

The “stress-life (S-N)” method is the most used fatigue damage assessment method [4]. This method uses the alternating stress amplitude (σ_a) to predict the number of cycles to failure (N). The S-N curve (stress amplitude versus fatigue life curve) that comprises the influence of material, geometry and surface condition is the tool used in S-N method. The S-N curve for a material can be developed using experimental tests. However due to the difficulty of conducting experiments, empirical and analytical formulae are available for developing material specific S-N curves. The S-N method is generally used for high cycle fatigue (HCF) where the stresses are low and material response is mostly elastic that is observed in steel bridges subject to usual service loading [5].

The reduction of thickness of metal elements due to corrosion is another problem that needs the attention. It is known that the corrosion is mainly depends on the atmospheric conditions. ISO 9223 [6] classifies the atmospheric corrosivity using; (i) pollutants and the time of wetness (TOW) and (ii) corrosivity rates, and points out five corrosivity categories. These corrosivity categories (numbered from C1 to C5 from low to high corrosivity) represent rural, urban, industrial and marine environments [7]. There are various methods and models developed to predict the rate of reduction of thickness subject to atmospheric corrosion [8,9]. Some of these models are based on the quantities of pollutants in the atmosphere and TOW while some are based on measured rate of reduction of thickness in different atmospheric conditions. These methods and models are very helpful analytical / empirical tools for assessing the corrosion damage up to a reasonable accuracy.

Accurate corrosion fatigue damage assessment of a structure needs a procedure that is developed combining the findings of corrosion fatigue and atmospheric / environmental conditions. Present paper attempts to propose an accurate procedure for assessing the corrosion fatigue damage of existing steel structures.

2 Hypotheses

The main cause of failure due to corrosion fatigue is broadly divided into two: (i) Reduction in thickness that increases the stress in the remaining part of the material and (ii) Roughening of the surface and pitting that act as stress raisers due to which cracks initiate earlier and, weakening of the material due to micro-structural changes caused by the combined effects of corrosion and cyclic loading. Therefore, to assess the corrosion fatigue damage of a structure the damages of both these causes should be taken into account.

2.1 Prediction of reduction of thickness

Corrosion rates of steels are largely different from one atmosphere to the other. Using corrosivity categories of ISO 9223 [6] with different atmospheres, the corrosion rates of carbon steel for the first year of exposure are in the range, rural: 0.0 - 1.3 μm/a, urban: 1.3 - 25 μm/a, marine: 25 - 80 μm/a and industrial: 80 - 200 μm/a [7]. Studies also show that the rate of corrosion decreases with time. Four years experimental data for carbon steel shows that the percentages of the average corrosion rates at the 2nd and 4th years with respect to the 1st year are 63% and 42% respectively. Further, the study of corrosion rate of carbon steel in seawater shows that the average corrosion rate after the 5th and 20th year are 70 and 50 μ/m [10,11]. Akesson [12] has mentioned that the corrosion rates of riveted bridges (wrought iron and mild steel) located in industrial areas is about 50 μm/a and in the inland part of the country (Switzerland) is less than 5 μm/a. Pitting (localized corrosion) is usually observed in structures exposed to the atmosphere due to the effects of the non-uniformity of material, environmental and corrosivity conditions [1,10]. The pitting factor is the ratio between the deepest metal penetration and the average metal penetration due to corrosion. Studies show that the pitting factor for steels (without mill-scale) is in the range 2 – 3 [10]. Accordingly, four methods can be suggested to obtain the rate of thickness reduction; (i) measuring the thickness reduction rate experimentally, (ii) measuring the pollutant levels and TOW first and then determining the rate using ISO 9223 or any other empirical methods, (iii) calculating an average rate by measuring the actual thickness of existing structures in which original thickness is known and (iv) using available data of previous studies. In the present study, the method (iii) was used to obtain the average thickness reduction rate of the structure.

2.2 S-N curve for corrosion fatigue

Mathematical functions have played a major role in developing S-N curves. In this study, a simplified corrosion fatigue S-N model that was developed using Palmgren function was used as the basic tool for the fatigue life evaluation [13,14,15].

The well accepted fact on the impact of corrosion on the fatigue damage is that corrosion reduces the fatigue life of metallic materials [12,16,17]. Therefore, in the S-N approach based fatigue assessment, the effect of corrosion should be included in the S-N curve. Accordingly, the corrosion based S-N model [17] used in the present study is given in Eq. (1),

$$\sigma(N)_{corr} = \sigma(N) - d \cdot log(N) \qquad (1)$$

where, $d = \frac{(\sigma_{VHCF} - \sigma_{corr})}{log(N_{VHCF})}$., $\sigma(N)$ and $\sigma(N)_{corr}$ are the stress amplitudes required for the fatigue failure of the element at N cycles in non-corrosive and corrosive atmospheres respectively, N_{VHCF} is the number of cycles concerned in the very high cycle fatigue (VHCF) region (> 10^7 cycles) and σ_{VHCF} is the fatigue strength amplitude in the VHCF region.

2.3 Stress range and mean stress correction

The S-N curve obtained in Eq. (1) is the standard curve for constant amplitude zero mean stress condition (stress ratio $R = -1$). However, in bridges, the stress amplitudes are neither constant amplitude nor zero mean stress. Therefore, stress ranges are calculated using the reservoir (or rein-flow) counting method and mean stress correction is carried out using modified Goodman method [17, 18] given in Eq. (2),

$$\sigma_a = \sigma_{ar}\left(1 - \frac{\sigma_m}{\sigma_u}\right) \quad (2)$$

where, σ_{ar} is the corrected stress amplitude, σ_a is the stress amplitude, σ_m is the mean stress and σ_u is the ultimate tensile strength.

2.4 Damage accumulation method

Stress ranges applied on a bridge varies during its service life (variable amplitude loading). The objective of using a damage accumulation method is to obtain the cumulative damage caused by each and every stress range. Though there are many methods available for estimating the cumulative fatigue damage, due to its simplicity, the most used Palmgren - Miner rule [4] was used in the present study. According to Palmgren - Miner rule, the cumulative damage D_i caused by n_i numbers of cycles of stress amplitude σ_i is given in Eq. (3),

$$\sum_1^n D_i = \sum_1^n \frac{n_i}{N_i} \quad (3)$$

where, N_i is the number of cycles to failure at the stress amplitude σ_i. The failure occurs when $\sum_1^n D_i \geq 1$.

2.5 Damage assessment procedure

Combining methods and techniques described in sections 2.1 – 2.4, the procedure proposed for assessing the cumulative fatigue damage of a steel structure in non-corrosive and corrosive atmospheres is given below (Figures 1 and 2).

Step 1: Measure dimensions of the bridge on-site, conduct a condition survey and field loading tests; Model the bridge (with measured thicknesses) using finite element methods (FEM), validate the model using measurements obtained from field loading test; Identify the critical members of the bridge based on stress levels and cycles; Prepare detailed FEMs of these critical members to obtain stress concentration factors SCF.

Step 2: Determine past and future loading details of the bridge (for railway bridges using railway time tables and for road bridges using traffic survey data). This detail should include the type of the vehicle, weight, number of wheels and wheel spacing etc.

Step 3: Use the validated FEM to obtain the influence lines of each critical element for all vehicle types; Using these influence lines, determine the primary force ranges (reservoir counting) and number of cycles n_i for these critical members.

Step 4a: For structures with no corrosion: Calculate the primary stress ranges ($\Delta\sigma_{p,i}$) using force range and original thickness; Then calculate the effective stress ranges at critical location (using SCF) with mean stress correction $\Delta\sigma_{e,i}$; Prepare histograms of $\Delta\sigma_{e,i}$ and n_i.

Step 4b: For structures with corrosion: Divide the past life and future life of the structures in to several intervals (say 10 year intervals); predict the actual thicknesses at each interval based on the corrosion rate; Calculate the primary stress ranges ($\Delta\sigma_{p,i}$) using force range and predicted thickness for all the time intervals; Calculate the effective stress ranges at critical location (using SCF) with mean stress correction $\Delta\sigma_{e,i}$; Prepare histograms of $\Delta\sigma_{e,i}$ and n_i.

Step 5a: For structures with no corrosion: Develop the material specific S-N curve of steels with no corrosion; Obtain N_i values for each and every $\Delta\sigma_{e,i}$.

Step 5b: For structures with corrosion: Develop the material specific S-N curve of steels with corrosion; Obtain N_i values for each and every $\Delta\sigma_{e,i}$.

Step 5: Use Palmgren – Miner damage accumulation rule or any other method to calculate the cumulative fatigue damage and the future life.

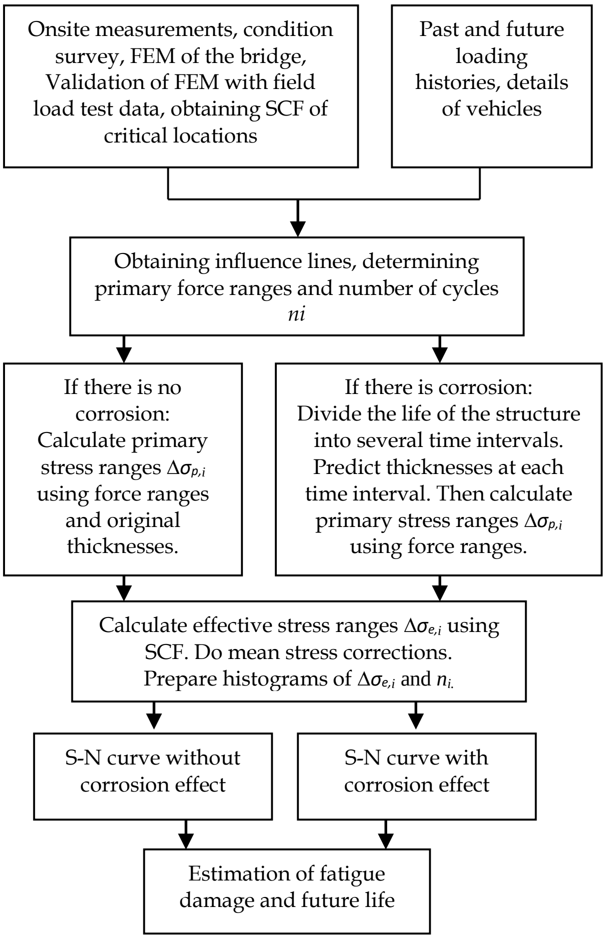

Figure 1: Damage assessment procedure

3. Case study

A century old iron and steel (mild steel and wrought iron) railway truss bridge damaged by both corrosion and fatigue was used for the case study. The bridge is a semi through truss Girder Bridge (Figure 2). The span and height of a truss is 32.25 m and 3.20 m respectively. The bridge is 5.35 m wide and caries a single rail track of gauge 1.74 m. Century old trusses of the bridge are wrought iron while some of the cross girders that were changed in 1980s are mild steel.

Figure 2: A view of the steel truss bridge

3.1 Onsite measurements

Condition survey and field loading test were first carried out. Two engines of mass 66 tons each were used for field loading test. Static loading was done by placing the engine on the bridge at several positions while dynamic loading was done when the engines are moving with different speeds. Electronic data measurements were obtained using strain gauges, acceleration gauges and displacement gauges.

In order to obtain the properties of materials used in the bridge, onsite non-destructive hardness testing was carried out using a portable tester. Later, material samples received from the bridge owner were tested at the laboratory. Table 1 gives the mechanical properties of wrought iron and mild steel.

Table 1: Mechanical properties of steels

Steel	σ_u (N/mm^2)	*Hv* (kgf/mm^2)	σ_y (N/mm^2)	*El* %
Wrought iron (WI)	343	104	230	18
Mild steel (MS)	426	120	249	37

(*Hv* is the Vickers hardness, σ_y is the yield strength and *El%* is the percentage elongation at brake)

3.2 Finite element models

Based on the detailed structural drawings prepared from field measurements, a three dimensional FEM for the whole bridge (Figure 3) was developed. Material properties obtained from laboratory testing were used in FEMs as required. The elastic modulus used was 205 GPa and Poisson's ratio used was 0.3. Loading test measurements (deflection, strain and acceleration) were used to validate the FEM. Suitable adjustments at support and joints were carried out to improve the performance of the model. Few detailed FEMs were also developed for critical members in order to observe the stress pattern and to obtain stress concentration factors (Figure 4).

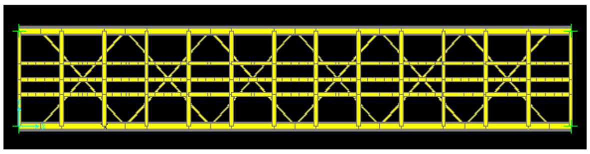

Plan viwe of the bridge showing bottom chord, cross girders, stringres, bottom bracing and the rail track.

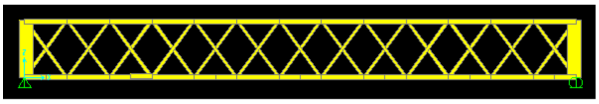

Sectionl viwe showing dioganal members, top and bottom chord and end box.

Figure 3: FEM of the bridge

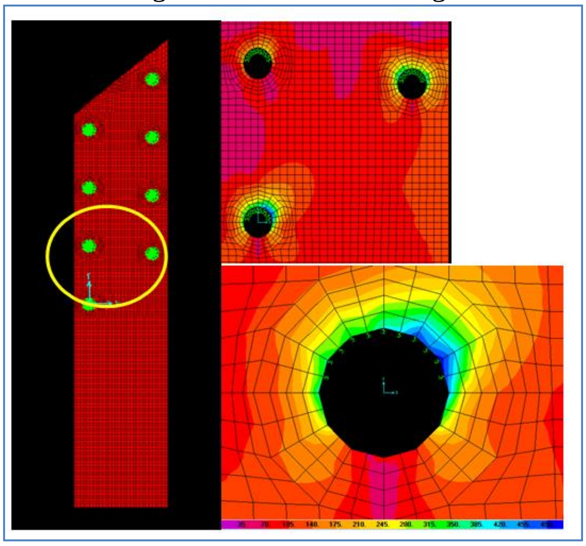

Figure 4: FEM of a critical connection

3.2 Full range S-N curves

Full range S-N curves for wrought iron and mild steel were developed for corrosive and non-corrosive conditions using the S-N models described in Section 2. As the S-N models produce the mean curves which has a 50% probability of failure (probability of survival Ps = 50%), 90% probability of survival (Ps = 90%) curves were developed for fatigue damage assessments [13,17]. The uniform scatter of stress (Tσ) for metals was estimated by using Eq. (4),

$$T\sigma = 1 : [\Delta\sigma(Ps=10\%)/\Delta\sigma(Ps=90\%)] \qquad (4)$$

Figures 5 and 6 show the S-N curves for wrought iron and mild steel developed for non-corrosive and corrosive atmospheres.

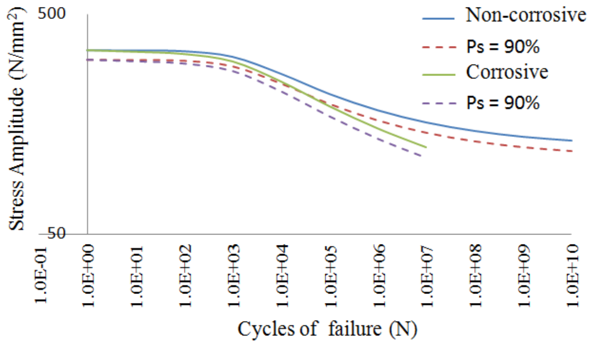

Figure 5: S-N curve for wrought iron

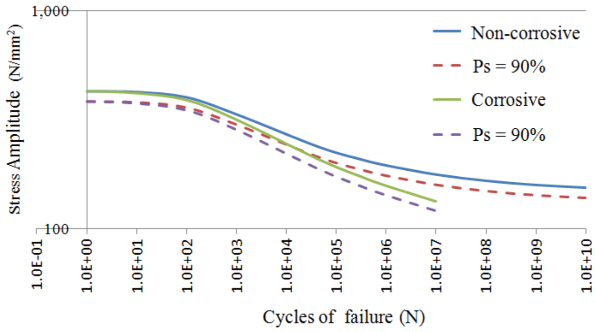

Figure 6: S-N curve for mild steel

3.3 Cumulative fatigue damage assessment

As described in Section 2.5 the critical members of the bridge were identified from the validated FEM of the bridge. The detailed FEMs of these critical members were then developed in order to obtain the stress concentration factors. Train timetables were used to obtain the past and future loading of the bridge. Thickness reduction due to corrosion was found by onsite thickness measurements and then the thickness reduction rate was estimated. Using influence lines of forces in critical elements and stress concentration factors obtained from FEMs, and modified Goodman method the effective stress ranges were calculated. Then, using the S-N curves developed, the fatigue damage with and without corrosion effect was estimated. Palmgren – Miner damage accumulation rule was used to find the cumulative fatigue damage.

3.4 Results

When considering the cumulative fatigue damage of one of the critical members: diagonal member 1, the total life for non-corrosive atmosphere was 180 years whereas that in corrosive atmosphere was 60 years. In the actual structure, some of the diagonal members are in damaged state. Some of the members have been replaced using mild steel, i.e., main girders. Therefore the wrought iron members may not survive up to 180 years. However, there were no observable fatigue cracks in the diagonal member 1 to verify the life of 60 years. One possibility is that the members may have deformed (failed) and the loading may have been distributed among other diagonal members. The other possibility is that the predictions of the procedure proposed may be conservative. Therefore, further research may be required to verify or improve the procedure proposed.

4. Discussion and conclusions

Corrosion fatigue damage assessment of steel structures needs research as there are no successful methods available. In the present study, an attempt was made to propose an assessment procedure that comprised different validated techniques. The advantage of using the procedure proposed is it uses a material specific S-N curve that represents the material behaviour and corrosion rates that represents the atmospheric conditions. The separation of (i) reduction in thickness that increases the stress in the remaining part of the material and (ii) micro-structural and surface changes of the material weakening the fatigue strength has made the proposed model simple. Even the method used for developing S-N curves for corrosive atmospheric conditions does not require expensive fatigue testing that makes the procedure simpler.

The conclusions of the study are as follows.

Existing theories and assessment methods can be used together with FEMs to assess the corrosion fatigue damage.

The fatigue damage of structural elements in corrosive atmosphere is considerably higher than the damage when they are in non-corrosive atmosphere.

FEM shows that the stress concentration factor of riveted connections increase with the reduction of the plate thickness due to corrosion.

Case study conducted using an iron and steel bridge showed that the procedure proposed is reasonable than the usual method. However, it may produce conservative results. Therefore, further studies are needed to verify or improve the procedure.

Acknowledgement

Department of Civil Engineering, University of Peradeniya, the Open University, Nawala and Ceylon Government Railway (CGR), Colombo.

References

[1] Roberg, P. R. 2000. Handbook of corrosion engineering, 1st Ed., McGraw Hill, New York.

[2] Revie, R. W., Uhlig, H.H. 2008. Corrosion and corrosion control. 4th ed. John Willy, New Jersey.

[3] Cui, W. 2002. A state of the art review on fatigue life prediction methods for metal structures, Journal of Material Science & Technology. Vol. 07, pp. 43-56.

[4] EN 1993-1-9. 2005. Design of steel structures: Part 1-9:Fatigue, CEN, Brussels.

[5] Rathnayake, R. M. S. U. P., and Dissanayake, P. B. R. 2011. Methodology for condition assessment and retrofitting of railway bridges, Proceedings of the 4th International Conference on Structural Engineering and Construction Management, Kandy, Dec 12-14, 2011.

[6] ISO 9223. 1992. Corrosion of metals and alloys – corrosivity of atmospheres – classification, ISO, Geneva.

[7] Roberge P. R. 2011. Atmospheric Corrosion, Uhligs corrosion handbook, Ed. Revie R. W. 3rd ed. John Willy, New York.

[8] El Aghoury I. 2012. Numerical tool for fatigue life prediction of corroded steel riveted connections using various damage models, PhD Thesis, Concordia university, Montreal.

[9] Hoeppner, D. W., Chandrasekaran, V., and Taylor, A. M. H. 1999. Review of pitting corrosion fatigue models, Proceedings of ICAF International Conference, Seattle.

[10] Matsushima, I. 2011. Carbon steel corrosion by sea water, Uhligs corrosion handbook, Ed. Revie R. W. 3rd ed. John Willy, New York.

[11] Tidblad, J., Kucera, V., Hicks, K., Kuylenstierna, J., et al. 2009. Atmospheric corrosion effects of air pollution of materials and cultural property in Asia and Africa. 17th International Corrosion Congress, NACE intl., Texas, 2009.

[12] Akesson, B. 2010. Fatigue life of riveted steel bridges. CRC press, London.

[13] Bandara, C. S., Siriwardane, S. C., Dissanayake, U. I., and Dissanayake, R. 2015. Developing a full range S-N curve and estimating cumulative fatigue damage of steel elements, Computational Materials Science, Vol. 96, pp. 96-101.

[14] Bandara, C. S., Siriwardane, S. C., Dissanayake, U. I., and Dissanayake, R. 2014. Fatigue failure predictions for steels in the very high cycle region – A review and recommendations, Engineering Failure Analysis, Vol. 45, pp. 421 – 435.

[15] Bandara, C. S., Siriwardane, S. C., Dissanayake, U. I., and Dissanayake, R. 2015. Full range S-N curve for fatigue life evaluation of steels using hardness measurements, International Journal of Fatigue, Vol. 82, pp. 325 – 331.

[16] Wang Y. Z. 2011. Corrosion fatigue, Uhligs corrosion handbook, Ed. Revie R. W. 3rd ed. John Willy, New York.

[17] C. Bandara. 2015. Fatigue damage assessment of steel structures and components, 1st ed. LAP Lambert Academic Publishing, Deutschland.

[18] Suresh S. 1991. Fatigue of materials. 1st ed. Cambridge: Cambridge university press, Cambridge.

SECM/15/089

Fatigue capacity of cold-formed steel roof battens under cyclic wind uplift loads

M. Kathekeyan[1] and M. Mahendran[1]

[1]Queensland University of Technology, Brisbane, Australia
E-Mail: myuran.kathekeyan@hdr.qut.edu.au, TP: +61 45075 4006
E-Mail: m.mahendran@qut.edu.au, TP: +61 73138 2543

Abstract: Steel roofs made of thin cold-formed steel roof claddings and battens are widely used in low-rise residential and industrial buildings all around the world. However, they suffer from premature localised pull-through failures in the batten to rafter connections during high wind events. A recent study proposed a suitable design equation for the pull-through failures of thin steel roof battens. However, it was limited to static wind uplift loading. In contrast, most cyclone/storm events produce cyclic wind uplift forces on roofs for a significantly long period, thus causing premature fatigue pull-through failures at lower loads. Therefore, a series of constant amplitude cyclic load tests was conducted on small and full scale roof panels made of a commonly used industrial roof batten to develop their S-N curves. A series of multi-level cyclic tests, including the recently introduced low-high-low (LHL) fatigue loading test, was also undertaken to simulate a design cyclone. Using the S-N curves, the static pull-through design capacity equation was modified to include the effects of fatigue. Applicability of Miner's rule was evaluated in order to predict the fatigue damage caused by multi-level cyclic tests such as the LHL test, and suitable modifications were made. The combined use of the modified Miner's law and the S-N curve of roof battens will allow a conservative estimation of the fatigue design capacity of roof battens without conducting the LHL tests simulating a design cyclone. This paper presents the details of this study, and the results.

Keywords: Cold-formed steel structures, Steel roofing systems, Thin steel roof battens, Wind action, Pull-through failures, Fatigue, Miner's rule

1. Introduction

Roofs made of thin and high strength cold-formed steel (CFS) claddings and battens are commonly used in low to medium-rise building construction. Such steel roof members are vulnerable to fatigue failures under high and fluctuating suction wind pressures. Particularly, low-pitched roofs of low to medium-rise buildings are subjected to high suction pressures and thus premature roof failures in high wind events, namely cyclones and storms.

Roofing assemblies comprise of claddings, battens/ purlin, rafter/ truss and their connections as shown in Figure 1. Generally, steel batten is a multi-span secondary structural member, spanning between roof trusses or rafters. The uplift wind pressure on roof claddings is transferred to the battens first through the cladding to batten connection, and then to rafter/truss via batten to rafter/truss connection. Finally, it is transferred to column and then to foundation as shown in Figure **1**.

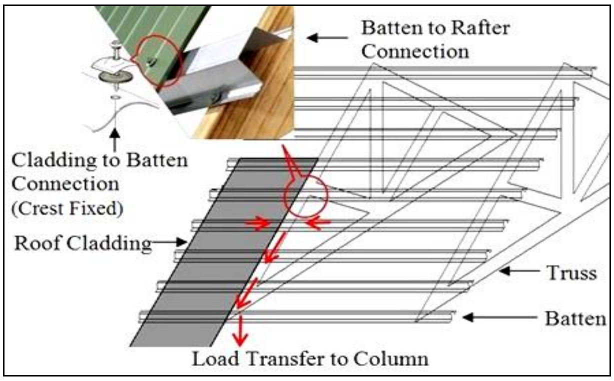

Figure 1: Typical roof structures and load path

Past cyclone damage studies have shown that roofs have mostly failed due to connection failures than member failures. They revealed that the cladding to batten and the batten to rafter screw connections shown in Figure 2 are the weakest links in the load transfer path. These connections can fail in two localised failure modes, namely static or fatigue failure depending on the wind event. Among them, the fatigue failure caused by cyclic loading is more critical as the fatigue failure capacity is about 40-50% of the static failure capacity [1].

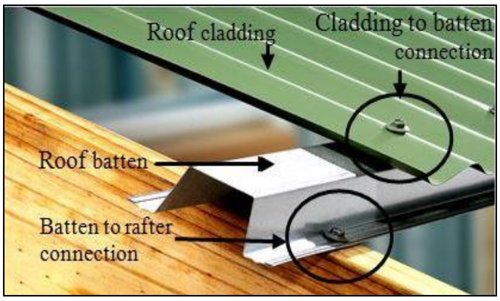

Figure 2: Critical roof connections

CFS roof members are susceptible to two types of local failures, namely, pull-through (Figure 3) and pull-out (Figure **4**) failures. A screw fastener head pulling through the cladding or batten under severe wind uplift pressure on the roof is referred to as pull-through failures whilst the same pulling out from the supporting member is referred to as pull-out failures. Therefore, a roof assembly can fail in one of the following four different failure modes during high wind events.

1. Pull-through and Pull-out failures of roof cladding to batten connection
2. Pull-through and Pull-out failures of roof batten to rafter connection

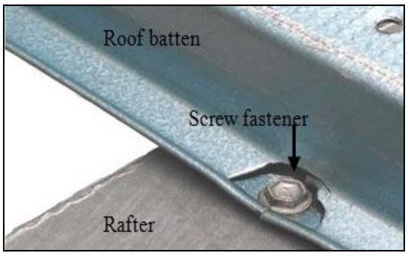

Figure 3: Pull-through failure of the batten to rafter connection

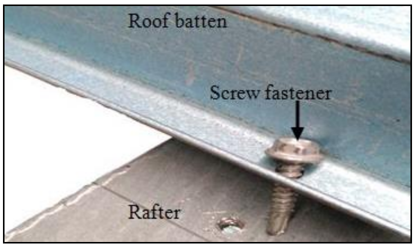

Figure 4: Pull-out failure of the batten to rafter connection

Many past studies have investigated all the possible failures associated with the cladding to batten connections, and improved the knowledge of this connection capacity under both static and cyclic wind effects. Such improvements made the batten to rafter connection the weakest connection in the roof assembly. A recent study investigated the static pull-through capacity of roof batten to rafter connections, and proposed suitable equations to predict the static pull-through capacity. However, the critical fatigue pull-through failure of roof batten to rafter connections has not been investigated. Therefore, this study investigates the fatigue pull-through failure of roof battens.

The failure at a connection progressively increases the loads on the adjacent fasteners, and leads to a complete collapse of building roofs. Therefore, a good knowledge of the fatigue behaviour and capacity of roof battens is essential. It can be achieved through the fatigue resistance curve (S-N curve in the form of stress/load level versus number of cycles to failure) obtained from constant amplitude cyclic tests. Such a S-N curve was obtained for an industrial roof batten through a series of constant amplitude cyclic tests. The batten and test assembly used were chosen to simulate real roofs in cyclone prone areas.

During cyclones, the amplitude of the cyclic wind uplift forces on the roof members is not constant. In order to include the varying amplitudes and the exposure period of roof members in a cyclone, a standard test method known as Low-High-Low (LHL) test was introduced. Such multi-level cyclic tests were also included in this study. Using constant amplitude and multi-level cyclic tests of roof battens, this study has investigated the fatigue pull-through capacity of roof battens when exposed to high wind events. This paper presents the details of this experimental study and the results.

2. Current Design and Test Methods

The Australian [3] and American standards [4] provides design formulae to calculate the pull-through capacity of mechanically fastened screw connections in tension. The design static pull-through capacity (ϕN_{ov}) based on [3] is as follows:

$$\phi N_{ov} = \phi\, 1.5\ t\ d\ f_u \qquad \text{for } 0.5 < t < 1.5 \text{ mm} \qquad (1)$$

Where, t is the thickness of the sheet in contact with the screw head, d is the greater of the screw head and the washer diameter (8 < d < 12.5 mm) and f_u is the specified ultimate tensile strength. It recommends the use of lesser of 90% of f_u for G550 steel sheet or 495 MPa for steel $0.6 < t < 0.9$ mm in thickness, and ϕ is the capacity reduction factor = 0.5. However, the applicability of Eq.1 to roof battens is questionable. Sivapathasundaram and Mahendran [5] showed that the pull-through capacities calculated form Equation (1) are much higher than the experimental results, ie. unsafe. The American cold-formed steel specification [4] also gives the same equation and is therefore not applicable to thin CFS battens.

Sivapathasundaram [6] developed the following design equations to predict the static pull-through capacity of roof battens. These equations predicted the pull-through capacities of roof battens used in their experimental study. However, they have not included the effects of cyclic wind loading in their equations.

For G550 steel roof battens:

$$F_{ov} = 8.68 t^2 f_u \tag{2}$$

and

For G300 steel roof battens:

$$F_{ov} = 2.96 t^{1.39} d^{0.61} f_u \tag{3}$$

European standard for CFS members and sheeting [7] recommends an equation to determine the fatigue pull-through capacity. The design pull-through capacity for screw connections subjected to cyclic wind loading is defined as follows:

Fatigue pull-through capacity = 0.5 x Static pull-through capacity (4)

Design static pull-through capacity
= $t \times d \times f_u / \gamma_m$ (5)

Where, γ_m is the partial factor = 1.25, and others have been defined under Eq.1.

However, the design pull-through capacity of a 0.75 mm Grade 550 steel (ultimate tensile strength f_u is 700 MPa) batten fastened by 10 gauge screw fasteners (d = 11 mm) calculated from Equation (5) was 4.62kN, ie. 37% higher than the average static pull-through capacity (3.38 kN) of the batten tested by Sivapathasundaram and Mahendran [5]. Therefore both the static and fatigue capacity equations are not suitable to determine the pull-through capacity of thin CFS battens.

Due to the lack of design fatigue pull-through capacity equations, the current design practice is mainly based on laboratory experiments using a fatigue loading sequence known as Low-High-Low (LHL) pressure sequence [8]. This simulates the sustained fluctuating wind loading in a design cyclone using seven blocks of loading applied at a frequency less than 3 Hz (Table 1), where P_t is the ultimate limit state wind pressure on a roof due to the combined external and internal wind pressures.

Table 1: Low-High-Low pressure sequence [8]

Sequence	Number of cycles	Cyclic loads
A	4500	0 to 0.45 P_t
B	600	0 to 0.6 P_t
C	80	0 to 0.8 P_t
D	1	0 to 1.0 P_t
E	80	0 to 0.8 P_t
F	600	0 to 0.6 P_t
G	4500	0 to 0.45 P_t

3. Experimental Study

This experimental study consists of two phases. The first phase consists of constant amplitude cyclic tests, which included full scale roof tests followed by a series of small scale batten tests. The second phase consists of multi-level cyclic tests including LHL tests. A commonly used industrial roof batten and 10 gauge screw fasteners were used in these tests. It is made of 0.75 mm base metal thickness (BMT) G550 steel (minimum yield stress of 550 MPa) with 40mm height (
Figure **5**).

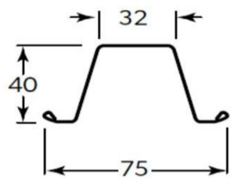

Figure 5: Test batten

3.1 Full Scale Tests

For research and test purposes, a two-span batten assembly is considered a satisfactory representation of multi-span batten assemblies used in buildings [9]. Therefore, a two-span roof batten assembly was chosen in the tests to simulate the fastener loads and the bending moment in the battens at the critical central support. 2.4 m x 1.5 m two-span roof panels were made using 0.48 mm BMT corrugated steel roof cladding, roof battens shown in Figure 5 and "C" purlins as shown in

Figure **6**.

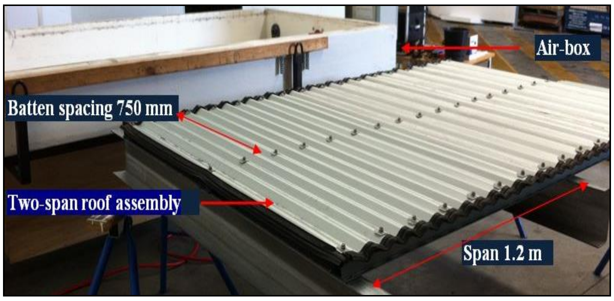

Figure 6: Full scale two-span roof assembly

Roof claddings were alternate crest fixed with battens using 6.5x55 self-drilling roofing screws with cyclone washers. 10 gauge self-drilling metal Tek screw fasteners were used to fix the battens to "C" purlins. Cyclone washers and roofing screws were selected to prevent local failures in the cladding to batten connections. In order to prevent the pull-out failures in the batten to rafter connections, Unbrako bolts and nuts were used instead of the 10g metal Tek screws in the critical central support of the middle batten, where the reaction force is the highest. A specially made screw head washer (head of 10g Tek screw) was used along with Unbrako bolts to simulate the metal Tek screw at the failure location (
Figure **7**). A constant torque 2.5N/m was used to install the bolt connections with lock nuts to prevent nut loosening during the cyclic tests.

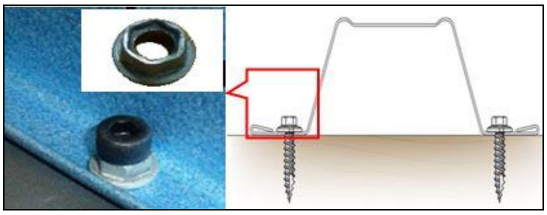

Figure 7: Simulated screw head washer

The roof panels were then tested in an air-box (
Figure **8**), where a wind suction pressure was simulated using a 7 kPa air pump and a controller. As seen in
Figure **8** the roof panels were placed upside down on top of the air-box. A special rubber seal was fixed around the roof panel to prevent air leak. Initially, three static tests were conducted. The suction pressure was slowly increased at a rate less than 15 N/s until complete pull-through failure occurred. The fastener loads were measured using 15 kN washer load cells (K-180) (
Figure **9**) to determine the static pull-through capacity.

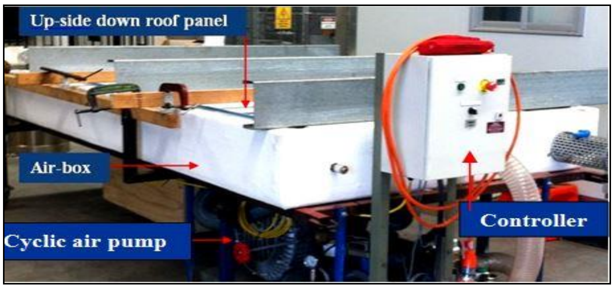

Figure 8: Full scale air-box test

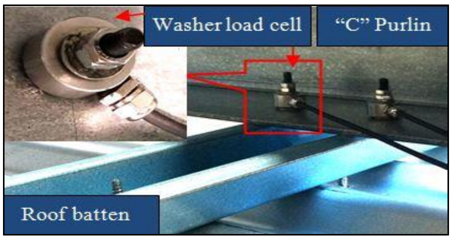

Figure 9: Washer load cells

A series of constant amplitude cyclic load tests was then conducted for different percentages of the measured static pull-through failure capacity to obtain the fatigue life (number of cycles to failure) of the roof batten. The air pump was controlled by a special air control valve to apply a sine wave form suction pressure on the roof test panels at a frequency of 1 Hz. The fastener tension load was measured using the washer load cells and the required cyclic pressures of each test were obtained by adjusting the air pressure based on the load cell reading.

3.2 Small Scale Tests

A series of small scale tests was included in this study to reduce the required number of full scale tests. Therefore, three different small scale battens (short, cantilever and two-span battens) were used to investigate the fatigue behaviour of roof battens. Figures 10 to 12 show the short, cantilever and two-span battens, respectively.

Among the small scale tests, initially a series of 150 mm long short batten tests (Figure 10) was conducted on a 100 kN MTS machine as was done for static pull-through capacity tests [5]. Although the batten's bending action was not simulated, it was included here to investigate the suitability of the previously used short batten tests and to investigate the effect of the absence of bending action on fatigue pull-through failures. Static and cyclic loads were applied by the MTS hydraulic actuator at the top flange of the batten until complete pull-through failure occurred. The static loading rate was 1mm/min while cyclic tests were conducted using force control at a frequency of 1 Hz.

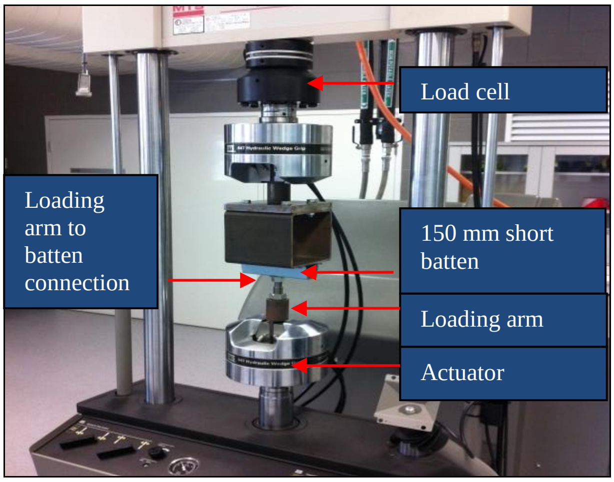

Figure 10: Short batten test

Secondly, a series of cantilever batten tests (Figure 11) was conducted by simulating both fastener tension load and bending moment in the batten. A 550 mm long cantilever batten (cantilever length of 240 mm) was used in this test series. The cantilever length was selected using simple bending theory to simulate the bending moment of the full scale roof assembly. Loading arm was bolted with the batten 240 mm away on either side of the connection as shown in Figure 11.

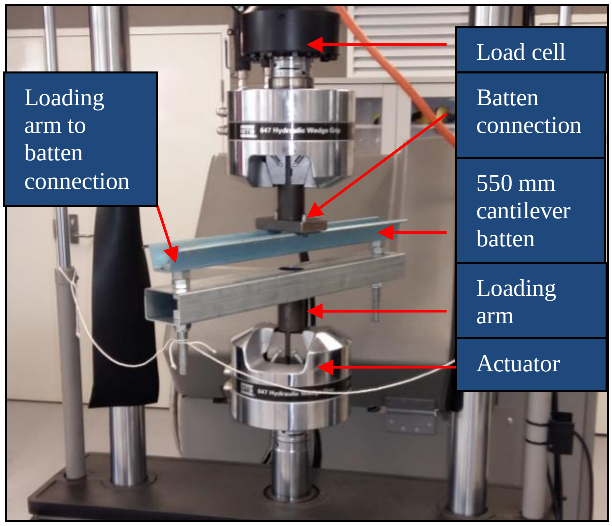

Figure 11: Cantilever batten test

Finally, a series of two-span batten tests was conducted on a 1900mm long batten (span of 900 mm) using a 500 kN hydraulic actuator (Figure 12). This test not only simulates the fastener tension load and the bending moment in the batten at the central support, but also the actual support conditions. The loading arm was bolted to the batten at its mid-span points. Batten span was calculated using simple bending theory to maintain the same fastener tension and bending moment in the batten at the central support of full scale panels. In these tests, the cyclic loads were applied as a sine wave at 1 Hz, and the number of cycles to failure was recorded. The load transferred to the critical central support connection (failure location) was measured using washer load cells.

In the cantilever and short batten tests, the load during the test was measured by the MTS load cell. However, in the air-box and two-span batten tests, two small washer load cells were used at the batten's central support, as shown in Figures 9 and 12, to measure the individual fastener reactions.

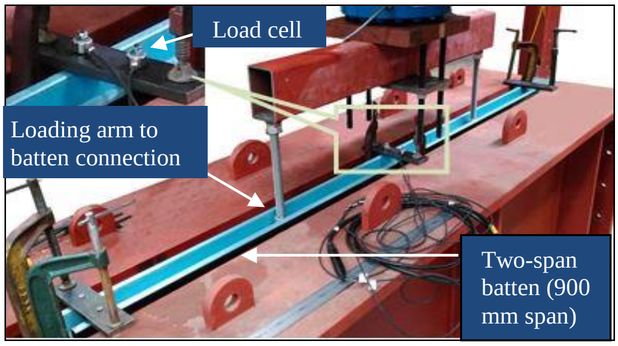

Figure 12: Small scale two-span batten test

3.3 Multi-level Cyclic Tests

The small scale two-span batten test method was used to conduct the multi-level cyclic tests with the same 1900 mm long two-span batten (span of 900 mm) and 10g screw fasteners to find the fatigue capacity of roof battens exposed to design cyclones, and to investigate the applicability of Miner's law. Cyclic tests of two-span battens were conducted at seven different percentages of P_t as required of the LHL test sequence (Table 1) [8]. The single load cycle D (Table 1) was held for 10 seconds at the ultimate design wind pressure, P_t [8]. Test was discontinued when the pull-through failure occurred.

4. Test Results and Comparison

4.1 Constant Amplitude Cyclic Tests

In order to produce the fatigue resistance curve (S-N curve) of the roof batten, static tests were first conducted using all the full scale and small scale tests, and their results are listed in Table 2. Figure 13 shows the average load per fastener versus displacement curve of the two-span batten test. The load increased up to a peak value (static pull-through capacity), which was mostly achieved when a tearing was initiated. After this, the load decreased until a complete pull-through failure occurred. The air-box tests were conducted in force control at a rate of 15 N/sec while all other tests were conducted in displacement control at a rate of 1mm/minute.

Table 2: Static pull-through capacity of roof batten

Test type	Static Capacity (kN)	Mean	COV
Air-box	3.06, 3.09, 3.61	3.25	0.10
Short batten	2.79, 2.94, 2.96, 3.01	2.93	0.03
Cantilever batten	2.76, 2.71, 2.93, 2.98	2.85	0.05
Two-span batten	3.00, 3.10, 3.12	3.07	0.02

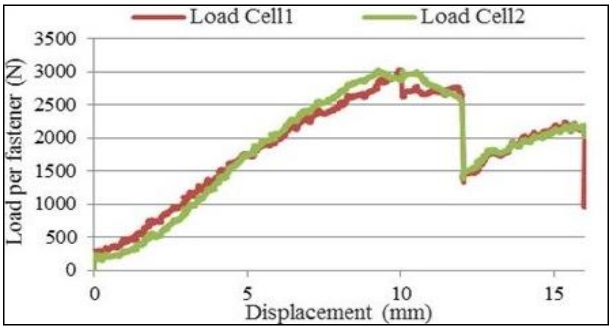

Figure 13: Average load per fastener versus displacement curves: two-span batten test

As seen in Table 2, the static pull-through failure capacities of roof battens obtained from short, cantilever and two-span batten tests agree reasonably well with the capacity obtained from the full scale air-box test. It should be noted that the air-box test was conducted in force control method, which generally gives a higher capacity compared to that obtained from displacement control tests. Also, a higher variation (COV = 0.1) was noticed in the large-scale tests due to the complex test arrangements. Due to the above reasons and as the variation between large and small scale tests are comparatively negligible, it can be concluded that all the small scale test methods can be used to obtain the static pull-through capacity of the roof battens. However, their applicability for the fatigue pull-through study is unknown. Therefore, constant amplitude cyclic load tests were conducted for a load range from zero to various percentages of the static pull-through capacity using all the test methods.

The number of cycles at crack initiation (N_i) as well as the number of cycles at the complete pull-through failure (N_f) were obtained and are listed in Table 3 to 6. In order to obtain N_i, displacement of the batten to rafter connection with respect to the loading point was recorded during the cyclic test. Such a displacement versus fatigue life graph is given in Figure 14. This graph can be divided into two segments, ie. up to the first notable peak (4500 cycles) followed by increasing displacement. In the first case, the displacement versus fatigue life graph is almost constant. From the first notable peak, where crack initiation occurred, the displacement increased in a manner as stable crack growth occurred. The two notable changes in the displacement indicate the crack initiation on the two sides of the batten. This pattern was noted in the majority of cyclic tests. Using this, cycles to crack initiation, N_i, were recorded in all the small scale tests, and are listed in Tables 4 to 6.

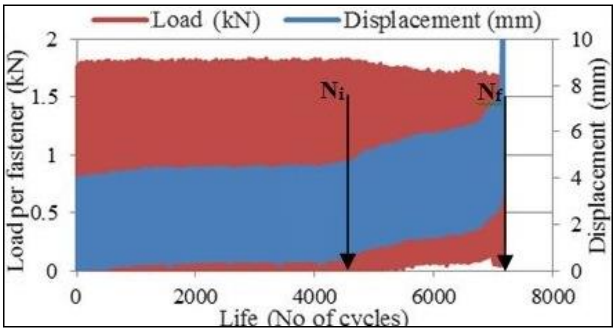

Figure 14: Force and displacement versus fatigue life graph of 56% cyclic test of two-span batten

Table 3: Constant amplitude cyclic test results - Full scale air-box tests

Applied load per fastener (kN)	Cyclic load (% of static pull-through load)	Number of cycles to failure
3.25	100	635
2.50	77	4753
2.20	68	3041
1.85	57	13100
1.60	49	21280
1.50	46	19581
1.50	46	19692
1.30	40	37781

Table 4: Constant amplitude cyclic test results - Two-span batten tests

Applied load per fastener (kN)	Cyclic load (% of static pull-through load)	Number of cycles to failure	
		N_i	N_f
3.07	100	1	308
2.73	89	1900	2400
2.39	78	2100	3000
2.05	67	3500	5372
1.71	56	4500	7162
1.54	50	5500	12290
1.26	41	26000	41617

Table 5: Constant amplitude cyclic test results - Cantilever batten tests

Applied load per fastener (kN)	Cyclic load (% of static pull-through load)	Number of cycles to failure	
		N_i	N_f
1.95	68.4	3100	5179
1.65	57.9	4400	6641
1.50	52.6	5400	13909
1.35	47.4	10000	20866
1.05	36.8	34000	47107

Table 6: Constant amplitude cyclic test results - Short batten tests

Applied load per fastener (kN)	Cyclic load (% of static pull-through load)	Number of cycles to failure	
		N_i	N_f
1.95	66.6	3200	6633
1.65	56.3	4800	11153
1.35	46.1	7500	28745

Constant amplitude cyclic test results were plotted as a S-N curve of cyclic pull-through failure load (percentage of static pull-through failure load) versus fatigue life (number of cycles to failure), and are presented in Figure 15. The S-N curves obtained from all the small scale tests agreed reasonably well with the S-N curve of the roof batten obtained from full scale air-box tests. This indicates that all the small scale tests can be used to study the fatigue behaviour of roof battens.

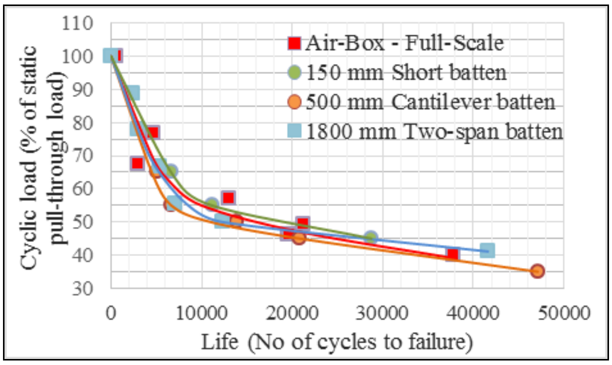

Figure 15: S-N curves of full scale and small scale tests for complete pull-through failure

Similarly, S-N curves for crack initiation, N_i, from all the small scale tests were compared as shown in Figure 16, which agreed perfectly well. As can be seen in Figures 15 and 16, both S-N curves clearly illustrate the reduction in fatigue life with increasing cyclic load levels. Also, it can be seen that below about 50 to 60% of the static pull-through capacity, fatigue life increment rate increases significantly. This indicates the presence of a fatigue limit in the range of 40 to 50% of the static pull-through failure load.

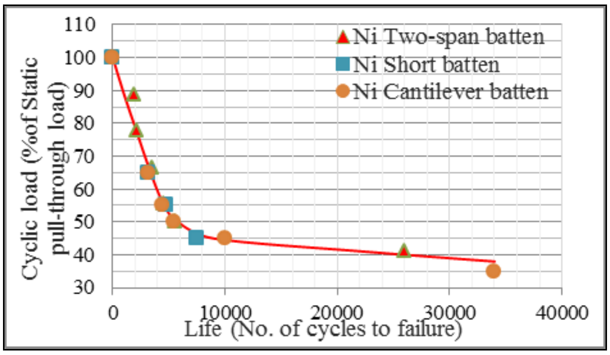

Figure 16: S-N curves of small scale tests for crack initiation

According to Figures 15 and 16, for a cyclic load closer to 40% of the static pull-through failure load, the roof batten will survive more than 25,000 cycles. However, in general, a house exposed to a cyclone will not experience such large numbers of cyclic loading. The LHL loading sequence [8] consists of about 10,000 cycles to represent a design cyclonic loading on a building roof. Therefore, by considering the damage caused by 10,000 cycles, a conservative fatigue limit of 45% of the static pull-through failure load can be proposed. However, it must be noted that real cyclonic loading is not constant amplitude cyclic loading. Therefore further guidance is needed.

Although all the small scale test results appear to agree reasonably well with the full scale test results, it is necessary to select the most suitable small scale test method for the fatigue study of roof battens. For this purpose, S-N curves obtained from each small scale test were compared with each other and full scale air-box tests. A good agreement between small scale two-span batten and full scale test results (Figure 17) reveal that the two-span batten test method can be used satisfactorily to simulate the full scale cyclic tests in the fatigue pull-through study of roof battens.

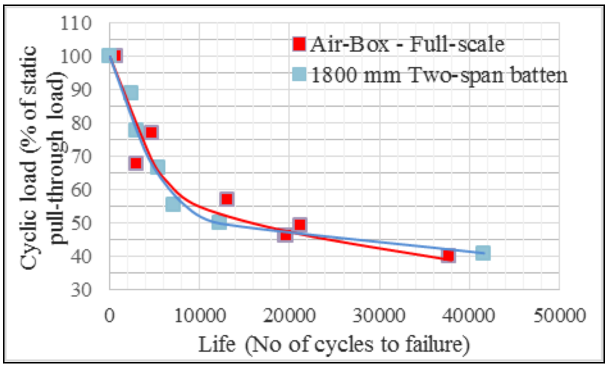

Figure 17: S-N curves of air-box and two-span batten tests for complete pull-through failure

Fatigue life (number of cycles to failure) from the cantilever batten test is always less than that obtained from the full scale test (Figure 18). This is because of the variation in the load at the critical failure connection (central support). The load applied to the batten to rafter connection in the cantilever batten test was constant throughout the test as shown in Figure 19, whilst the load in the critical central support connection in the air-box test reduced with fatigue damage as the load was transferred to the end supports with accumulated fatigue damage and associated changes to the connection fixity. This reflects the real case, i.e. load at the batten to rafter connections in roof varies with fatigue cracking during high wind events. This can only be simulated in two or more span batten tests. Therefore, small scale two-span batten test is the most suitable method for the fatigue study of roof battens.

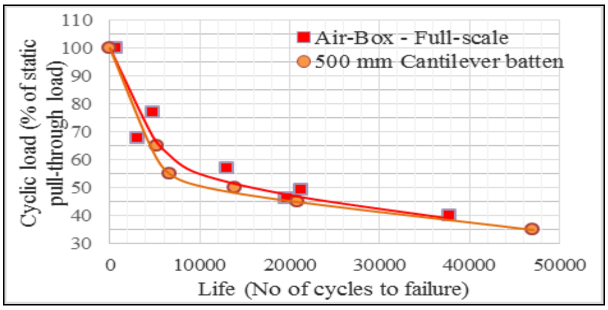

Figure 18: S-N curves of air-box and cantilever batten tests for complete pull-through failure

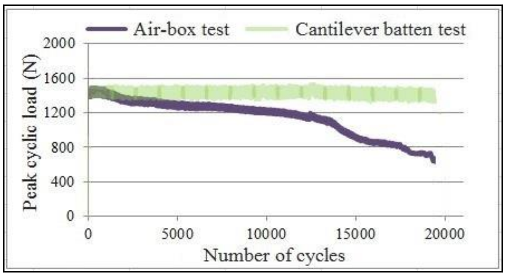

Figure 19: Peak cyclic load per fastener variation at the failure connection during cyclic loading

Although the short and cantilever batten tests do not simulate the actual condition, they can be compared to study the effect of bending due to two reasons: the load applied to the critical connection does not vary with fatigue damage, hence the fastener loads in these two tests are constant and equal; both tests used the same MTS machine, hence any machine error can be ignored. Therefore, S-N curves from these two test methods were compared as shown in Figure 20.

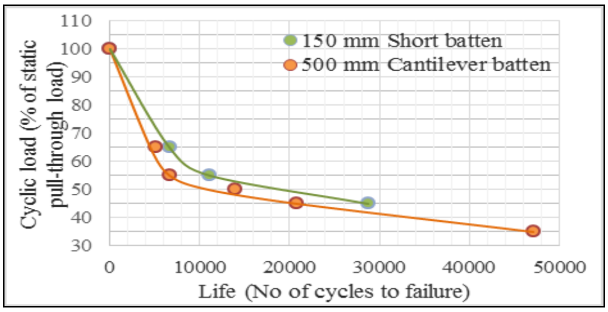

Figure 20: S-N curves of short and cantilever batten tests for complete pull-through failure

Table 7: Comparison of short and cantilever batten test results

Load applied per fastener (kN)	Cyclic load (% of static pull-through load)	Life (No of cycles to failure)		Variation %
		Cantilever batten test	Short batten test	
1.95	65	5179	6633	28
1.65	55	6641	11153	83
1.35	45	20866	28745	38

It shows a better fatigue performance in short batten tests compared to cantilever batten tests (Table 7). However, on the contrary, N_i obtained from these two tests agreed well. Figure 21 shows the comparison of N_i and N_f from these two test methods. It shows that the moment in the batten does not influence crack initiation; but it influences crack propagation. In other words, fastener tension load only influences the crack initiation, but both moment and fastener tension load at the critical support influence the crack growth and thus the complete pull-through failure, ie. the bending action influences N_f but not N_i. It must be noted that the variation between the fatigue life of the air-box and short batten tests is negligible as shown in Figure 15 as the S-N curve of the full scale air-box test is located between the S-N curves of short and cantilever batten tests.

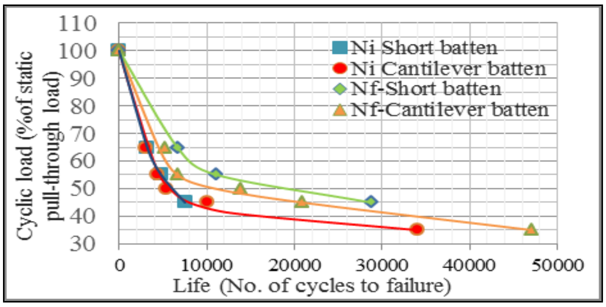

Figure 21: S-N curves of short and cantilever batten tests for crack initiation and complete pull-through failure

4.2 Multi-level Cyclic Tests

Table 8 lists the details of the multi-level cyclic tests of two-span battens conducted in this study and the results.

Table 8: Multi-level cyclic tests and the results

Test No	Pt (kN)	Pt*	Cyclic load sequences (% of P_t)			Cyclic load sequences *			No of cycles at each load sequence		
			A	B	C	A	B	C	A	B	C
T-1	3.07	100	70	80	70	70	80	70	1000	1500	1028
T-2	3.38	110	45	60	80	49.5	66	88	4500	600	295
T-3	3.53	115	45	60	80	51.8	69	92	4500	600	55
T-4	3.68	120	45	60	80	54	72	96	4500	600	80
T-5	4.45	145	45	60	--	65.3	87	--	4500	360	--

*- % of static pull-through failure load

Table 9: Fatigue damage calculated using the basic Miner's rule for Multi-level cyclic tests

Test No	Pt *	Cyclic load *	N applied	N_f failure	N_i failure	Damage-N_f	Damage-N_i
T-1	100	70	1000	4200	2850	1.03	1.49
		80	1500	2700	1900		
		70	1028	4200	2850		
T-2	110	49.5	4500	13600	6000	0.63	1.20
		66	600	5100	3300		
		88	295	1600	1100		
T-3	115	51.8	4500	10400	5200	0.62	1.14
		69	600	4400	3000		
		92	55	1100	700		
T-4	120	54	4500	9000	4700	0.81	1.41
		72	600	3900	2700		
		96	80	500	350		
T-5	145	65.3	4500	5200	3300	1.07	1.66
		87	360	1800	1200		
		--	0	0			

*- % of static pull-through failure load

The fatigue damage with respect to the complete pull-through failure was initially calculated using the basic Miner's rule as shown next.

$$F_t = \sum_{a=1}^{m} F_a = \sum_{a=1}^{m} \frac{n_a}{(N_f)_a} = 1 \qquad (6)$$

where F_t – Total fatigue damage, a ($1 \le a \le m$) – particular stress amplitude loading sequence, m - total number of various stress amplitude loading, F_a - fatigue damage for a particular stress loading, a, n_a - number of cycles applied in particular stress loading, a, and $(N_f)_a$ - total number of cycles to failure in the particular stress loading, a. Total number of cycles to failure, $(N_f)_a$, was obtained from the developed S-N curve (Figures 15 and 16) and the damage was calculated using Equation (6) for both crack initiation and complete pull-through failure. Table 9 presents the details and the damage results. Ideally, the calculated fatigue damage should be equal to one for a fatigue failure. However, it was less than one in some cases (T-2 to T-4), and are thus under-estimating the fatigue pull-through failure load. In contrast, the fatigue damage calculated for crack initiation is always greater than one. These results reveal that the basic Miner's rule does not always predict the fatigue damage accurately. Therefore, a modified Miner's rule for the total fatigue damage *(F_t)* is proposed as equal to the sum of damage up to crack initiation *(F_i)* and during crack propagation *(F_p)*.

$$F_t = F_i + F_p \qquad (7)$$

For a roof batten subjected to m number of various stress amplitude loading, a ($1 \le a \le m$), Equation 7 can be expanded as shown in Equations (8) to (10) for a crack initiation that occurred at xth stress amplitude loading, a=x, after y number of cycles.

$$F_t = \sum_{a=1}^{x+m} F_a = \sum_{a=1}^{x} F_a + \sum_{a=x}^{x+m} F_a = 1 \qquad (8)$$

$$\sum_{a=1}^{x} F_a = \frac{(N_{fi})_x}{(N_{ff})_x} \qquad (9)$$

$$\sum_{a=x}^{x+m} F_a = \frac{n_x - y}{(N_{ff})_x} + \sum_{a=x+1}^{m} \frac{n_a}{(N_{ff})_a} \qquad (10)$$

where,

N_{fi} and N_{ff} – Number of cycles to crack initiation and complete pull-through failure in a constant amplitude cyclic test at a given load level

n – Number of cycles applied at a given load level

In order to predict the fatigue damage using the modified Miner's rule, stress amplitude (x)

corresponds to crack initiation, $a=x$, and the number of cycles to crack initiation (y) at the xth load level, $n_x=y$, has to be found first. This can be achieved using Equation (11). The number of cycles to crack initiation (N_{fi}) and complete pull-through failure (N_{ff}) at a given load level can be obtained from the S-N curve obtained from constant amplitude cyclic tests. The S-N curves of the two-span batten test for crack initiation (N_{fi}) and complete pull-through failure (N_{ff}) are shown in Figure 22. **Error! Reference source not found.** presents the fatigue damage calculated using the modified Miner's rule.

$$\sum_{a=1}^{x-1} \frac{n_a}{(N_{fi})_a} + \frac{y}{(N_{fi})_x} = 1 \qquad (11)$$

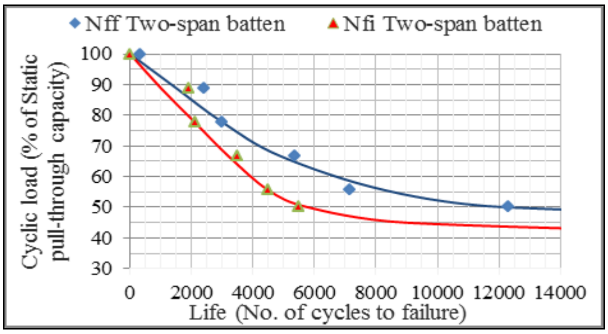

Figure 22: S-N curve of two-span batten test for crack initiation and complete pull-through failure

Table 10: Fatigue damage calculated using the modified Miner's rule for Multi-level cyclic tests

Test No	Cyclic load*	n_a	N_{ff}	N_{fi}	n_a/N_{fi}	y	$\frac{(N_{fi})_x}{(N_{ff})_x}$	Damage
T-1	70	1000	4200	2850	0.35	--		1.04
	80	1500	2700	1900	0.79	1233	0.70	
	70	1028	4200	2850	0.35	--		
T-2	49.5	4500	13600	6000	0.75	--		0.83
	66	600	5100	3300	0.18	--		
	88	295	1600	1100	0.27	75	0.69	
T-3	51.8	4500	10400	5200	0.87	--		0.78
	69	600	4400	3000	0.20	404	0.68	
	92	55	1100	700	0.08	--		
T-4	54	4500	9000	4700	0.96	--		0.98
	72	600	3900	2700	0.22	115	0.69	
	96	80	500	350	0.23	--		
T-5	65.3	4500	5200	3300	1.36	3300	0.63	1.07
	87	360	1800	1200	0.30	--		
	--	--	--	--	--	--		

*- % of static pull-through failure load

Fatigue damage predicted by both basic (
Table 9) and modified miner's rules (**Error! Reference source not found.**) reveal that the modified Miner's rule (mean = 0.94, COV = 0.14) appears to better model the pull-through failure of the roof batten than the basic Miner's rule (mean = 0.83, COV = 0.26). Table 11 presents a summary of the predicted damage. The modified Miner's rule calculates the damage based on N_{fi} and N_{ff} values for the load level where the crack initiation occurred, thus ignoring any interactions/ damage up to that point. Further multi-level static tests are needed to verify this assumption.

Table 10: Comparison of damage predicted by basic and modified Miner's rules

Damage predicted	Predicted damage T-1	T-2	T-3	T-4	T-5	Mean	COV %
Basic	1.03	0.63	0.62	0.81	1.07	0.83	0.26
Modified	1.04	0.83	0.78	0.98	1.07	0.94	0.14

Finally, the fatigue capacity of the roof batten based on LHL loading sequence was obtained using the modified Miner's rule and validated through four LHL tests (Table 11). The ultimate design load, P_t, for fatigue pull-through failure (Table 1), was calculated using the modified Miner's rule based on Equation 11 and S-N curves for crack initiation. It was assumed that the fatigue pull-through capacity is based on the crack initiation at the end of sequence G. As seen in Table 12, the ultimate design load closer to crack initiation is 95% of the static pull-through capacity. Therefore, the design fatigue pull-through capacity of the tested roof batten can be taken as 95% of the batten's static pull-through capacity, i.e. 2.92 kN per fastener. Two LHL tests were conducted based on this P_t, which confirmed crack initiation at the end (Table 11). The load and displacement versus fatigue life graph in this test also confirms this observation (Figure 23).

Table 11: Low-High-Low (LHL) tests

Test No	P_t*	Sequences survived	Crack	Test status
LHL T-1	95	A-G	No	Pass
LHL T-2	95	A-G	Hairline crack	Pass
LHL T-3	100	A-G	Yes (Figure 24)	Failed
LHL T-4	115	A-C	Complete failure	Failed

Table 12: Fatigue damage for LHL Tests 1 and 2

A	$\%P_t$	n_a	P_t*	N_{fi}	F_a	$\sum_{a=A}^{G} F_a$
A	45	4500	42.75	15000	0.30	0.30
B	60	600	57.0	4300	0.14	0.44

C	80	80	76.0	2300	0.03	0.47
D	100	1	95.0	400	0.00	0.48
E	80	80	76.0	2300	0.03	0.51
F	60	600	57.0	4300	0.14	0.65
G	45	4500	42.75	15000	0.30	0.95

*- % of static pull-through failure load

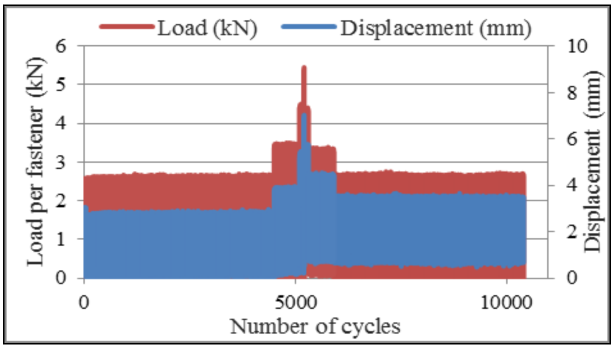

Figure 23: Fastener load and displacement versus fatigue life graph of 95% P_t LHL test

Table 12 shows that the design load that corresponds to a complete fatigue pull-through failure must be higher than 95% of the static pull-through capacity. However, a design load greater or closer to the static pull-through failure capacity should not be taken as the fatigue pull-through capacity as crack initiation dominated by static loading may occur closer to such a design load. To investigate this, two LHL tests were conducted, i.e. 100% (LHL T-3) and 115% (LHL T-4) of the static pull-through capacity to investigate the static failure at the single load sequence D and the fatigue failure before sequence D, respectively. These test results are given in Table 11. The LHL T-3 (closer to 100%) batten survived the LHL load sequences with minor crack as shown in Figure **24**.

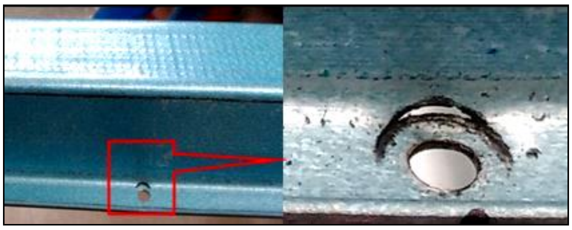

Figure 24: Crack pattern of 100% LHL test

The failure criterion given in [8] for roofing assemblies is that the tested roof assembly should not be disengaged from its supports during the LHL test. However, this will lead to a fatigue pull-through capacity of roof battens from LHL tests to be higher than its static pull-through capacity as observed in this study. This unusual observation is due to the fact that the static pull-through capacity is based on the first tearing of batten (when the load begins to drop) whereas the fatigue pull-through capacity is based on complete pull-through failure. The current failure criterion for LHL tests may only be adequate for roof sheeting due to the differences in the fatigue cracking modes of roof sheeting and battens. Further research is needed.

The small scale tests used in this study did not include the effects of the deformations of flexible supporting members, which might have accelerated the crack growth process and reduced the number of cycles to failure. In this case, LHL tests might give a lower fatigue pull-through capacity. However, based on the experimental results reported in this paper and the above discussions, the fatigue design pull-through capacity of 0.75 mm G550 roof battens exposed to a design cyclone (LHL test) can be taken as 2.92 kN per central support fastener, irrespective of their span as crack initiation does not depend on span (Figure 16).

5. Conclusions

This paper has presented the details of a series of constant amplitude and multi-level cyclic tests of an industrial roof batten to investigate the fatigue pull-through failures at the batten to rafter connection. Three different small scale constant amplitude cyclic tests along with full scale air-box tests were conducted to select the suitable small scale test method for the fatigue study of roof battens. Constant amplitude and multi-level cyclic test results based on the validated small scale two-span test method were then used to modify the basic Miner's rule to predict the fatigue damage in roof battens, and to find the fatigue pull-through capacity of roof battens exposed to a design cyclone simulated by the LHL test.

Test results and the modified Miner's rule have shown that the fatigue design pull-through capacity of roof battens exposed to a design cyclone can be conservatively estimated without conducting the more expensive and time consuming LHL tests. A similar approach used in this paper can be used for other roof battens. Alternatively, the use of a reduction factor of 0.45 with Equations 2 and 3 can be used as a very simple and conservative approach to allow for the fatigue effects of cyclonic wind loading.

Acknowledgements

The authors would like to thank Australian Research Council and Queensland University of

Technology (QUT) for the financial support for this research study. Thanks are also extended to all the technical officers at QUT's O-block laboratory and Banyo Pilot Plant Precinct for their support in using the required laboratory facilities.

References

[1]. Mahendran, M. (1989), Fatigue Behaviour of Corrugated Roofing under Cyclic Wind Loading, Technical Report No. 41, James Cook University CTS, Townsville.

[2]. Stephens, R.I., Fatemi, A., Stephens, R. R., Fuchs, H. O., (2000), Metal Fatigue in Engineering, John Wiley & Sons, Technology & Engineering, USA.

[3]. Standards Australia (2005), AS/NZS 4600, Cold-formed Steel Structures, Sydney.

[4]. American Iron and Steel Institute (AISI) (2007), North American Specification for the Design of Cold-Formed Steel Structural Members, Washington, DC, USA.

[5]. Sivapathasundaram, M., and Mahendran, M., (2014), Pull-through Failure Tests of Thin Steel Roof Battens under Wind Uplift Loads, Proc. of 22nd International Specialty Conference on Cold-Formed Steel Structures, St Louis, Mo, USA, pp. 679-696.

[6]. Sivapathasundaram, M. (2015), Localised Pull-through Failures of Thin Steel Roof Battens Subjected to Wind Uplift loads, Ph.D. thesis, Queensland University of Technology, Brisbane.

[7]. Eurocode 3(EN 1993-1-3). (2006), Design of steel structures - Part 1-3: General rules - Supplementary rules for cold-formed members and sheeting, Brussels

[8]. Building Code of Australia (BCA). (2008). Class 2 to 9 buildings, Vol. One and Class 1 & 10 buildings, Vol. Two, Sydney.

[9]. Standards Australia (1992), AS 4040.3, Methods of testing Sheet Roof and Wall Cladding - Resistance to Wind Pressures for Cyclone Regions, Sydney.

SECM/15/166

Novel Method for Developing S-N Curves for Corrosion Fatigue Damage Assessment of Steel Structures

C. S. Bandara[1*], U. I. Dissanayake[1] and P. B. R. Dissanayake[1]

[1]University of Peradeniya, Peradeniya, Sri Lanka
*E-Mail: chamindasbandara@yahoo.com; bandara@civil.pdn.ac.lk, TP: +94 77 540 0273

Abstract: Corrosion is one of the main problems in steel structures. The combined effect of corrosion and fatigue caused by cyclic loading magnifies the damage severely reducing the fatigue life of the structure. Steel bridges in coastal and industrial zones are among the structures most vulnerable to corrosion fatigue. Up until now there have been no accurate methods introduced for assessing corrosion fatigue damage and predicting the future life of structures in a corrosive atmosphere.

In the S-N approach based fatigue damage assessment method S-N curves should include corrosion effects. If usual S-N curves that do not include corrosion effects are used, they should be modified or safety factors should be applied to account for the effects of corrosion. The present paper describes a study carried out for improving one of the existing full range S-N curve models for corrosion effects. Using adjustments to the existing S-N model a new corrosion based S-N model was proposed. Experimental results showed that the proposed S-N model can be efficiently used for assessing fatigue damage of steel structures located in corrosive atmosphere. The S-N model proposed remains a simple single formula. The only parameters necessary for the new corrosion based S-N model are the ultimate tensile strength, Vickers hardness and the high cycle fatigue strength in corrosive environment.

Keywords: corrosion fatigue, damage assessment, life evaluation, S-N curve, steel structures

1. Introduction

Structural failures of steel bridges and vessels due to corrosion fatigue has have made it a much discussed topic. The Silver bridge collapse in 1967, the Mianus river bridge collapse in 1983, the MV Kiraki vessel failure in 1990, the Aloha aircraft failure in 1998 and the Minnesota bridge failure in 2007 are some examples for corrosion fatigue failures in the past half century.

Corrosion fatigue occurs as a result of synergetic interactions between the environment, material microstructure and cyclic loading [1]. Corrosion fatigue damage accumulates with cyclic loading in four stages: (i) cyclic plastic deformation, (ii) micro-crack initiation (iii) micro-crack growth and coalescence and (iv) crack propagation [2]. Mechanisms behind the corrosion fatigue process in an aqueous environment (most common) can be described as: crack nucleation at corrosion pits due to high stress concentrations, reduction of crack closure, enhancement of slip irreversibility due to oxides in slip steps, electrochemical attack at plastically deformed regions (non-deformed regions act as cathodes), electrochemical attack when the protective oxide film is damaged and surface energy reduction due to the adsorption of environmental species that increase the micro crack growth [1]. It has been found that the combined damage of corrosion and fatigue is greater than the sum of their individual damage [3,4].

Corrosion fatigue is a complex process and there are no universal guidelines for assessing it [1]. The outcomes of this process on structural elements are: rough uneven surface, corrosion pits, reduction of thickness and deteriorated weak material microstructure [5]. All these outcomes raise the stresses due to stress concentrations and reduced cross-sections. Highly stressed locations then act as fracture origins in both static and cyclic loading. Fracture mechanic theories such as stress intensity based pitting corrosion damage models are widely used for assessing failures due to corrosion pits and cyclic loading [7,8]. It is a well accepted fact that corrosion related fatigue damage reduces the fatigue life of metallic materials [3,6]. Therefore, in the S-N approach based fatigue assessments, the S-N curve should contain the effects of corrosion.

Accordingly, the main aims of this study are: proposing a new two steps procedure for corrosion fatigue damage assessments and a simple full range S-N model that includes the effects of corrosion.

2. Hypothesis

In fatigue assessments, the reduction of thickness due to corrosion is usually taken into account by measuring the available thickness. Using the available cross-sectional area of sections, the actual stress is re-calculated. Then, using an S-N curve with a factor of safety to take into account the effects of corrosion and the past loading history of the structure the present fatigue damage is estimated [9]. When evaluating the future life of a structural element, the reduction of the thickness in the future should also be predicted. Corrosion rates of steels obtained from experiments and past studies may be useful for predicting the thickness reduction in the future [10]. Then, using the recalculated stress and the factored S-N curve the future life is evaluated. However, the S-N curve with safety factors is not economical and reliable all the time.

The main cause of failure due to corrosion fatigue is broadly divided into two: (i) Reduction in thickness that increases the stress in the remaining part of the material and (ii) Roughening of the surface and pitting that act as stress raisers due to which cracks initiate earlier and, weakening of the material due to micro-structural changes caused by the combined effects of corrosion and cyclic loading.

Then, the two steps proposed in the new damage assessment procedure are:

(i) Estimating the stress increment in the remaining material due to thickness reduction using thickness measurements.

(ii) Taking into account the effects of surface roughness, pitting and material weakening due to corrosion in the fatigue life by using an accurate SN curve.

The stresses estimated in step (i) can then be used with the S-N curve obtained in step (ii) to calculate the past, present and future damage of the structure due to corrosion fatigue.

As fatigue testing is difficult, costly and time consuming, analytical (or empirical) models and simple tests are necessary. Therefore, using an existing full range S-N model a new simple S-N curve that is able to account for the effects of surface roughness, corrosion pits and macrostructural changes is proposed in section 3.

3. Developing S-N curves with corrosion effects

The full range S-N model proposed by Bandara et al., [11] for assessing structures and components in the non-corrosive environment is given in Eq. (1),

$$\sigma(N) = a(N+B)^b + c \tag{1}$$

where,

$a = \left(\frac{\sigma_{VHCF} - \sigma_k}{N_{VHCF}^b - N_k^b}\right)$, $B = \left(\frac{\sigma_u - c}{a}\right)^{1/b}$,

b = -0.2 and

$$c = \left(\frac{\sigma_k N_{VHCF}^b - \sigma_{VHCF} N_k^b}{N_{VHCF}^b - N_k^b}\right).$$

Here, σ_u is the ultimate tensile strength, N_k is the number of cycles at stress amplitude σ_k that represents the knee point of the S-N curve closer to 10^7 cycles. N_{VHCF} is the number of cycles concerned in the very high cycle fatigue (VHCF) region (> 10^7 cycles) and σ_{VHCF} is the fatigue strength amplitude in VHCF region [12] obtained from Eq. (2),

$$\sigma_{VHCF} = (155 - 7\log N_{VHCF}) \cdot \frac{(Hv+120)}{1000} (\sigma_u)^{1/3} \tag{2}$$

where, Hv is the Vickers hardness.

Vacuum is the perfect non-corrosive environment. Due to the fact that the difference of the fatigue strength of metals such as mild steel in the vacuum and dry air is less than 5% [6], dry air can also be considered non-corrosive. Therefore, the proposed S-N curve can be used in dry air without any modifications. However, if the proposed fatigue model is used for structures and components in a corrosive atmosphere (rain, various gases, water, in the sea etc.,) a modification is necessary. Experiments have shown that the difference between the fatigue strengths in corrosive and noncorrosive environments in low cycle fatigue (LCF) region is low. This difference expands in the high cycle fatigue (HCF) and VHCF regions [2,6]. The expected modification for the full range S-N curve for corrosive atmosphere is as shown in Figure 1 [13].

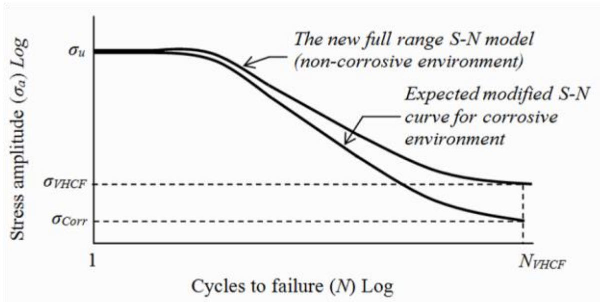

Figure 1: Proposed full range S-N model for corrosive environment. σ_{corr} is the VHCF fatigue strength of steel in the corrosive environment.

3.1 Modifications for corrosion effect

As illustrated in Figure 1, using a linear increase of difference between the non-corrosive and corrosive fatigue strength, the full range S-N curve can be modified to account for the corrosion effects. Eq. (3) shows this modification applied on the full range S-N model.

$$\sigma(N)_{corr} = \sigma(N) - \left(\frac{\sigma_{VHCF}-\sigma_{corr}}{\log(N_{VHCF})-\log(1)}\right)\{\log(N) - \log(1)\} \quad (3)$$

where, σ_{corr} is the VHCF fatigue strength of steel in the corrosive environment.

After simplifying some of the terms, the proposed full range S-N curve model for corrosive environment can be written as in Eq. (4),

$$\sigma(N)_{corr} = \sigma(N) - d \cdot \log(N) \quad (4)$$

where, $d = \frac{(\sigma_{VHCF}-\sigma_{corr})}{\log(N_{VHCF})}$.

The only unknown (except σ_u and Hv) in this modified formula is σ_{corr}.

3.2 Experimental verification

Investigations for corrosion effects of steels on fatigue life is usually performed in two methods of tests; (i) Fatigue testing with low frequencies (5 - 25 Hz etc) using non-corroded specimens that are allowed to corrode during the test in corrosive media, and (ii) Fatigue testing with frequencies about 50 – 150 Hz using pre-corroded specimens.

The difference between the two tests is that the first test provides S-N curves for the combined effects of corrosion and fatigue while corrosion is taking place. The second test provides the effects of existing corrosion on the fatigue life. Test method (ii) is simple and the most relevant for existing structures and components. Therefore, in this study, pre-corroded steel specimens were subjected to fatigue testing.

Three low carbon steels, mild steel (MS), quenched and self tempered steel (QST) and cold twisted deformed steel (CTD) were used for fatigue testing. The mechanical properties of these steels are given in Table 1. The fatigue tester used was a rotating bending fatigue tester with a loading frequency of 50 Hz. The specimens were first polished and then left in contact with water for 60 days. The thickness reduction (60 days) calculated using weight measurements for MS, QST and CTD were 45.3, 36.7 and 39.8 μm respectively.

As mentioned in Section 3.1, predicting the full range S-N curve in a corrosive environment requires determining σ_{corr} in the VHCF region. This parameter should be found by conducting fatigue testing at very low stresses. In this study σ_{corr} at 10^7 cycles for medium and low strength steels was determined using experimental details provided by Revie and Uhlig [6] and given in Table 2. The testing has been done in air and in well water with the test frequency of 25 Hz.

Table 1: Mechanical properties of steels tested (σ_y is the yield strength and El is the percentage elongation)

Material	σ_u (N/mm²)	σ_y (N/mm²)	*El* (%)
Mild steel (MS-2)	426	249	37
Cold twisted deformed steel (CTD)	562	403	33
Quenched and self tempered steel (QST)	595	402	33

Table 2: High cycle fatigue (HCF) limit and corrosion fatigue strength σ_{corr} of steels [6]

Metal	HCF limit in air, σ_{HCF} (N/mm²)	σ_{corr} at 10^7 cycles	$\sigma_{corr}/\sigma_{HCF}$
0.11% C steel, annealed	172	110	0.64
0.16% C steel, quenched and tempered	241	138	0.57
1.09% C steel, annealed	289	158	0.55
3.5% Ni, 0.3% C steel, annealed	338	200	0.59
0.9% Cr, 0.1% V, 0.5% C steel, annealed	289	152	0.52
13.8% Cr, 0.1% C steel, quenched and tempered	345	241	0.70

Prediction of σ_{corr} was done as follows. As the VHCF fatigue strength and σ_{corr} at VHCF region were not available, σ_{corr} at 10^7 cycles and HCF limit σ_{HCF} were used in this study. The ratio ($\sigma_{corr}/\sigma_{HCF}$) for these steels was in the range 0.52 – 0.70 with an average of 0.60. For MS, CTD and QST steels, σ_{HCF} was calculated using the relationship $\sigma_{HCF} = 0.5\sigma_u$. Then, σ_{corr} for MS, CTD and QST steels were estimated from the relationship, $\sigma_{corr} = 0.6\sigma_{HCF}$. Accordingly, the estimated σ_{corr} values for MS, CTD and QST steels were 127.8, 168.6 and 178.5 N/mm² respectively. Then, full range S-N curves of MS, CTD and QST steels with corrosion effects were predicted using Eq. (4). A comparison of predicted S-N curves, experimental data and details for non-corroded steel tests are given in Figures 2, 3 and 4.

The comparison of experimental fatigue data for non-corroded and corroded specimens shows the increasing difference of fatigue strengths as expected. The new corrosion based S-N models for all three steels also show this increasing gap between non-corrosive and corrosive curves well aligning with the experimental data. This observation verifies the ability of the new model to produce S-N curves with corrosion effects well.

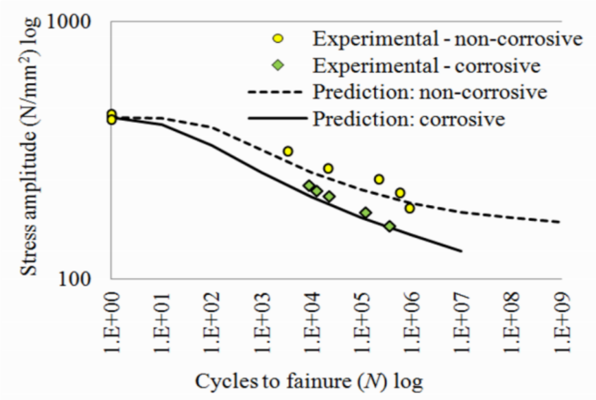

Figure 2: S-N curves for non-corroded and corroded specimens of MS with predictions

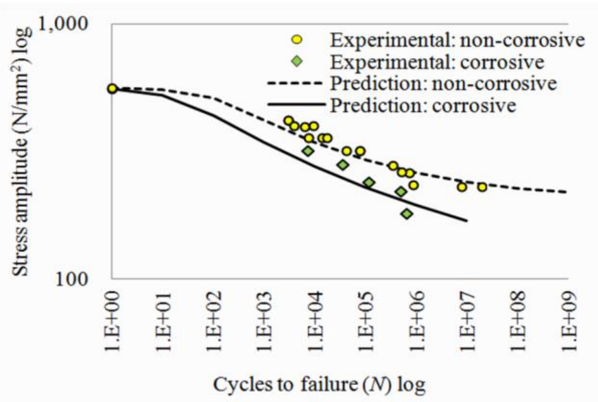

Figure 3: S-N curves for non-corroded and corroded specimens of CTD with predictions

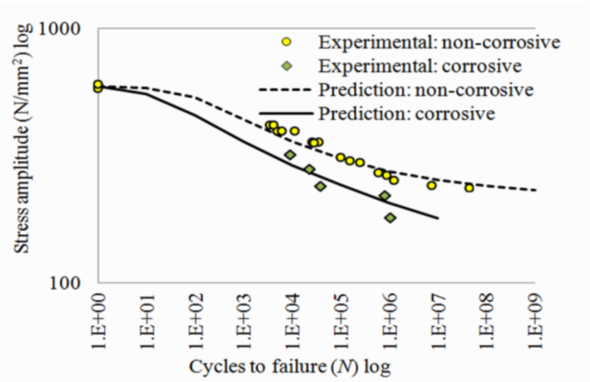

Figure 4: S-N curves for non-corroded and corroded specimens of QST with predictions

Though there are minor differences, experimental fatigue data of corroded specimens and the corresponding full range curves are mostly in good agreement. Reasons for these minor differences are; the difference between corrosion fatigue test data and fatigue testing of pre-corroded specimens and approximations used when estimating σ_{corr}. It should be noted that the method used for estimating σ_{corr} in this study may not always produce good predictions. Therefore, stress intensity and fracture mechanics based methods or experimental methods should be used for estimating σ_{corr}. These methods must be able to combine the effects of material factors, loading conditions and environmental factors.

4. Discussion

The effect of corrosion on steel structures and components creates many problems. Thickness reduction, increased surface roughness, surface irregularities and corrosion pits, and weakening of the material microstructure are some of them. Corrosion reduces the carrying capacity of structural elements. When thickness is reduced, stress in the remaining portion of structural elements increases. Due to surface roughness, surface irregularities and pitting, stresses in structural elements get concentrated, thus magnifying detrimental effects. Due to these many failures involved in corrosion fatigue, the assessment of corrosion fatigue damage is complicated. Therefore, in the present study, a simple two steps procedure was proposed.

In S-N approach based fatigue assessments, usual S-N curves that do not include corrosion effects should be modified and/or factors of safety should be applied. The full range S-N model with corrosion effects proposed in this study does not require any modifications and therefore, it is a valuable tool for fatigue damage assessments.

Due to the fact that fatigue in a corrosive environment (and fatigue in corroded elements) is caused by the combined effects of material, stress and environment, determining σ_{corr} using simple analytical methods is not successful. Therefore, the verification of the new S-N model with corrosion effects was done using both analytical methods and experimental data. It was observed that the new SN model performs well.

The new S-N model has many advantages. It is a simple formula that describes the entire stress – life region in a single function. Therefore this model can be easily used for assessing cumulative fatigue damage caused by both constant and variable amplitude loading. The material parameters needed for developing S-N curves from this model are σ_u, Hv and σ_{corr}. Here, σ_u and Hv are parameters that are obtained from simple tests.

5. Conclusions

The new two steps fatigue assessment procedure and the fatigue S-N model proposed in this paper that takes into account the effects of corrosion (corrosion due to water) is important in the fields of civil, structural and mechanical engineering. The conclusions of the study are as follows.

The procedure can easily be applied for structures once the S-N model is developed. The S-N model can be developed for low and medium carbon steels using three parameters, σ_u, Hv and σ_{corr}. Here too, σ_u, Hv can be found easily using common monotonic tests.

The S-N formula with corrosion effects proposed for carbon steels (in aqueous environment) is able to describe the full stress-life behavior of steel. Therefore, it can be used for both constant and variable amplitude loading to calculate the cumulative fatigue damage.

The average ratio $\sigma_{corr}/\ \sigma_{HCF}$ obtained from experimental results of six low and medium carbon steels is 0.60. This average ratio is a good approximation for determining σ_{corr} of carbon steels.

Acknowledgement

Financial assistance of the National Research Council (Grant NRC-11/106) is acknowledged.

References

[1] Suresh S. 1991. Fatigue of materials. 1st ed. Cambridge: Cambridge university press, Cambridge.

[2]. Gangloff, R. P. 2005. Environmental cracking - corrosion fatigue, Corrosion tests and standards manual, Eds., Baboian, R. Dean, Jr S. W. Hack, H. P. Hibner, E. L. and Scully, J. R., ASTM International.

[3] Wang Y. Z. 2011. Corrosion fatigue, Uhligs corrosion handbook, Ed. Revie R. W. 3rd ed. John Willy, New York.

[4] Cui W. 2002. A state of the art review on fatigue life prediction methods for metal structures, Journal of Material Science & Technology. Vol. 07, pp. 43-56.

[5] Roberg, P. R. 2000. Handbook of corrosion engineering, 1st Ed., McGraw Hill, New York.

[6] Revie R. W, Uhlig H.H. 2008. Corrosion and corrosion control. 4th ed. John Willy, New Jersey.

[7] Hoeppner, D. W., Chandrasekaran, V., and Taylor, A. M. H. 1999. Review of pitting corrosion fatigue models, Proceedings of ICAF International Conference, Seattle.

[8] Acun, N., Gonza lez-Sa nchez, J., Ku-Basultoa,

G. and Domı nguez, L. 2006. Analysis of the stress intensity factor around corrosion pits developed on structures subjected to mixed loading, Scripta Materialia, Vol. 55, pp. 363–366.

[9] Rathnayake, R. M. S. U. P., and Dissanayake, P. B. R. 2011. Methodology for condition assessment and retrofitting of railway bridges, Proceedings of the 4th International Conference on Structural Engineering and Construction Management, Kandy, Dec 12-14, 2011.

[10] Bandara C. S., Siriwardane S. C., Dissanayake U., and Dissanayake R. 2014. Corrosion effects on fatigue life of steel structures, Proceedings of the 5th International Conference on Sustainable Built Environment, Kandy, Dec 12-15, 2014.

[11] Bandara, C. S., Siriwardane, S. C., Dissanayake, U. I., and Dissanayake, R. 2015. Developing a full range S-N curve and estimating cumulative fatigue damage of steel elements, Computational Materials Science, Vol. 96, pp. 96101.

[12] Bandara, C. S., Siriwardane, S. C.,

Dissanayake, U. I., and Dissanayake, R. 2014. Fatigue failure predictions for steels in the very high cycle region – A review and recommendations, Engineering Failure Analysis, Vol. 45, pp. 421 – 435.

[13] El Aghoury I. 2012. Numerical tool for fatigue life prediction of corroded steel riveted connections using various damage models, PhD Thesis, Concordia university, Montreal.

SECM/15/170

Fatigue Life Prediction of Steel Bridges with High Amplitude Loadings

P.A.K. Karunananda[1], T.M. pallewatta[1], P.B.R. Dissanayake[2], M. Ohga[3] and S.A.S.C.Siriwardane[4]

[1]Department of Civil Engineering, The Open University of Sri Lanka, Sri Lanka
[2]Department of Civil Engineering, University of Peradeniya, Sri Lanka
[3]Department of Civil and Environmental Engineering, Ehime University, Japan
[4]Department of Mechanical Engineering, University of Stavanger, Norway

Abstract: This paper presents a new fatigue model to predict life of steel bridges considering the effect of high amplitude loading. It consists of a modified strain-life curve and a new strain based damage index. Modified strainlife curve consists of Coffin-Manson relation in low cycle fatigue region and a new strain-life curve in high cycle fatigue region. The damage variable is based on a modified von Mises equivalent strain to account for the effects of loading non-proportionality and strain path orientation in multiaxial stress state. The proposed model was verified with experimental test results of two materials available on the literature. Then, it was illustrated with an old riveted wrought iron railway bridge. The obtained results verify the effectiveness of the proposed model over commonly used Miner's rule based life prediction of steel bridges.

Keywords: High cycle fatigue, low cycle fatigue, steel bridges, life prediction, high amplitude loading.

1. Introduction

Bridges are generally subjected to low amplitude loading by usual traffic. As a result, bridge members generally experience high cycle fatigue (HCF) damage. During their service life, bridges may also be subjected to high amplitude loading due to earthquakes, unexpected stress concentrations and etc. When a bridge is subjected to high amplitude loading, some members may undergo inelastic stresses. These inelastic stresses may cause low cycle fatigue (LCF) damage during the high amplitude loading while subjecting to HCF in service conditions. This combined damage of HCF and LCF may cause a reduced life of members (Kondo and Okuya 2007). In addition, bridges connections are generally subjected to multiaxial stress states and combined with HCF and LCF create a complexity in accurate estimation of fatigue life.

Most of existing fatigue life research of bridges is based on multiaxial high cycle fatigue. To the knowledge of authors, there is almost no literature regarding high amplitude loading effects on bridges. However, in other fields such as aircraft and automobile engineering, von Mises equivalent strain and Coffin-Manson strain-life curve are used with Miner's rule as the general method to estimate the life due to high and low amplitude loadings (Suresh 1998). The Miner's rule is the simplest and the most widely used fatigue life prediction technique. One of its interesting features is that life calculation is simple and reliable when the detailed loading history is unknown. However under many variable amplitude loading conditions, Miner's rule based life predictions have been found to be unreliable since it cannot capture loading sequence effect (Siriwardane et al. 2008). In addition, von Mises equivalent strain cannot capture the effects due to non-proportional loading and orientation of strain path (Borodii and Adamchuk 2009). As a result, it usually predicts inaccurate fatigue life.

These reasons raise the question about accuracy of the Miner's rule based life estimation for high and low amplitude loadings. Therefore, it is necessary to have a comprehensive model, which is based on commonly available material properties, to estimate more accurately the life due to high and low amplitude loadings. The objective of this paper is to propose a new model to accurately estimate the fatigue life (crack initiation life) when a bridge is subjected to high amplitude loading in addition to the usual low amplitude loading.

2. Proposed Fatigue Model

This section proposes the new fatigue model to consider the effect of high amplitude loading.

Initially, the details relevant to proposed damage variable, modified strain-life fatigue curve are discussed. Then, it is followed by the proposed damage indicator.

2.1 Damage variable

The proposed damage variable for multiaxial stress state is given as,

$$\varepsilon_{eq} = (1+\alpha\phi)(1+kSin\varphi)\varepsilon_{VM} \tag{1}$$

where ε_{eq} is the equivalent strain amplitude in the multiaxial stress state, α is the material parameter for loading non-proportionality, ϕ is the cycle non-proportionality parameter, k is the material parameter for strain path orientation, φ is the angle between principal direction and applied strain path and ε_{VM} is the von Mises equivalent strain as given

$$\varepsilon_{VM} = \frac{1}{(\sqrt{2}\times(1+\nu))}\begin{bmatrix}(\varepsilon_{xx}-\varepsilon_{yy})^2+(\varepsilon_{yy}-\varepsilon_{zz})^2\\ +(\varepsilon_{zz}-\varepsilon_{xx})^2\\ +\frac{3}{2}\times(\gamma_{xy}^2+\gamma_{yz}^2+\gamma_{zx}^2)\end{bmatrix}^{1/2} \tag{2}$$

where ν is the Poison ratio, ε and γ are the axial and shear strain amplitudes in respective planes.

The first expression in parentheses of equation (1) is the degree of additional strain hardening depending on the cycle geometry to account for non-proportional loading. The second expression in parentheses is strain hardening depending on the orientation of the cyclic strain path for proportional loading. The material parameters (α and k) have to be estimated by additional testing of the material. ϕ and φ can be estimated for given strain path considering cycle geometry and its orientation, respectively (Borodii and Adamchuk 2009).

2.2 Strain-life curve

To take account the damage dependent effect in high and low amplitude loading, it is necessary to modify the strain-life fatigue curve in HCF regime. The proposed curve consists of two parts as shown in Figure 1. The first part of the curve describes fatigue life of plastic strain $(\varepsilon_{eq} \geq \varepsilon_y)$ cycles which usually affects LCF. To describe this part, Coffin-Manson strain-life curve is utilized as shown below.

$$\varepsilon_{eq} = \frac{\sigma_f^{'}}{E}(2N)^b + \varepsilon_f^{'}(2N)^c \tag{3}$$

where ε_{eq} is the equivalent strain amplitude in multiaxial stress state, N is the number of cycles to failure, $\sigma_f^{'}$ is the fatigue strength coefficient, b is the fatigue strength exponent, $\varepsilon_f^{'}$ is the fatigue ductility coefficient, c is the fatigue ductility exponent and E is the elastic modulus of the material.

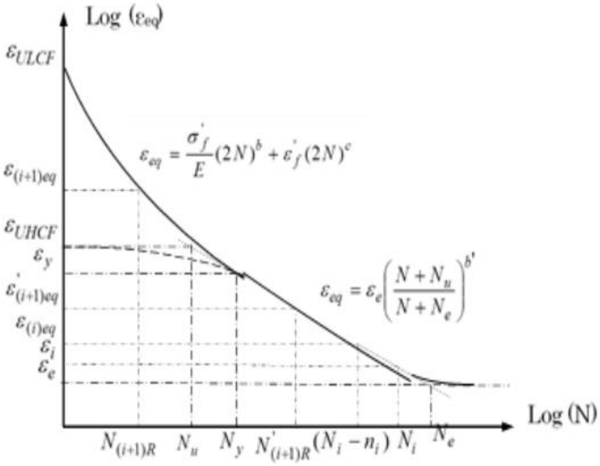

Figure 1: Schematic representation of the proposed strain-life curve

The ultimate strain of low cycle fatigue, $(\varepsilon)_{ULCF}$ which is the strain amplitude corresponding to failure in half reversal (a quarter of a cycle) is obtained from equation (3) as,

$$(\varepsilon)_{ULCF} = \varepsilon_f^{'} \tag{4}$$

The second part of the curve describes the fatigue life of elastic strain cycles which usually $(\varepsilon_{eq} < \varepsilon_y)$ affects HCF. This part of curve represents hypothetical fully known curve. The shape of the curve is obtained by directly transforming the previous fully known stress-life curve (Siriwardane et al. 2008) to elastic strain-life curve as shown below.

$$\varepsilon_{eq} = \varepsilon_e\left(\frac{N+N_u}{N+N_e}\right)^{b'} \tag{5}$$

where ε_e is the strain amplitude of the fatigue limit, N_e is the number of cycles to failure at strains of ε_e. The ε_y and N_y are the yield strain and the corresponding number of cycles to failure. The b' is the slope of the finite life region of the curve. The $(\varepsilon)_{UHCF}$ is the ultimate strain of HCF which is the elastic strain amplitude corresponding to half reversal (a quarter of a cycle) is expressed as,

$$(\varepsilon)_{UHCF} = \left(\frac{\sigma_u}{E}\right) \quad (6)$$

where σ_u is the ultimate tensile strength of the material. The N_u is the number cycles corresponding to the intersection of the tangent line of the finite life region and the horizontal asymptote of the ultimate elastic strain amplitude $(\varepsilon)_{UHCF}$ as shown in Figure 1.

2.3 Damage indicator

The proposed damage indicator considers combined damage of high and low amplitude loadings. The hypothesis behind this fatigue law is that if the physical state of damage is the same, then fatigue life depends only on the loading condition. Suppose a component is subjected to a certain equivalent strain amplitude $(\varepsilon)_i$ of n_i number of cycles at load level *i*. N_i is the fatigue life (number of cycles to failure) corresponding to $(\varepsilon)_i$ (Figure 1). Therefore, the reduced life at the load level *i* is obtained as (N_i−n_i). $(\varepsilon)_{(i)eq}$ The damage equivalent strain (Figure 1), corresponding to the failure life (Ni−ni) is defined as ith level damage equivalent strain. Then, the new damage indicator, Di is stated as,

$$D_i = \frac{(\varepsilon)_{(i)eq} - (\varepsilon)_i}{(\varepsilon)_u - (\varepsilon)_i} \quad (7)$$

where the $(\varepsilon)_u$ is

$$(\varepsilon)_u = \begin{cases} \varepsilon_{ULCF} & (\varepsilon)_i \geq \varepsilon_y \\ \varepsilon_{UHCF} & (\varepsilon)_i < \varepsilon_y \end{cases} \quad (8)$$

At the end of i^{th} loading level, damage D_i has been accumulated (occurred) due to the effect of $(\varepsilon)_{i+1}$ loading cycles, the damage is transformed to load level *i+1* as below.

$$D_i = \frac{(\varepsilon)'_{(i+1)eq} - (\varepsilon)_{i+1}}{(\varepsilon)_u - (\varepsilon)_{i+1}} \quad (9)$$

and $(\varepsilon)_u$ is expressed

$$(\varepsilon)_u = \begin{cases} \varepsilon_{ULCF} & (\varepsilon)_{i+1} \geq \varepsilon_y \\ \varepsilon_{UHCF} & (\varepsilon)_{i+1} < \varepsilon_y \end{cases} \quad (10)$$

Then, $(\varepsilon)'_{(i+1)eq}$ is the damage equivalent strain at loading level *i+1* and it is calculated as,

$$(\varepsilon)'_{(i+1)eq} = D_i[(\varepsilon)_u - (\varepsilon)_{i+1}] + (\varepsilon)_{i+1} \quad (11)$$

The corresponding equivalent number of cycles to failure $N'_{(i+1)R}$ is obtained from the strain-life curve as shown in Figure 1. The $(\varepsilon)_{i+1}$ is the equivalent strain at the level i+1 and supposing that it is subjected to number of cycles, then the corresponding residual life at load level i+1, $N_{(i+1)R}$ is calculated as,

$$N_{(i+1)R} = N'_{(i+1)R} - n_{(i+1)} \quad (12)$$

Therefore, strain $(\varepsilon)_{(i+1)eq}$, which corresponds to $N_{(i+1)R}$ at load level *i+1,* is obtained from the strain-life curve as shown in Figure 1. Then the cumulative damage at the end of load level *i+1* is defined as,

$$D_{(i+1)} = \frac{(\varepsilon)_{(i+1)eq} - (\varepsilon)_{i+1}}{(\varepsilon)_u - (\varepsilon)_{i+1}} \quad (13)$$

This is carried out until D_i is equal to 1.

3. Experimental verification of The Proposed model

This section explains the verification of the proposed fatigue model. Experimental test results of two materials were used for this purpose: S304L stainless steel and Haynes 188.

3.1 Verification for S304L Steel

Random variable fatigue test performed by Colin and Fatami 2010 were used to verify the proposed fatigue model. Experimental results were compared with the predicted lives of the proposed fatigue model as well as the Miner's rule based previous model. The obtained comparisons are given in Table 1.

Table 1: Experimental summary and predicted fatigue lives of S304L steel

Test	Maximum strain	Minimum strain	Experimental life (blocks)		Predicted life (blocks)	
			Test life	Average life	Previous model	Proposed model
1	0.001	-0.001	211			
2	0.001	-0.001	196			
				203	259	239
3	0.005	-0.005	1601			
4	0.005	-0.005	1740			
				1671	2789	2118
5	0.003	-0.003	14463			
6	0.003	-0.003	15666			
				15065	20122	10075

In above table, first two tests are in LCF region while other four are combined HCF and LCF tests. If the percentage variations of the predictions are estimated with the experimental results, Miner's rule gives a percentage variation of 26.59% while the proposed model gives 15.39%. Therefore, Proposed model based fatigue lives are more accurate than previous model predictions.

3.2 Verification for Haynes 188

Block loading fatigue tests performed by Bonacuse and Kalluri 2002 were used to verify the proposed fatigue model. Here, axial (A) and torsional (T) block loading tests were performed in four different sequences (AA, TT, AT and TA) as shown Table 4. The first loading block is in the high cycle fatigue region and the second is in the low cycle fatigue region. The material parameter, *k*, was estimated as 0.17 by constant amplitude testing given in Kalluri and Bonacuse 1999. Experimental results were compared with the predicted lives of the proposed fatigue model as well as previous model as given in Table 1.

Table 2: Experimental summary and predicted fatigue lives of Haynes 188

	First load level		Second load level			Predicted life (cycles)	
Test	Strain amplitude	No of cycles (n_1)	Strain amplitude	No of cycles (n_2)	Experimental life (n_1+n_2)	Previous model	Proposed model
AA1	0.0067	3926	0.0203	789	4715	4365	4413
AA2	0.0066	7851	0.0202	758	8609	8249	8337
AA3	0.0066	15702	0.0203	659	16361	15977	16147
AA4	0.0066	23553	0.0205	815	24368	23709	23931
TT1	0.0120	5857	0.0345	1250	7107	7276	7414
TT2	0.0120	11714	0.0349	1100	12814	12923	13189
TT3	0.0121	23427	0.0347	1343	24770	24316	24832
TT4	0.0119	35141	0.0347	1467	36608	35677	36219
TT5	0.0120	40998	0.0349	1294	42292	41348	41812
AT1	0.0069	3926	0.0348	1189	5115	5084	5345
AT2	0.0069	7851	0.0347	1218	9069	8660	9093
AT3	0.0065	15702	0.0344	930	16632	16058	16600
AT4	0.0066	23553	0.0346	1253	24806	23885	24185
TA1	0.0121	5857	0.0201	560	6417	6316	6367
TA2	0.0120	11714	0.0203	494	12208	12133	12216
TA3	0.0119	23427	0.0200	459	23886	23740	23907
TA4	0.0119	35141	0.0204	427	35568	35322	35588

The percentage variations of predicted lives from experimental lives for previous and proposed models were estimated as 0.74% and 0.62%, respectively. Therefore, the predicted fatigue lives by the proposed fatigue model are more accurate than previous model predictions.

3.3 Case study

This section explains the application of the proposed model to a riveted wrought iron railway bridge. The selected bridge is one of the longest railway bridges in Sri Lanka and a view of the bridge is shown in Figure 2 (a). The evaluations are especially based on secondary stresses and strains, which are generated around the riveted connection of the member due to stress concentration effect of primary stresses caused by usual traffic (low amplitude) and earthquake (high amplitude) loadings. The selected member is shown in Figure 2 (b).

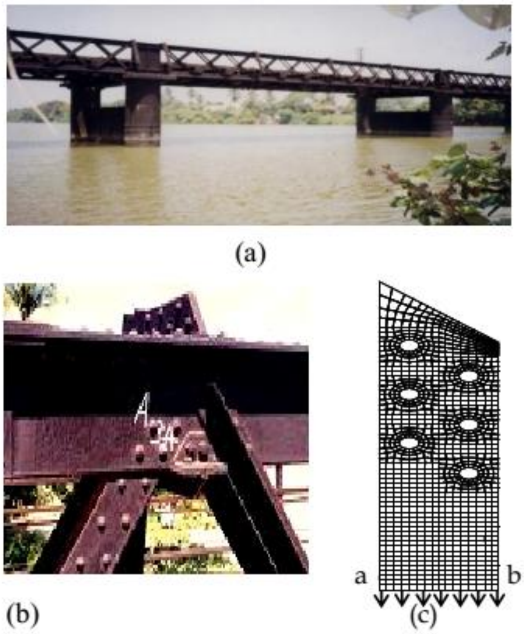

Figure 2: Views of (a) the bridge; (b) considered member and (c) the FEM mesh.

The fatigue life is estimated based on the state of strain considering all rivets are in active state while they have no clamping force. The clamping force is generally defined as the compressive force in plates which is induced by the residual tensile force in the rivet. Since there are no clamping force (value of clamping force is zero), connected members are considered to subject to the biaxial stress state. Then, a critical member without rivets can be considered to analyze the biaxial state of stress of a 2D finite element analysis. The nine node isoperimetric shell elements were used for the FE analysis as shown in Figure 2(c). Earthquake (high amplitude loading) was considered to occur at different times in bridge life (10, 50, 75 and 100 years) as given in Table 3.

Table 3: Fatigue life of the member for different earthquake occurrences

Time of earthquake (after construction, years)	Previous model (Miner's rule)		Proposed model	
	Fatigue life (years)	Percentage reduction of life (%)	Fatigue life (years)	Percentage reduction of life (%)
10	127.7	5.0	130.9	19.6
50	127.7	5.0	109.6	32.7
75	127.7	5.0	116.3	28.6
100	127.7	5.0	130.5	19.9
No earthquake	134.5	-	162.8	-

It is assumed that usual traffic load is followed after the earthquake. The fatigue life of the member was estimated using two approaches: (1) proposed model; (2) previous model (Coffin-Manson curve with the Miner's rule) and the obtained results are given in Table 3. The results indicate fatigue damage caused by earthquake loading causes an appreciable reduction of bridge life. There, the percentage reduction of life is the highest when the earthquake occurs 50 years after the construction. If the earthquake magnitude is increased, the highest percentage reduction of life occurs earlier than 50 years. Therefore, the magnitude of the earthquake load has an effect in estimating the year with the highest percentage reduction. For the previous model, the reduction of service life is constant (5%) irrespective of time of earthquake occurrence since Miner's rule cannot represent the loading sequence effect. These results show the effectiveness of the proposed method over previous model in life prediction.

The differences of case study results confirm the importance of considering high amplitude loading to estimate the fatigue life of existing steel bridges in addition to usual traffic loadings.

5. Conclusions

A new model for life estimation of high amplitude loading was proposed. Verification of the model was conducted by comparing the predicted lives with experimental lives of two materials. It was shown that the proposed fatigue model can represent the effect of high amplitude loading better than the previous model where detailed stress histories are known. The proposed fatigue model was utilized to estimate the fatigue life of a bridge member. Case study realized the importance of consideration of the high amplitude loading caused by earthquake in addition to low amplitude loading due to usual traffic loading in steel bridges. The effectiveness of the proposed model over the Miner's rule based previous model was verified.

References

[1] Bonacuse P and Kalluri S (2002). Sequenced axial and torsional cumulative fatigue: low amplitude followed by high amplitude loading, Biaxial/Multiaxial Fatigue and Fracture, Elsevier.

[2] Borodii MV and Adamchuk MP (2009). Life assessment for metallic materials with the use of the strain criterion for low cycle fatigue. International Journal of Fatigue. 31, pp. 1579-1587.

[3] Colin L and Fatami A (2010). Variable amplitude cyclic deformation and fatigue behavior of stainless steel 304L including step, periodic and random loading. Fatigue and Fracture of Engineering Materials and Structures. 33, pp. 205-220.

[4] Kalluri S and Bonacuse PJ (1999). Cumulative axial and torsional fatigue: an investigation of load-type sequencing effects. ASTM symposium on multiaxial fatigue and deformation: testing and production, Seattle, WA

[5] Kondo Y and Okuya K (2007). The effect of seismic loading on the fatigue strength of welded joints. Material Science and Engineering A. 468-470. pp. 223-229.

[6] Siriwardane S, Ohga M, Dissanayake R and Taniwaki K (2008). Application of new damage indicator-based sequential law for remaining fatigue life estimation of railway bridges. Journal of Constructional Steel Research. 64(2). pp. 228-237.

[7] Suresh S (1998). Fatigue of Materials, UK: Cambridge University Press, Cambridge.